Copyright Undertaking

This thesis is protected by copyright, with all rights reserved.

By reading and using the thesis, the reader understands and agrees to the following terms:

1. The reader will abide by the rules and legal ordinances governing copyright regarding the use of the thesis.
2. The reader will use the thesis for the purpose of research or private study only and not for distribution or further reproduction or any other purpose.
3. The reader agrees to indemnify and hold the University harmless from and against any loss, damage, cost, liability or expenses arising from copyright infringement or unauthorized usage.

If you have reasons to believe that any materials in this thesis are deemed not suitable to be distributed in this form, or a copyright owner having difficulty with the material being included in our database, please contact lbsys@polyu.edu.hk providing details. The Library will look into your claim and consider taking remedial action upon receipt of the written requests.

Pao Yue-kong Library, The Hong Kong Polytechnic University, Hung Hom, Kowloon, Hong Kong

http://www.lib.polyu.edu.hk

HETEROEPITAXIAL GROWTH OF LEAD MAGNESIUM NIOBATE-LEAD TITANATE THIN FILMS BY PULSED LASER DEPOSITION METHOD

SUBMITTED BY

HAU FEI FEI

FOR THE DEGREE OF

MASTER OF PHILOSOPHY IN PHYSICS

AT

THE HONG KONG POLYTECHNIC UNIVERSITY

2002

Pao Yue-kong Library
PolyU · Hong Kong

Abstract

In the present research we have used pulsed laser deposition (PLD) method to prepare super high-*k* $(1-x)[Pb(Mg_{1/3}Nb_{2/3})O_3]-x[PbTiO_3]$ ($PMN_{1-x}-PT_x$) dielectric thin films for future high-density dynamic random access memory (DRAM) applications. $PMN_{1-x}-PT_x$ films with x = 0.1 and 0.35 have been grown on various substrates with $La_{0.7}Sr_{0.3}MnO_3$ (LSMO) and $BaPbO_3$ (BPO) conducting oxides as well as Pt bottom electrodes. Conditions for heteroepitaxial growth of PMN-PT films have been identified. Structural and electrical properties of all these films have been carefully evaluated and compared. Integration of PMN-PT super high-*k* dielectric films with Si has been attempted via Pt and TiN buffer layers. Good structural quality PMN-PT/Pt/Si, PMN-PT/LSMO/Pt/Si and PMN-PT/BPO/Pt/Si heterostructures have been obtained. In addition, heteroepitaxial $(001)_{PMN-PT}||(001)_{LSMO}||(001)_{MgO}||(001)_{TiN}||(001)_{Si}$ has been demonstrated. Our results also reveal that the use of lead based oxide electrode (BPO) has reduced the dielectric leakage current. A maximum room temperature dielectric constant of 1750 at 10 kHz and a minimum leakage current of 6.78×10^{-9} A/cm^2 at 1V have been recorded.

Acknowledgements

I would like to acknowledge my supervisor Dr. K. H. Wong, for his valuable advice and discussion throughout these two years. Special thanks would be given to Miss Phoebe Ho for helping me in some electrical measurements. Thanks would also go to Mr. M. N. Yeung for his assistance in SEM characterization. I would also like to thank my research companions, Mr. K.S. So, Miss H.Y. Cheung, Mr. K. M. Yeung, and Mr. W.S. Tsang for their useful suggestions. This project is supported by a Research Grant of The Hong Kong Polytechnic University under Code No. G-W035. I am grateful for the award of a research studentship by the university.

Table of Contents

Abstract i
Acknowledgements ii
Table of contents iii

Chapter 1 Introduction
1.1 Background 1
1.2 Lead magnesium niobate – lead titanate (PMN-PT) 2
1.3 Dynamic random access memory (DRAM) 7
1.4 Dielectric properties 12
1.5 Outline of thesis 14

Chapter 2 Pulsed Laser Deposition (PLD)
2.1 Introduction 16
2.2 History of PLD 16
2.3 Mechanisms of PLD 17
2.3.1 Laser radiation interaction with the target 18
2.3.2 Dynamics of the plasma plume 19
2.3.3 Interaction of the plasma plume with the substrate 19
2.3.4 Nucleation and growth of a thin film on the substrate surface 20
2.4 Advantages and disadvantages of PLD 21

Chapter 3 Experimental Set-up and Measurements
3.1 Introduction 23
3.2 Experimental set-up and procedure 23
3.3 Characterization of thin films 26
3.3.1 X-ray diffractometry (XRD) 26
3.3.2 Scanning electron microscopy (SEM) 31
3.3.3 Surface profiling 32
3.3.4 Leakage current measurement 33
3.3.5 Dielectric measurement 33

Chapter 4 Fabrication and Characterization of PMN_{1-x}-PT_x on LAO Single Crystal Substrate

4.1 Introduction 35

4.2 PMN_{1-x}-PT_x/LSMO/LAO 36

4.2.1 Fabrication and structural characterization of thin films 36

4.2.2 Electrical properties 43

4.2.2.1 Leakage current measurement 43

4.2.2.2 Dielectric measurement 44

4.3 Thickness dependence of $PMN_{0.9}$-$PT_{0.1}$/LSMO/LAO 46

4.3.1 Fabrication and structural characterization of thin films 46

4.3.2 Surface morphology 49

4.3.3 Electrical properties 52

4.3.3.1 Leakage current measurement 52

4.3.3.2 Dielectric measurement 53

Chapter 5 Fabrication and Characterization of $PMN_{0.9}$-$PT_{0.1}$/LSMO/MgO/TiN/Si

5.1 Introduction 55

5.2 Fabrication and characterization of $PMN_{0.9}$-$PT_{0.1}$/LSMO/MgO 56

5.2.1 Fabrication and structural characterization of thin films 56

5.2.2 Surface morphology 59

5.2.3 Electrical properties 61

5.3 LSMO/MgO/TiN/Si 62

5.3.1 Fabrication and structural characterization of thin films 62

5.3.2 Surface morphology 64

5.4 $PMN_{0.9}$-$PT_{0.1}$/LSMO/MgO/TiN/Si 66

5.4.1 Fabrication and structural characterization of thin films 66

5.4.2 Surface morphology 68

5.4.3 Electrical properties 70

5.4.3.1 Leakage current measurement 70

5.4.3.2 Dielectric measurement 71

Chapter 6 Fabrication and Characterization of $PMN_{0.9}$-$PT_{0.1}$ Films with $BaPbO_3$ Electrode

6.1 Introduction 72
6.2 $PMN_{0.9}$-$PT_{0.1}$ on LAO with BPO bottom electrodes 73
6.2.1 Fabrication and structural characterization of thin films 73
6.2.2 Surface morphology 76
6.2.3 Leakage current and dielectric constant measurement 78
6.3 $PMN_{0.9}$-$PT_{0.1}$ on MgO with BPO bottom electrodes 78
6.3.1 Fabrication and structural characterization of thin films 78
6.3.2 Surface morphology 80
6.3.3 Electrical properties 82
6.3.3.1 Leakage current measurement 82
6.3.3.2 Dielectric measurement 83
6.4 $PMN_{0.9}$-$PT_{0.1}$ on Pt/Si with LSMO and BPO oxide electrodes 84
6.4.1 Fabrication and structural characterization of thin films 84
6.4.2 Surface morphology 86
6.4.3 Electrical properties 90
6.4.3.1 Leakage current measurement 90
6.4.3.2 Dielectric measurement 91

Chapter 7 Conclusions 93

References 97

Chapter One

Introduction

1.1 Background

Rapid progress in miniaturization of electronic systems makes great demands on reduction of the size of the passive components as well as on increasing their functionality. These requirements are acutely felt in dynamic random access memory (DRAM) capacitor technology, in which the size of an individual memory cell keeps on shrinking towards the theoretical limit, and the component density leaps up one order of magnitude every 2-3 years. The conventional dielectric insulator based on SiO_2 has already reached its upper limit of usefulness. Any further progress on DRAM technology needs the introduction of new storage capacitor dielectric and electrode materials. In this research, pulsed laser deposition method is used to fabricate high quality heteroepitaxially grown super high-*k* dielectric capacitor for potential DRAM applications. $0.9Pb(Mg_{1/3}Nb_{2/3})O_3$ – $0.1PbTiO_3$ ($PMN_{0.9}$-$PT_{0.1}$) is chosen in this project because it exhibits unusually large dielectric constant at room temperature.

Pulsed laser deposition (PLD) has been demonstrated to be an excellent technique to fabricate high quality perovskite oxide thin films. Besides, PLD is a technique that is easy to grow multi-layer films. In addition, the high substrate

temperature causes thermal damage on a Si wafer by an atomic diffusion from the ferroelectric film and thermal melting of metal wire [Matsumuro et. al., 1998]. PLD method is expected as a low-temperature process since the ablated species are highly energetic and the substrate temperature for crystallization can be reduced.

1.2 Lead magnesium niobate - lead titanate (PMN-PT)

Lead magnesium niobate, $Pb(Mg_{1/3}Nb_{2/3})O_3$ (PMN), with perovskite structure is a well known relaxor ferroelectric which is characterized by a diffuse phase transition and a strong frequency dispersion of the broad dielectric peak at around –15°C. $PbTiO_3$ (PT) is a typical normal ferroelectric material with T_c = 492°C. The solid solution of PMN and PT, PMN_{1-x}-PT_x exhibits relaxor ferroelectric for $x < 0.4$ [Shrout et al., 1990] and has been reported to have ultra-high dielectric constant of >30,000 (cf. SiO_2 of 3-4) [Swartz et al., 1984].

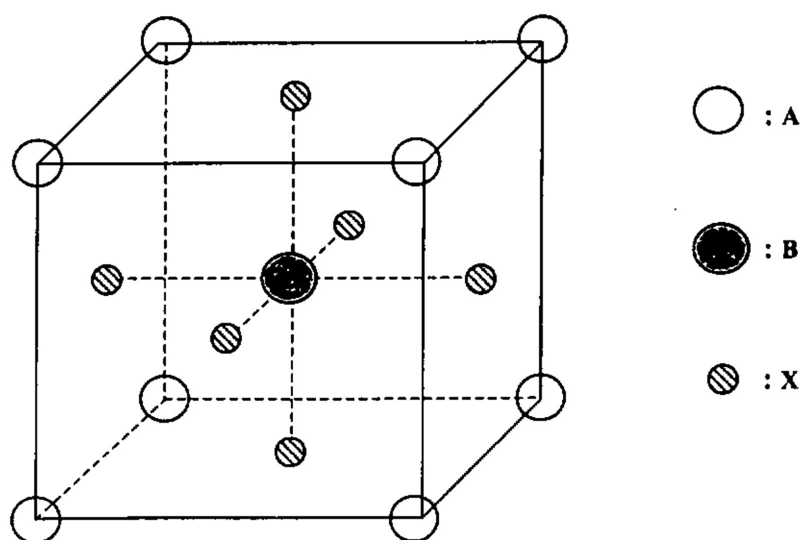

Fig. 1.1 A unit cell for the perovskite crystal structure.

A unit cell of perovskite structure is shown in Fig. 1.1. Perovskite structures have two types of cations (represented by A and B), their chemical formula may be designated as $A_mB_nX_p$.

PMN relaxor ferroelectric has several identifiable properties. First, it has a very large dielectric constant. The dielectric permittivity vs temperature profile shows a broad peak because the phase transition of relaxor occurs over a wide range of temperature. The temperature of dielectric maximum, T_m, increases with frequency. For $Pb(Mg_{1/3}Nb_{2/3})O_3$, Smolensky has reported that the behavior of the dielectric permittivity is mainly caused by the fluctuations in Mg : Nb concentration and the disorder of Mg and Nb ions [Smolensky, 1970]. Secondly, PMN is

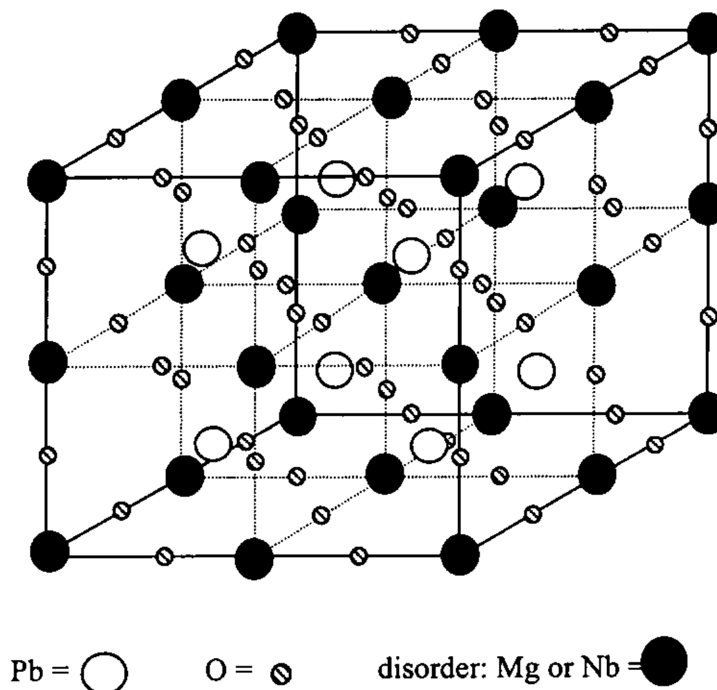

Fig. 1.2 Perovskite structure of PMN.

ferroelectric at low temperature with hysteresis loop. However, the hysteretic response slowly degenerates into just nonlinearity as the temperature increases. Lastly, there are no optical or x-ray evidences for the presence of macroscopic phase change below the transition temperature T_c [Cross, 1987].

The microscopic structure and the fundamental origins of the relaxor ferroelectrics behavior remain in doubt. It is generally accepted that the relaxor behavior of mixed B-site cation perovskites is related to the B-site chemical ordering. According to Smolensky, this different property between relaxor and normal ferroelectrics originates from their different order of B site and local composition fluctuations [Smolensky, 1970]. Fig. 1.2 shows the cubic perovskite structure of PMN. For $PbTiO_3$, the B-site only has one species (Ti^{4+}). For PMN, it has two species (Mg^{2+} and Nb^{4+}) in B site with chemical disorder. The chemical disorder of B-site and local composition fluctuations lead to large fluctuations in Curie temperature. This fluctuation of Curie temperature at different crystal regions leads to a diffuse phase transition.

The PMN forms a solid solution with PT where Mg^{2+} and Nb^{4+} are replaced by Ti^{4+} on the octahedral site of the perovskite structure. Fig 1.3 shows the phase diagram of PMN-PT system [Shrout et al, 1990a].

In recent years PMN_{1-x}-PT_x relaxor ferroelectric have been intensively studied. Their unique dielectric behavior and the unusually large piezoelectric response make them very attractive for integrated multi-layer capacitors and

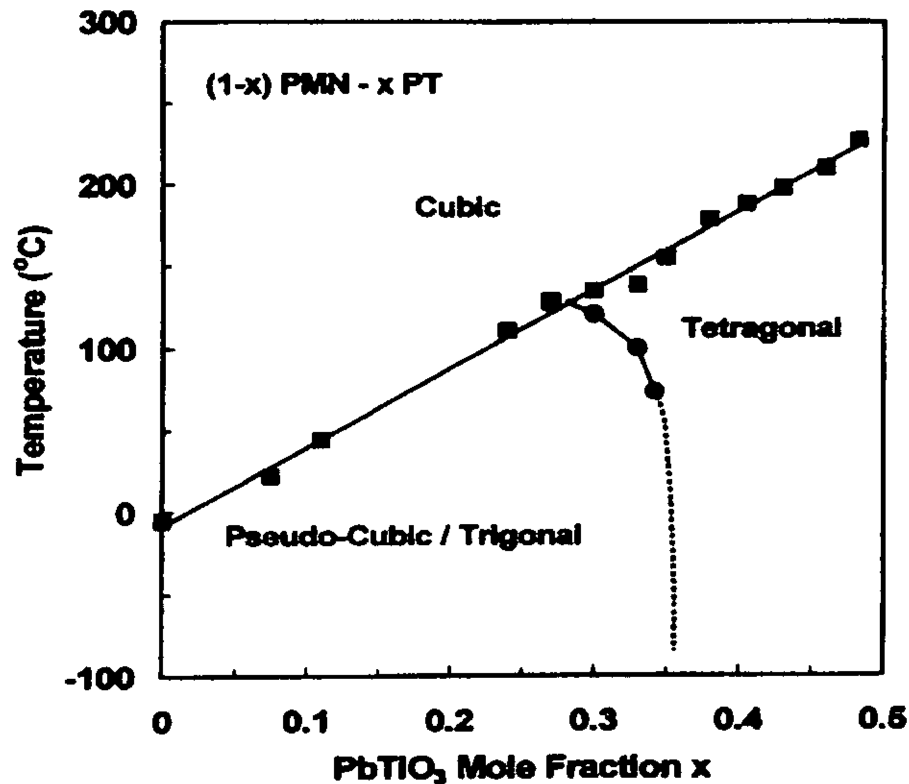

Fig. 1.3 The phase diagram of PMN-PT solid solution system (adapted from [Shrout et al., 1990]).

microelectromechanical systems (MEMS). Depending on the PT content, PMN_{1-x}-PT_x exhibits different electrical properties and can be utilized for different electrical device applications. By changing the content of $PbTiO_3$, the maximum dielectric constant occurs at varied temperatures ranging from -15°C to 492°C. For examples, $PMN_{0.9}$-$PT_{0.1}$ exhibit large dielectric constant at room temperature because its T_m is around 40°C. It can be used as a high-k dielectric capacitor. Besides, the boundary between the ferroelectric tetragonal and rhombohedral phases, known as a morphotropic phase boundary (MPB), which occurs at $x \sim 0.33$, PMN_{1-x}-PT_x exhibits maximum piezoelectric coefficient and dielectric constant [Park et al., 1997]. The

temperature at the dielectric maximum T_m, however, can be tuned from −15°C to over 145°C when x is increased from 0 to the MPB. On the other hand, the material behaves like a normal ferroelectric for $x \geq 0.4$ [Shrout et al., 1990b].

Preparation of high quality PMN_{1-x}-PT_x thin film has been difficult due to the presence of the undesirable pyrochlore phase, which causes the reduction of the dielectric and piezoelectric properties [Syamaprasad et. al., 1997]. The stable pyrochlore phases can be cubic pyrochlore $Pb_3Nb_4O_{13}$ (P_3N_4), rhombohedral pyrochlore $Pb_2Nb_2O_7$ (P_2N_2), and tetragonal pyrochlore $Pb_3Nb_2O_8$ (P_3N_2, non-ferroelectric) [Lavric et. al., 1998]. Nevertheless, epitaxial PMN_{1-x}-PT_x films has been grown on MgO [Tantigate et al., 1995] and $LaAlO_3$ (LAO) [Nagarajan et al., 1999] by pulsed laser deposition (PLD) and other methods, such as sol-gel spin-on method [Udayakumar et. al., 1995], sol-gel dip-coating method [Lu et. al., 1999], and metal organic chemical vapor deposition [Takeshima et. al., 1995]. Typically, the dielectric constant of PMN_{1-x}-PT_x films in the range of 800 to 2000 has been reported. For microelectronic applications, however, it is important to grow the relaxor ferroelectric on Si. In this project, we have focused on growing high quality epitaxial PMN-PT films by PLD method. Platinum and conducting oxide electrodes have been used. Their effects on PMN-PT film growth are examined and compared. Attempts on integrating the PMN-PT dielectric films with Si substrate via buffer layers are also presented.

1.3 Dynamic random access memory (DRAM)

The dynamic random access memory (DRAM) consists of one transistor and one capacitor (1T-1C) per bit. Fig. 1.4 illustrates the diagram of DRAM cell. The design of DRAM is simple and the cell is small. Data are stored in an array of capacitors at the intersection of columns of bit lines and rows of word lines. For a read operation, a 'sense' amplifier determines whether the capacitor was charged 1 or 0 and then by applying an appropriate voltage to rewrite that charge. DRAM is a volatile memory device because the charge in the capacitors will be lost gradually and the cells need recharging by a refresh operation [Ramesh, 1997].

A static random access memory (SRAM) stores data in a flipflop consisting of normal logic transistors. It is ready for another read cycle as soon as the first is complete. DRAM needs to write the data back into the cell after a read access and to perform precharge before the next attempt to read the device. The cycle time of a SRAM is faster than that of a DRAM. But SRAMs are a quarter the capacity of DRAMs for the same process technology and chip size. In addition, the cost of SRAM is about four times as much per bit as a DRAM. Therefore, the difference in cost and capacity between the two devices keeps the DRAMs in demand [Prince, 1996].

DRAM was patented in 1972 as a solid-state memory [Ramesh, 1997]. At the beginning, the material used for DRAM capacitor was SiO_2 and the design of DRAM was in planar geometry. The capacitance $C = \varepsilon_o\varepsilon_r A/d$, where ε_o and ε_r are the

permittivity of vacuum and the relative permittivity of the material, respectively. A and d are the area and the thickness of the capacitor.

The evolution of dynamic random access memories (DRAMs) with higher-level integration has been achieved by decreasing the size of the memory cell areas. The thickness of the dielectric has to be decreased to maintain the similar charge densities. As the size of DRAM device continues to shrink, low dielectric constant silicon dioxide and silicon oxynitride can no longer be used because of the physical limitations for their structure and thickness. Besides, large tunneling current sets in if the dielectric film is too thin. New high dielectric constant material is needed for further reduction of cell size. The high permittivity dielectric film would allow one to grow physically thicker films of similar capacitance like thin SiO_2 films. Ferroelectrics and related dielectrics have also been suggested for DRAM

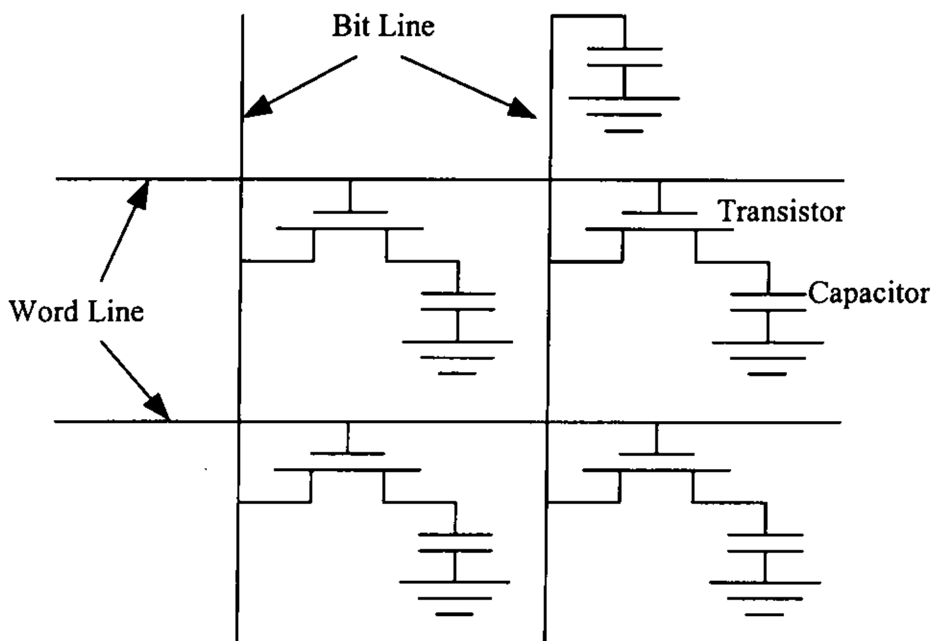

Fig. 1.4 Diagram of DRAM cell (redrawn from [Ramesh, 1997]).

applications. High dielectric perovskite structure materials such as $SrTiO_3$ [Abe et al., 1992], $(Ba_{1-x}Sr_x)TiO_3$ (BST) [Kawano et al., 1993], and $Pb(Zr_xTi_{1-x})O_3$ (PZT) [Hwang et al., 1996] have attracted much attention for charge storage capacitors. For DRAM applications, ferroelectric properties such as polarization hysteresis are not essential, only a high dielectric constant with good insulating properties is required [Joshi, 1993].

The International Technology Roadmap for Semiconductors (ITRS) has identified advanced high-*k* dielectric for DRAM stack capacitor for the immediate and medium term requirements (Table 1). Long-term projection beyond 2008, however, remains totally open.

Year	1999	2002	2005	2008	2011	2014
Technology node	180nm	130nm	100nm	70nm	50nm	30nm
DRAM capacity	1G	3G	8G	24G	64G	192G
Upper electrode	Poly-Si	TiN, TiON	Metal	Metal	Metal	Metal
Bottom electrode	Poly-Si	Metal	Metal	Perovskite	???	???
Capacitor dielectric material	Ta_2O_5	Ta_2O_5	BST	Epi-BST	???	???
Expected capacitor dielectric constant	22	50	250	700	1500	>1500

Table 1.1 DRAM Stack Capacitor Films Potential Solutions (Source: 99 ITRS)

In the giga-bit era, the cell size of DRAM is being scaled down faster than the general design rule. A cell footprint of $8F^2$ (F: Feature Size) needs to be realized at the below 200 nm node generation. Based on the assumption that a cell capacitance retains at least 25fF/cell to assure stable circuit function and sufficient soft-error immunity, the layer thickness of conventional SiO_2 with dielectric constant of 3-4 is reduced to <1nm. In such thickness the tunneling current is prohibitively large at > $1 A/cm^2$ and thus preclude the use of SiO_2 dielectric layers in future high density DRAMs. Instead high-*k* dielectric and metal counter-electrode are needed. Ta_2O_5 with a dielectric constant of 22 is a promising dielectric choice for this node. At the 100 nm node, a higher *k* material such as (Ba, Sr)TiO3 (BST) with a dielectric constant of about 200-250 will be needed. At the 70nm node, research and development for new materials such as epi-BST with a sufficiently high dielectric constant will be required. At the 50 nm node and beyond, a dielectric constant of 1500 is expected. Thus innovation of 'super high-*k*' value is called for and a new DRAM device structure that uses ferroelectrics with enormously large *k* value should be explored.

Fig. 1.5 presents the state-of-the-art ferroelectric DRAM technology (NEC). This is a tungsten silicide metallized BST DRAM with a very thin BST film (26 nm). The top and bottom electrodes are Ru, but the bottom has a thick ruthenium oxide-ruthenium sandwich structure cemented with TiN onto a polysilicon plug where TiN act as diffusion barrier [Scott, 2000].

For DRAM application, the main features for the dielectric capacitor were summarized as follows:

- Very high dielectric permittivity ε_r;
- Low dielectric loss (tan δ);
- Low leakage current;
- High breakdown strength;
- Full integration with Si.

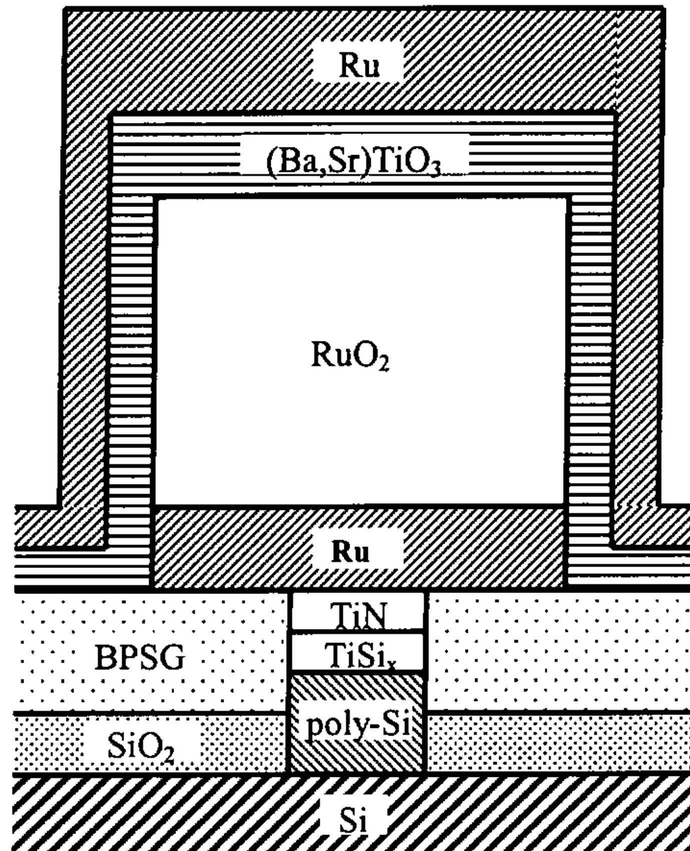

Fig. 1.5 NEC ruthenium/ruthenium oxide metallization for BST DRAM (redrawn from [Scott, 2000]).

1.4 Dielectric properties

The dielectric constant and dissipation factor are true material properties and can therefore be understood in terms of composition and structure, which define material behavior in an electric field. In the microscopic concept of polarization, the dielectric constant is related to the various polarizability mechanisms. The components of the polarizability are $\alpha = \alpha_e + \alpha_i + \alpha_o + \alpha_s$ representing susceptibilities associated with electronic, ionic, orientation, and space charge polarization, respectively.

Electronic polarization (P_e) is due to shifts or displacement of electron clouds away from their equilibrium position in the electric field, resulting in a net dipolar response. It occurs in all solids up to optical frequencies ~ 10^{16} Hz.

Ionic polarization (P_i) is only found in ionic substances such as sodium chloride. The molecules are formed of atoms having excess charges of opposite polarities. The relative position of positive and negative ions of a molecule will tend to shift in an electric field. It occurs up to the infrared region of 10^{10} - 10^{13} Hz.

Orientation polarization (P_o) is only found in substances that possess permanent dipole moments. The molecules or association of ions possess a dipole moment even in the absence of an applied field. Polarization results from a rotation of the permanent moments into the direction of the applied field.

Interfacial or Space Charge Polarization (P_s) usually arises from the presence of electrons or ions capable of migrating over distances of macroscopic magnitude. Some of these charge carriers will be trapped and accumulate at lattice defects, impurity centers, voids, strains, or at electrode surfaces, and then distort the field and produce an apparent increase in the dielectric constant. In heterogeneous or multiphase materials, interfacial polarization is of particular importance. Due to the differences in the electrical conductivity of the phases present, charges move through the more conducting phases and build up on the surfaces that separate these from the more resistive phases. Effectively each conducting region will become polarized so that there is an apparent increase in the average moment of the molecules given by $P_s = \alpha_s E$ where α_s is the interfacial or space charge polarizability. Space charge polarization typically occurs at low frequency (< 1kHz), but it can occur up to much higher (~ 10^5 Hz) frequencies in some case [Buchanan, 1991].

It has been discussed that the total polarization in any material is made up of four different components. The average dipole moment per molecule is given by $p = \alpha E$ where α is the total polarizability ($\alpha_e+\alpha_i+\alpha_o+\alpha_s$); E is the electric field intensity acting on each molecule. Then the electric polarization is given by $P = N\alpha E$ where N is the number of molecules per unit volume [Zaky et al., 1970].

Regarding to the dissipation factor of a capacitor, as a result of superposition of different loss mechanisms, thin film capacitor shows a general behavior of increasing loss at very low and very high frequencies, with a wide minimum in the intermediate frequency range. Losses in a bulk capacitor arise due to

: (1) the dielectric is not a perfect insulator, that is the losses due to the leakage resistance R_p of the capacitor, which is placed in parallel with C (this dc contribution to the dissipation factor is given by $1/\omega R_pC$, where ω is the angular frequency and is dominant at low frequencies); (2) ac dielectric loss consisting of a frequency-independent contribution present at all levels of loss, superimposed by ac relaxation peaks. The majority of the current is carried by defects, as is true in typical dielectric films, the frequency-independent loss is thought to be due to a wide range of distribution of relaxation processes in the film. Besides the leakage losses and the dielectric losses, there is another source of loss which is very dominant in thin film capacitors. This arises from the resistance R_s of the electrodes, which is placed in series with the capacitance C. The loss due to electrode resistance is given by ωCR_s and is significant at high frequencies. Within certain limits, the high-frequency characteristics of thin film capacitors can be improved by using highly conductive and thicker electrodes [Chopre et al., 1983].

1.5 Outline of thesis

In the present study, the structural and electrical properties of PMN-PT with $La_{0.7}Sr_{0.3}MnO_3$ (LSMO) and $BaPbO_3$ (BPO) bottom electrodes fabricated on LAO, MgO, Si and Pt/Si substrates will be investigated.

In chapter two, the history of PLD and the basic mechanism of film growth will be introduced. Besides, the advantages and disadvantages of PLD will be explicitly presented.

The experimental set-up will be presented in chapter three. The working principle of some major characterization equipment such as X-ray diffractometry (XRD) will be discussed. Leakage current and dielectric measurements will also be described.

In chapter four, we describe the fabrication of PMN-PT films on LAO(001) single crystal using conducting LSMO perovskite as bottom electrode. The structural and electrical properties of $PMN_{0.9}$-$PT_{0.1}$ and $PMN_{0.65}$-$PT_{0.35}$ films grown on LSMO/LAO will be reported. Then, the structural and the electrical properties of thickness dependence of $PMN_{0.9}$-$PT_{0.1}$ grown on LSMO/LAO will also be discussed.

Temperature dependence of epitaxial $PMN_{0.9}$-$PT_{0.1}$/LSMO/MgO will be reported in chapter five. The heterostructure of $PMN_{0.9}$-$PT_{0.1}$/LSMO/MgO/TiN/Si has also been fabricated and their structural and electrical properties will be revealed at the end of this chapter.

In chapter six, $PMN_{0.9}$-$PT_{0.1}$ has been grown on LAO and MgO single crystal substrate with BPO conducting oxide bottom electrode. $PMN_{0.9}$-$PT_{0.1}$with BPO and LSMO oxide electrodes have been grown on top of Pt/Si substrates. Their structural and electrical properties as functions of growth conditions will be presented.

Finally, conclusion of the experimental results and suggestions for future works will be given in chapter seven.

Chapter Two

Pulsed Laser Deposition (PLD)

2.1 Introduction

There are various methods to deposit thin films for different optical and electronic devices. Thin film growth technique can be broadly divided by chemical vapour deposition (CVD) and physical vapour deposition (PVD) methods. Chemical depositions involve chemical reactions and/or exchanges during film formation. Chemical vapour deposition method includes hydride CVD, trichloride CVD, metal-organic CVD, and sol-gel fabrication. On the other hand, physical vapour depositions (PVD) only involve physical transfer of material from a target to the surface of a substrate. PVD includes pulsed laser deposition (PLD), molecular beam epitaxy (MBE), electron-beam sputtering, ion-beam sputtering, magnetron sputtering, and thermal evaporation. In this chapter, the history of PLD will be introduced first, and then a brief description of basic mechanism will be given. Finally, the advantages and disadvantages of PLD will be presented.

2.2 History of PLD

Laser ablation was developed since 1965. The first experiment was demonstrated by Smith et al. [Smith et al., 1965]. In 1970's, the invention of

electronic Q-switch and the development of high efficiency second harmonic generator made laser ablation suitable for growing high quality films and brought PLD to a new era. In subsequent years, Gaponov deposited oxide films in an oxidizing ambient in late 1970's [Gaponov et al., 1979].

Major breakthrough came at 1987 when the successful growth of high T_c superconducting films by PLD led to numerous studies. The pioneering work was done by Venkatesan of Bellcore [Dijkkamp et al., 1987]. After that time, many experiments were done and initiated an explosive growth in PLD. The work includes the heteroepitaxy of oxide films on semiconductors such as YSZ/Si [Fork et. al., 1992], the growth of ferroelectric perovskite oxide films [Ramesh et. al., 1990], and epitaxial grow of TiN on Si(100) substrates [Narayan et. al., 1992]. Also, production-related issues regarding reproducibility [Cheung et. al., 1992] and large-area scale-up [Greer et. al., 1990] have also been addressed. In addition, interest has been sustained and broadened by the concurrent development of high-power pulsed ultraviolet (UV) excimer lasers that are reliable and convenient to use.

2.3 Mechanisms of PLD

Figure 2.1 shows the schematic diagram for laser ablation. It consists of a vacuum chamber, target holder and substrate holder. A high-power pulsed laser is focused on the surface of a target. The ablated materials form a luminous plasma plume and are collected by a heated substrate to produce a desired crystalline film.

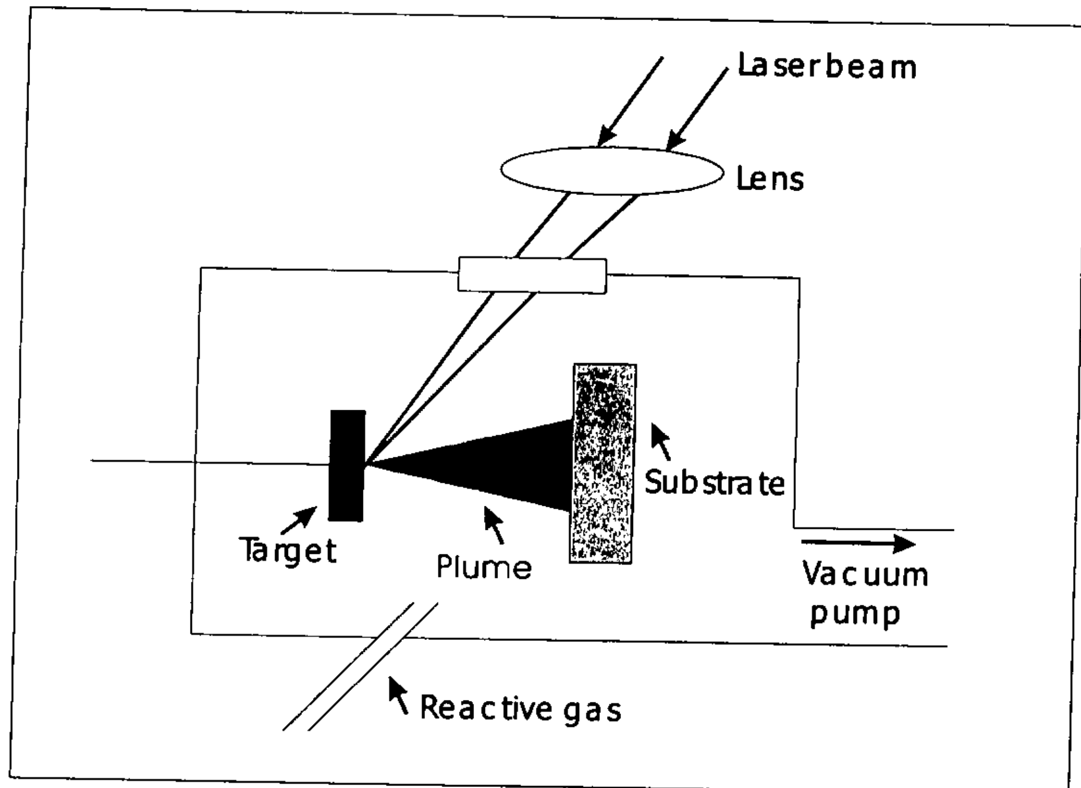

Fig. 2.1 Schematic diagram for laser ablation.

The mechanism of PLD is a very complex physical phenomenon. In general, the thin film formation process in PLD can be divided into four stages. They are laser radiation interaction with the target, dynamics of the plasma plume, interaction of the plasma plume with the substrate, and nucleation and growth of a thin film on the substrate surface. All stages are important for the formation of a high quality thin film.

2.3.1 Laser radiation interaction with the target

The mechanisms of laser ablation involve many complex physical phenomena such as collisional-, thermal-, and electronic-excitation, exfoliation and

hydrodynamics. The laser focused onto the surface of target material with high fluence. Sufficiently high flux densities and short pulse duration lead to local heating and evaporation of target material. Materials are dissociated from the target surface and ablated out with stoichiometry as in the target. The ablated plume consists of a mixture of energetic species including atoms, molecules, electrons, ions, clusters, micron-sized solid particulates, and molten globules.

2.3.2 Dynamics of the plasma plume

The ablated materials from the target tend to move towards the substrate according to the laws of gas-dynamic and show the forward peaking phenomenon [Namiki et al., 1986]. Singh et al reported that the spatial thickness varied as a function of $cos\theta$ [Singh et al., 1990]. The uniformity of film is significantly depending on the spot size of the laser and the plasma temperature. The target-to-substrate distance also governs the angular spread of the ablated materials and it affects the profile and homogeneity of the film.

2.3.3 Interaction of the plasma plume with the substrate

Interaction of the plasma plume with the substrate affects both the quality and the stoichiometry of thin films. The energetic species of the plume sputter some of the surface atoms forming a collision region between the incident flow and the sputtered atoms. This thermalized region serves as a source for condensation of particles. When the condensation rate is greater than the sputtering rate, thermal

equilibrium condition can be reached quickly and film grows on the substrate surface at the expenses of the direct flow of the ablation particles.

2.3.4 Nucleation and growth of a thin film on the substrate surface

There are three conventional modes of film nucleation and growth: (i) three-dimensional island growth (Volmer-Weber), (ii) two-dimensional full-monolayer growth (Frank-van der Merwe), and (iii) two-dimensional growth of full monolayers followed by nucleation and growth of three-dimensional islands (Stranski-Krastinov). According to Greene [Greene, 1993], the selection of one of these growth modes by a substrate-film system depends (a) on the thermodynamics relating the surface energies (film and substrate), and (b) the film-substrate interface energy. The two main thermodynamic parameters for the growth mechanism are substrate temperature and supersaturation.

The nucleation process depends on the interfacial energies between the three phases present – substrate, condensing material and vapour. The critical size of the nucleus depends on deposition rate and substrate temperature. For small supersaturation, the nucleation process creates isolated patches (islands) on substrates. These patches subsequently grow and coalesce together forming large nuclei. As the supersaturation increases, the critical nucleus shrinks until its height reaches atomic diameter such that its shape is two-dimensional. For even larger supersaturation, the layer-by-layer nucleation will happen for incompletely wetted foreign substrates.

The crystalline film growth depends on the surface mobility of adatom (vapour atoms). The substrate temperature determines the adatom's surface diffusion ability. High temperature favors rapid and defect-free crystal growth. Low temperature or large supersaturation crystal growth causes disordered or even amorphous structures.

2.4 Advantages and disadvantages of PLD

In general, PLD is a relatively simple method to prepare thin films. The most important advantage of PLD is that stoichiometric films can be easily fabricated because the "congruent" evaporation of the target material by extremely high heating rate at the target surface due to pulsed laser irradiation. Since the ablated species are highly energetic, lower substrate temperature can be used to grow crystalline films. With the choice of an appropriate laser, PLD can also be used to grow thin film of any kind of materials. A multiple targets system can be loaded inside the deposition chamber and it is easy to fabricate in-situ heterostructure thin films. Different kinds of gas can be introduced into the deposition chamber to form a reactive environment for fabricating different materials. For growing oxide thin films, oxygen is provided during the film growth process.

On the other hand, there are disadvantages in using PLD method. One of the main problems is the formation of particulates on the films. The size of the particulates can be as large as a few microns. But this problem can be reduced by

placing a shadow mask to block off the particulates. Besides, PLD method cannot grow large area films uniformly because the narrow angular distribution of the ablated plume. A larger uniform film can, nevertheless, be produced by laser beam scanning [Greer et al., 1990] and by substrate scanning [Davis et al., 1991].

In general, PLD is a versatile technique for preparing a wide range of thin films and multi-layer structures. Different materials in thin film form can be fabricated by PLD. This makes PLD a powerful deposition technique in thin film research.

Chapter Three

Experimental Set-up and Measurements

3.1 Introduction

In this project, all thin films are fabricated by PLD method. Structural characteristics of the heteroepitaxially grown PMN-PT capacitors are examined by X-ray diffractometry (XRD). The surface morphology and cross section of the films are examined by scanning electron microscopy (SEM). The leakage current is measured by a Digital Electrometer TR8652. The capacitance against frequency is measured by an impedance / gain-phase analyzer (Hewlett Packard 4194A).

3.2 Experimental set-up and procedure

The instrument for pulsed laser deposition consists of a 248 nm Krypton Fluoride (KrF) excimer laser (Compex 205, Lamda Physik), a vacuum chamber, substrate holder, target holder, and optics. The experimental set-up used in the present PLD experiments is shown in Fig. 3.1.

A mechanical rotary pump (ULVAC D-330K) was used to pump down the pressure of the chamber to about 10mTorr. Then the chamber can be evacuated by a cryro-pump (CTI-CRYOGENICS CRYO-TORR 8) to 2×10^{-6} Torr. For the pressure

of the chamber in the range of 10 – 0.001 Torr, it was monitored by a Baratron pressure gauge (MKS Baratron Type 122A). For the pressure lower than 0.001 Torr, it was measured by an ionization gauge (ULVAC Type WI-T).

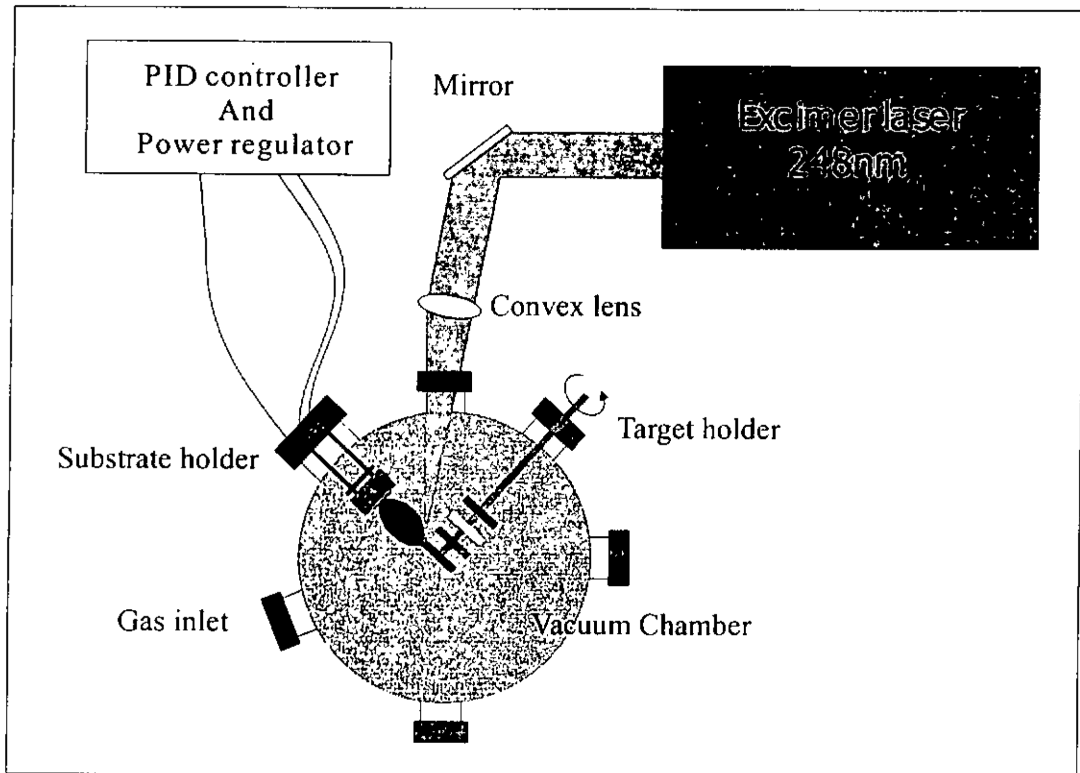

Fig. 3.1 Experimental set-up of PLD

The KrF excimer laser emits high flux of UV photons. The gases used were F_2, Kr and Ne with partial pressure of 4mBar, 130mBar and 3210mBar, respectively. The wavelength of KrF excimer laser is 248nm and the laser energy can be up to 700mJ per pulse. The laser beam was guided into the deposition chamber through fused silica window by a UV-grade mirror and a convex lens. The mirror is a dielectric multi-layer coated laser grade optical glass and it has high reflectivity of

excimer laser line at 45° incident angle. The focal length of the lens is 50 cm and the laser fluence can be adjusted by changing the position of the lens. The laser beam was focused onto a rotating target at an angle of 45°. The windows of the chamber are made of UV-grade fused silica that the transmittance of the excimer laser can be up to 90%.

The oxidizating gas, such as O_2, was flowed through the gas inlet into the deposition chamber. The targets were mounted with a rotating shaft through the center. The distance between targets and substrate holder was about 5 cm. During deposition, the target holder was rotated continuously to ensure that the surface of the target was evenly ablated and to prevent pitting on the target surface. By slide in and out the shaft for target selection, in situ multi-layer films could be fabricated.

The substrate heater was made of stainless steel and the heating filament was Kanthal wire (25% chromium, 5% aluminum, 3% cobalt and 67% iron) with total resistance of about 12 Ω. The diameter of the Kanthal wire was 0.559 mm and the resistance per unit length was 5.1 $\Omega\ m^{-1}$. A K-type (Nickel-Chromium, Nickel-Aluminum) thermocouple was placed into the heating block for the measurement of the substrate temperature and the temperature was controlled by a PID controller (Shimaden SR-19) and a power regulator (PAC25-0321).

Four different substrates were used in this studied, they were $LaAlO_3$ (LAO), MgO, Si, and Pt/Si. Before deposition, all substrates were immersed in acetone and degreased by ultrasonic. Only Si substrate was etched by 10% HF for 5

minutes then rinsed by deionized water. The substrates were then adhered on the heater face-plate with high-temperature silver paste which can act as a heat conducting medium. The substrate temperature was measured by placing a thermocouple just below the face-plate of the heater. To fabricate different films, different deposition processing parameters were required to obtain good quality films. Some materials required high vacuum condition (TiN, MgO) and some of them needed to deposit at oxygen ambient (LSMO, BPO, PMN-PT). To fabricate TiN or MgO, the chamber was evacuated by a rotary pump to approximately 10 mTorr, then the pressure of the chamber was pumped down by a cryo-pump to 5×10^{-6} Torr. For the fabrication of LSMO, BPO, and PMN-PT, the films were deposited under 150, 100 and 200 mTorr ambient oxygen pressure, respectively. During deposition, the choice of deposition time and laser repetition rate can control the thickness of the thin films. The detail deposition conditions of different films will be discussed in corresponding chapters.

3.3 Characterization of thin films

3.3.1 X-ray diffractometry (XRD)

X-ray diffractometry (Philip X'pert system) is a common and non-destructive method for characterization of crystal structure. It can be used to determine the atom location of bulk solids, powders, or thin films. The XRD system was operating both in four-circle and Bragg-Brentano (2θ–θ) geometries. The X-ray was the K_α radiation of Cu with wavelength of 1.54Å. The K_β line was filtered off by

appropriate Ni filter. This XRD performs several modes of scanning. The 2θ-θ scan was used to determine the crystal phase formed with the orientation normal to the substrate surface. The out-of-plane orientation of the PMN-PT (200) peaks was examined by ω–scan. Smaller full width at half maximum (FWHM) of ω–scan profile means better quality in orientation of the films. The XRD ϕ–scan was performed to confirm epitaxial growth of the films.

Fig. 3.2 shows a schematic diagram of X-ray diffraction of a crystal. The X-ray radiation from the X-ray source interacts with the atoms. Each atom scatters a small fraction of the incident beam. The scattered beams from all atoms in the crystal planes involved may interfere. From the figure, a constructive interference happens when

$$AB + BC = n\lambda,\ n = 1,2,3,\ldots$$

where n is an integer and λ is the X-ray wavelength. Since $AB = BC = d\ \sin\theta$, it follows Bragg's Law

$$2d\sin\theta = n\lambda,\ n = 1,2,3,\ldots$$

where d is the interplanar spacing, θ is the angle between the X-ray beam and the crystal plane, and n is the order of the intensity maximum.

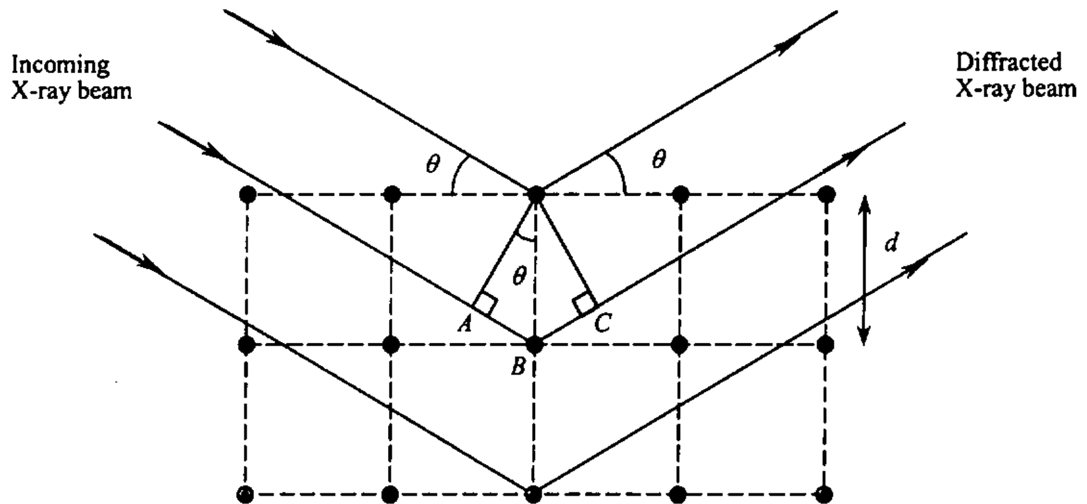

Fig 3.2 Bragg diffraction of X-rays from successive planes of atoms. Constructive interference occurs for *ABC* equal to an integral number of wavelengths.

For simple cubic structure, the interplanar spacing d can be determined by the following equation

$$d = \frac{a}{\sqrt{h^2 + k^2 + l^2}}$$

where a is the lattice constant of the crystal structure and h, k and l are the reciprocal lattice indices for a, b, c axis, respectively.

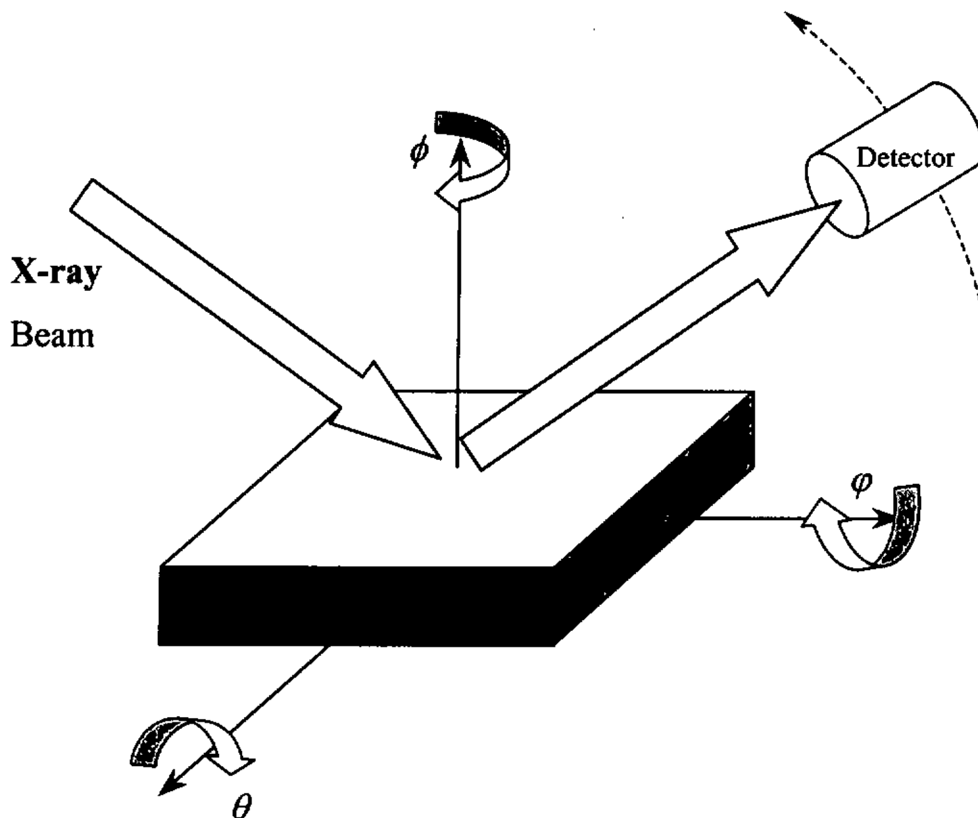

Fig. 3.3 The rotation axes of the sample relative to the X-ray emitter and detector.

The X-ray diffractometry (XRD) consists of the X-ray source, different kinds of slits, monochromator and detector. There are four rotation axes, they are θ (ω), 2θ, φ and ϕ for different scan modes as shown in Fig 3.3. Three different scan modes, 2θ–θ, ω and ϕ scans, were performed to investigate the quality of the films in this project.

For the 2θ–θ scan, the position of the X-ray source is fixed, the sample rotates a certain angle with respect to the X-ray beam axis and the detector rotates twice of that angle. It allows us to observe the lattice planes of the thin films grown with the direction parallel to the normal direction of the substrate surface. The

diffraction profile reflects the crystal structure of the materials. Then we can determine the crystalline phases and orientations. The 2θ–θ scan gives information on the out-of-plane crystalline orientation of the film.

To obtain quantitative measurements of orientations, ω scan is performed. It gives the degree of random orientation of the crystal grains with each other in the films. On the other hand, it allows us to know how good the film is oriented. ω scan is carried out by fixing the 2θ value of the selected peak and the angle θ is scanned for a few degree. The strong diffraction appears when a particular plane of the grain is aligned at the angle matching the Bragg's Law. Therefore, a broader profile will be obtained for worse-aligned grains than a better-aligned one. The ω scan profile is usually referred as the rocking curve. The value of the full width at half maximum (FWHM) of the rocking curve reflects the degree of the orientation of the thin films. A narrow profile (smaller FWHM) means the film has better orientation. A film can be considered as highly oriented if the FWHM of the rocking curve is less than or around 1°. For comparison, the FWHM of ω scan of single crystal like LAO or Si substrate is about 0.2° in our XRD system.

2θ–θ and ω scan can only provide limited information of crystal planes paralleled to the surface and out-of-plane lattice spacing characteristics. If we observe diffraction peaks from a single family of planes in the 2θ–θ scan, it is not sufficient to determine whether the thin films are epitaxially grown or just randomly oriented on the substrates. Therefore, ϕ scan is performed to retrieve this

information. For a film with simple cubic structure, in carrying out the ϕ scan, the specimen angle φ should be tilted to 45° and fixing the 2θ and θ angles corresponding to the (202) crystal plane of the films or substrates. Then a 360° ϕ scan is performed to investigate the peaks and identifies its four-fold symmetric feature. From the ϕ scan profiles, the film was cube-on-cube epitaxially grown on substrate if the peaks were 90° apart and both peaks from the film and substrate aligned at same angles.

3.3.2 Scanning electron microscopy (SEM)

The surface morphology and cross section of the films were investigated by scanning electron microscopy (SEM, Leica stereoscan 440). The film thickness can be determined from the cross section image. Its principle maximum amplification is about 300,000. Under this amplification, grains size ~ 20-30 nm can be just resolved.

In SEM, the detector collects electrons that are knocked out of the specimen atoms by the electron beam. The signal from detector is then amplified by circuitry and synchronized with the scan generator to produce an image. For non-conducting specimen such as PMN-PT film, sharper image can be obtained by coating a thin layer of gold of about 10 nm, which can increase the emission of secondary and backscattered electron, reduce the thermal damages as well as eliminate specimen charging. Therefore, details of surface morphology or cross section of the deposited thin films can be obtained.

3.3.3 Surface profiling

The thickness of the thin films can be determined from the SEM cross-sectional image of the films. Film thickness can also be measured directly by Alpha-step profiler (Tencor Instrument, model P-10). The principle of Alpha-step is to move a very fine needle across the step and detect the thickness profile of the film as shown in Fig. 3.4. The highest resolution of this instrument is less than 1 nm. In order to use this method to measure film thickness, a sharp step on the film is needed. Therefore, a mask should be placed to produce a sharp step on the film during deposition.

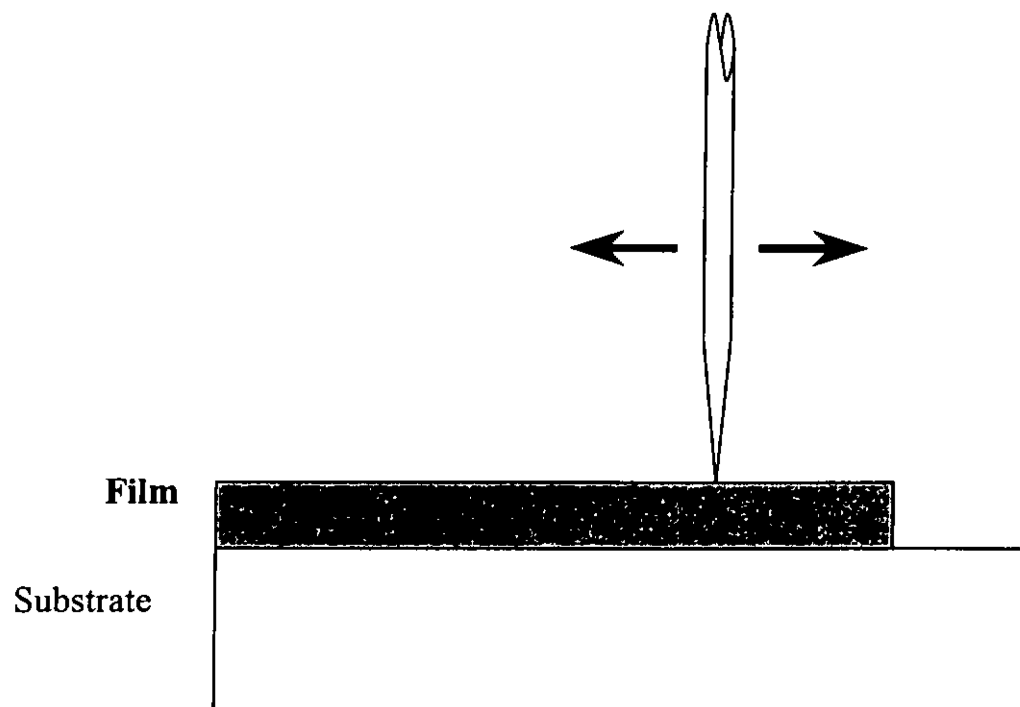

Fig 3.4 Film thickness measurement by Alph-step surface profiler.

3.3.4 Leakage current measurement

Leakage current is the most important feature for DRAM application. A DRAM dielectric needs a small leakage current to obtain large capacitance density and long retention time. In particular, the leakage current needs to be small enough such that the leakage through the capacitor will be less than 10% of the charge on the capacitor before a refresh cycle.

In order to measure the electrical properties of PMN-PT film, 0.2 mm diameter Au top-electrodes were sputtered onto the films. The leakage current against voltage was measured by a Digital Electrometer, Advantest TR8652. By connecting the two terminals of the meter across the top and bottom electrodes of the dielectric layer and increasing the driving voltage gradually, the leakage current against voltage curve can be obtained. For DRAM application, the leakage current density (leakage current per unit area) should be as low as 10^{-7}A/cm^2 at 1V.

3.3.5 Dielectric measurement

For a parallel-plate capacitor, the capacitance $C = \varepsilon_0\varepsilon_r A/d$, where ε_0 and ε_r are the permittivity of vacuum and the relative permittivity of the material, respectively, A and d are the area and the thickness of the capacitor. ε_r is also referred to as dielectric constant of the material and it shows the degree of polarizability or charge storage capability of the material. The dielectric constant is related to temperature, and the frequency of the applied field.

To obtain the dielectric constant of samples, we have to measure the capacitance first. Then the dielectric constant of PMN-PT film can be evaluated by simple calculation. The capacitance against frequency was measured by an impedance / gain-phase analyzer (Hewlett Packard 4194A).

Chapter Four

Fabrication and Characterization of PMN_{1-x}-PT_x on LAO Single Crystal Substrate

4.1 Introduction

During the course of DRAM capacitor development, the size (area) of the capacitor cell keeps on reducing rapidly for packing more units in the same IC. Since the capacitance $C = \varepsilon_o\varepsilon_r A/d$ and in order to maintain the capacitance at a certain value, the capacitor thickness should be reduced. However, there is a limit to the reduction because large tunneling leakage current occurs if the film is too thin. So on one hand we want to decrease A, but on the other we need to keep a large d. The only way out is to use materials that have big ε_r.

PMN is a well known relaxor ferroelectric that has large and broad dielectric peak at around −15°C. Its solid solution with lead titanate $PbTiO_3$ (PT), PMN_{1-x}-PT_x is also relaxor ferroelectric for $x < 0.4$ [Nomura et al., 1982].

The solid solution PMN_{1-x}-PT_x exhibits different electrical properties and can be utilized for different electrical device applications depending on the PT content. $PMN_{0.9}$-$PT_{0.1}$ exhibits large dielectric constant at room temperature because

its T_m is around 40°C. At the MPB, i.e. $PMN_{0.65}$-$PT_{0.35}$ also exhibits large dielectric constant but its T_m is at ~145°C [Park et al., 1994].

In this chapter, we describe the epitaxial growth and characterization of PMN-PT films. LAO(001) single crystal and conducting $La_{0.7}Sr_{0.3}MnO_3$(LSMO) perovskite are used as substrate and electrode, respectively. We choose LSMO as the bottom electrode because it exhibits good crystallinity, thermal stability and high electrical conductivity. It has a reasonably low resistivity of about 300 μΩ cm at room temperature [Wu et al., 1999]. Its pseudo-cubic structure with lattice constant of 3.8 Å matches closely to that of LAO(3.79 Å) and PMN-PT(3.9 Å – 4.03 Å).

Two different compositions of PMN_{1-x}-PT_x have been grown on LSMO/LAO. They are $PMN_{0.9}$-$PT_{0.1}$, and $PMN_{0.65}$-$PT_{0.35}$. After the deposition, the structure and electrical properties of the PMN-PT films are measured at room temperature and compared. In addition, $PMN_{0.9}$-$PT_{0.1}$ films of different thickness, ranging from 70nm to 450nm, are also prepared on LSMO/LAO. Their structural and electrical properties as function of film thickness are also examined.

4.2 PMN_{1-x}-PT_x/LSMO/LAO

4.2.1 Fabrication and structural characterization of thin films

The ceramic targets of LSMO, $PMN_{0.9}$-$PT_{0.1}$ and $PMN_{0.65}$-$PT_{0.35}$ were prepared by solid-state reaction method. The chemicals of La_2O_3, $SrCO_3$, and MnO_2

were used for the reaction to form the required LSMO compound. The mixed LSMO powder was then ball milled in acetone for 4 hours to ensure homogeneous distribution. The powder was then put into a crucible and put in the furnace with the following sintering conditions. Re-grounding of the powder between sintering was done using agate mortar.

Number of sintering	1	2	3
Sintering temperature (°C)	1200	1260	1320
Time for sintering (hours)	4	12	10

Table. 4.1 Sintering conditions of LSMO target.

After the second time of sintering, the powder was pressed into 1 inch diameter pellet by an oil-compressor at a pressure of 4 Tones.

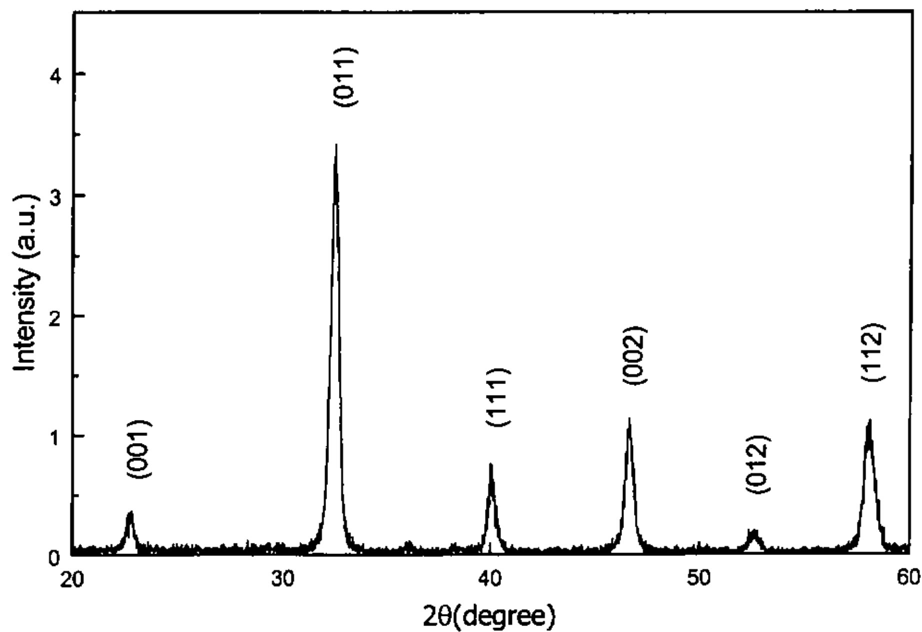

Fig. 4.1 The XRD 2θ-θ profile LSMO target.

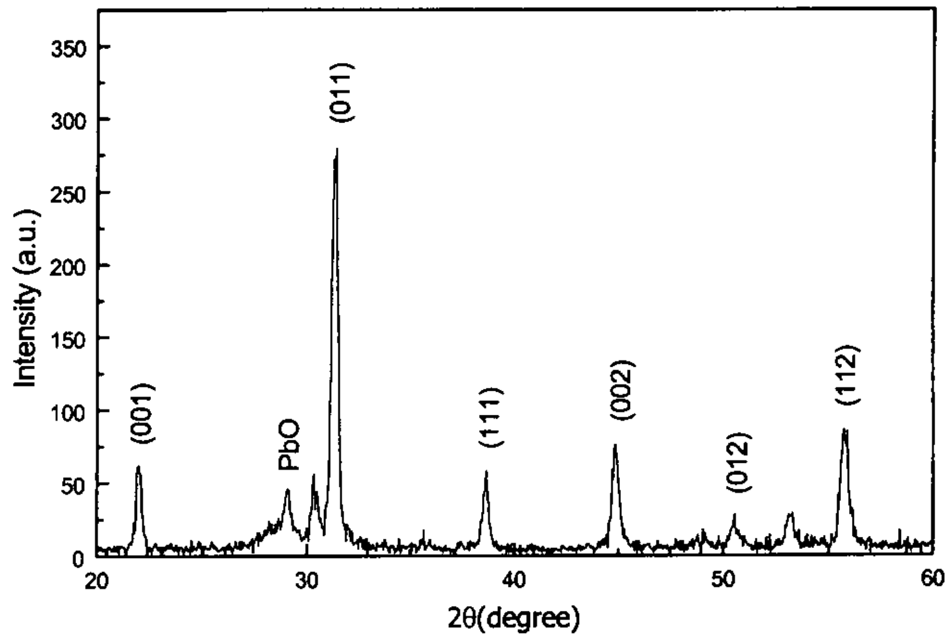

Fig. 4.2 The XRD 2θ-θ profile $PMN_{0.9}$-$PT_{0.1}$ target.

The ceramic targets of $PMN_{0.9}$-$PT_{0.1}$ and $PMN_{0.65}$-$PT_{0.35}$ were prepared by mixing PbO, MgO, Nb_2O_5 and TiO_2 powder. The powder was ball milled and sintered at 850°C for 2 hours. The power was then pressed into pellet and sintered at 1000°C for 1 hour.

The LSMO, PMN-PT targets were examined by energy-dispersive X-ray spectrometer (EDX) and their nominal composition were determined to be $La_{0.7}Sr_{0.3}MnO_3$, $0.9Pb(Mg_{1/3}Nb_{2/3})O_3$-$0.1PbTiO_3$ and $0.65Pb(Mg_{1/3}Nb_{2/3})O_3$-$0.35PbTiO_3$. The crystalline structure of the LSMO, $PMN_{0.9}$-$PT_{0.1}$ and $PMN_{0.65}$-$PT_{0.35}$ targets were then characterized by XRD. The XRD diffraction lines are

identified and shown in Fig. 4.1 and Fig. 4.2. The XRD diffraction profile of $PMN_{0.65}$-$PT_{0.35}$ targets (not shown in here) shows similar pattern with $PMN_{0.9}$-$PT_{0.1}$.

For the fabrication of the bottom electrode LSMO films, the laser repetition rate and energy density used were 10Hz and 4 Jcm^{-2}, respectively. During the deposition, the substrate was kept at 650°C. The laser ablation was carried out under an ambient oxygen pressure of 150 mTorr. For the fabrication of PMN-PT, 6 Hz laser repetition rate and 4 Jcm^{-2} radiation energy density were used. The films were deposited under 200 mTorr ambient oxygen pressure and the deposition temperature was also set at 650°C. No post-deposition annealing was performed. The as-deposited heterostructure of $PMN_{0.9}$-$PT_{0.1}$/LSMO/LAO and $PMN_{0.65}$-$PT_{0.35}$/LSMO/LAO films thus obtained were examined by different characterization method. The thickness of PMN-PT and LSMO films are 450, and 150 nm, respectively.

The XRD 2θ-θ profile of the $PMN_{0.9}$-$PT_{0.1}$/LSMO/LAO and $PMN_{0.65}$-$PT_{0.35}$/LSMO/LAO films are showed in Fig. 4.3. Highly oriented single perovskite phase of PMN-PT films have been obtained. The diffraction peaks of the PMN-PT films shift to larger angular value for increasing PT content. That means the out-of-plane lattice constant decreases with increasing PT content. By simple calculation, the lattice constant for $PMN_{0.9}$-$PT_{0.1}$, and $PMN_{0.65}$-$PT_{0.35}$ are 0.401, and 0.398 nm, respectively. These values agree with Lu's result [Lu et al., 1999].

The dependence of the lattice constant with increasing PT content in the rhombohedral range ($x \leq 0.33$) and in the tetragonal range ($x \geq 0.35$) coincides well with results obtained in bulk samples [Noblanc et al., 1996]. The c/a–axis is measurable for many tetragonal materials such as (Pb, La)(Zr, Ti)O_3 (PLZT) [Floquet et al., 1998]. However, it is not seen in our PMN-PT samples. One possible reason is that of the small c/a–axis ratio of PMN-PT (less than 1.01), where the c/a–axis ratio of PLZT is about 1.05 [Floquet et al., 1998]. Besides, our XRD equipment does not have high enough resolution to distinguish these two closely positioned peaks.

The out-of-plane orientation of the PMN-PT (002) peaks were examined by ω–scan. The full width at half maximum (FWHM) of the rocking curve are 1.1° and 1.2° for $PMN_{0.9}$-$PT_{0.1}$, and $PMN_{0.65}$-$PT_{0.35}$, respectively. These values reveal that the orientation of $PMN_{0.9}$-$PT_{0.1}$, and $PMN_{0.65}$-$PT_{0.35}$ films are quite good.

The XRD ϕ–scan of the PMN-PT(202), LSMO(202), and MgO(202) were performed to confirm the epitaxial relationship of the films. The 360° ϕ–scans of $PMN_{0.9}$-$PT_{0.1}$/LSMO/LAO are shown in Fig. 4.4. All profiles display features of 4-fold symmetry of a cubic structure, i.e. diffraction peaks are separated by 90°. We can also see that the peaks of different layers appear at the same angular position. This indicates that the films are cube-on-cube growth on LAO(001) substrate. It shows an in-plane epitaxial relationship of $(001)_{PMN0.9\text{-}PT0.1} \| (001)_{LSMO} \| (001)_{LAO}$.

Similar heteroepitaxial relationships are also obtained for $PMN_{0.65}$-$PT_{0.35}$/LSMO/LAO films.

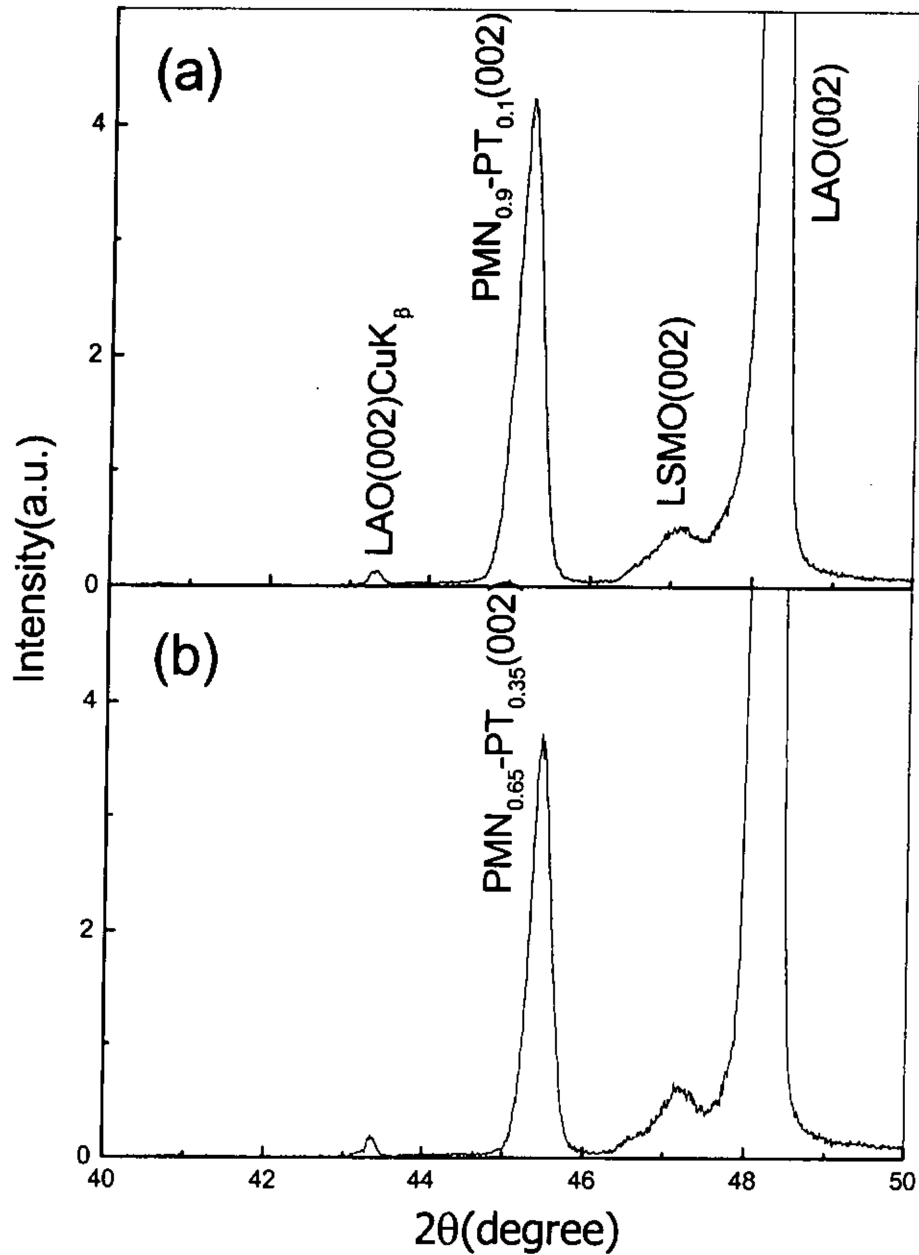

Fig. 4.3 The XRD 2θ-θ profile of the $PMN_{0.9}$-$PT_{0.1}$/LSMO/LAO and $PMN_{0.65}$-$PT_{0.35}$/LSMO/LAO films.

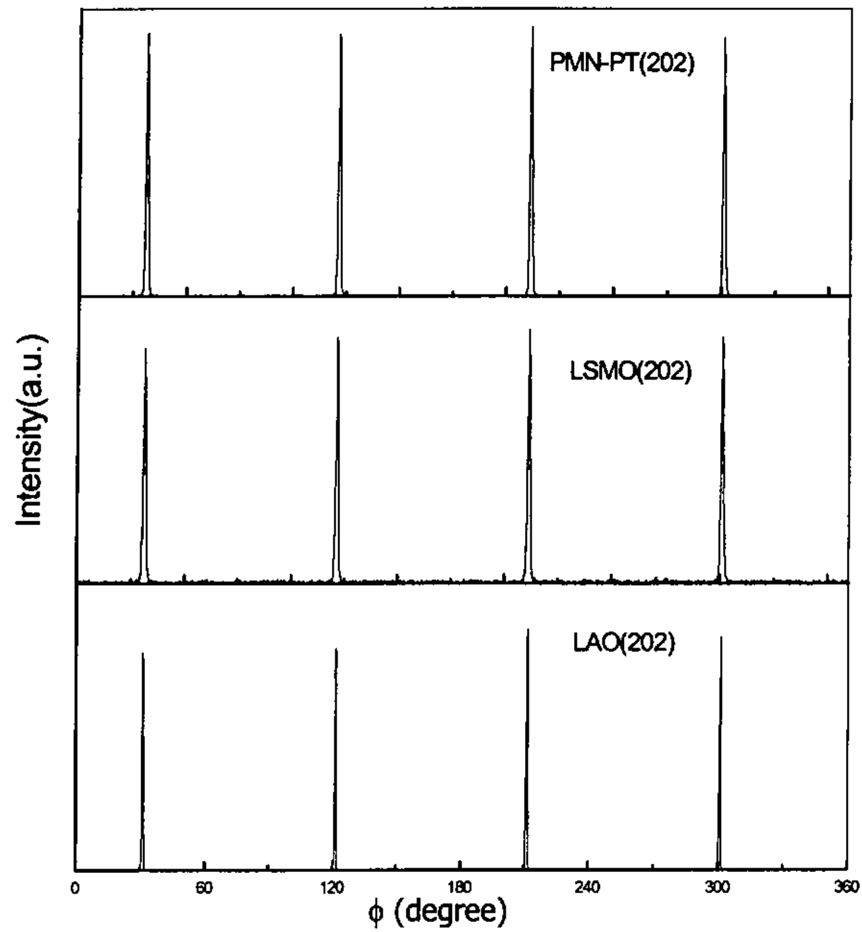

Fig. 4.4 The ϕ–scan of the $PMN_{0.9}$-$PT_{0.1}$(202), LSMO(202), and LAO(202).

4.2.2 Electrical properties

4.2.2.1 Leakage current measurement

For DRAM application, the leakage current density should be kept as low as 10^{-7}A/cm^2 to 10^{-6}A/cm^2 to avoid undue heating and power consumption [Kotecki, 1997]. Fig. 4.5 shows the leakage current density versus applied voltage for the heterostructures of $PMN_{0.9}$-$PT_{0.1}$/LSMO/LAO and $PMN_{0.65}$-$PT_{0.35}$/LSMO/LAO. From the figure, the leakage current density of $PMN_{0.65}$-$PT_{0.35}$ film is slightly larger than that of $PMN_{0.9}$-$PT_{0.1}$. The values of leakage current density at 1V and 5V are summarized in Table 4.2. For both films, the leakage current density remains at below 10^{-7} A/cm^2 for the applied voltage smaller than 1.6V, but increases dramatically for the applied voltage larger than this voltage. This breakdown voltage may be caused by local micro-breakdown of the films.

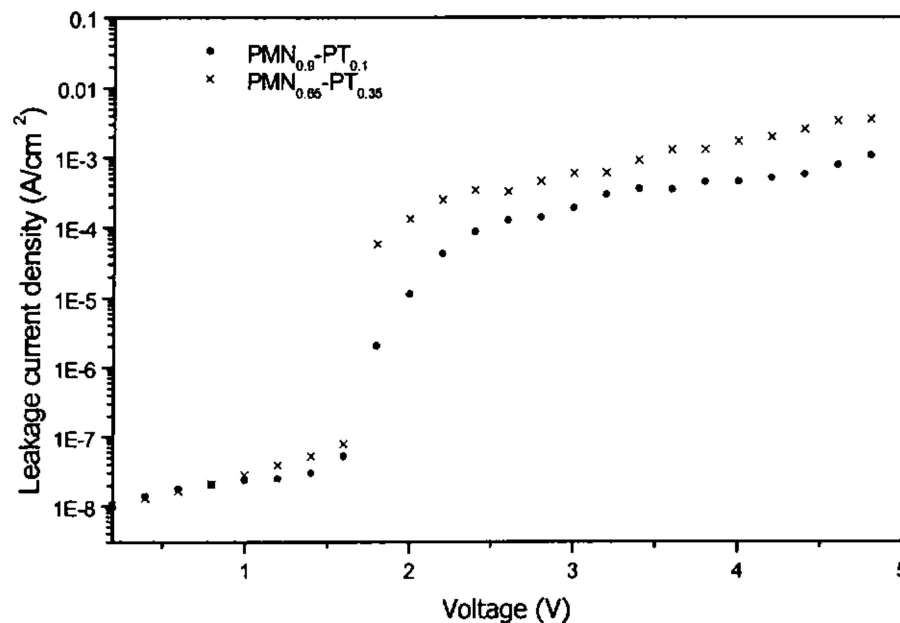

Fig. 4.5 The leakage current density versus applied voltage for the heterostructure of $PMN_{0.9}$-$PT_{0.1}$/LSMO/LAO and $PMN_{0.65}$-$PT_{0.35}$/LSMO/LAO.

	$PMN_{0.9}$-$PT_{0.1}$	$PMN_{0.65}$-$PT_{0.35}$
Leakage current density at 1V (A/cm^2)	2.3×10^{-8}	2.8×10^{-8}
Leakage current density at 5V (A/cm^2)	1.0×10^{-3}	3.6×10^{-3}

Table 4.2 The leakage current density for the heterostructure of $PMN_{0.9}$-$PT_{0.1}$/LSMO/LAO and $PMN_{0.65}$-$PT_{0.35}$/LSMO/LAO at applied voltage of 1V and 5V.

4.2.2.2 Dielectric measurement

Regarding to the dielectric constant of PMN-PT, Fig. 4.6 shows the dielectric constants of $PMN_{0.9}$-$PT_{0.1}$, and $PMN_{0.65}$-$PT_{0.35}$ films grown on LSMO/LAO. The measurements were taken under room temperature. These figures show that the dielectric constant of $PMN_{0.9}$-$PT_{0.1}$ is larger than $PMN_{0.65}$-$PT_{0.35}$, and that the $PMN_{0.9}$-$PT_{0.1}$ film has a relatively smaller dissipation factor than $PMN_{0.65}$-$PT_{0.35}$. The dielectric constants at 10kHz are 1411 and 1224 for $PMN_{0.9}$-$PT_{0.1}$ and $PMN_{0.65}$-$PT_{0.35}$, respectively. The dissipation factors are 0.034 and 0.047 for $PMN_{0.9}$-$PT_{0.1}$ and $PMN_{0.65}$-$PT_{0.35}$, respectively.

The transition temperature of $PMN_{0.9}$-$PT_{0.1}$ and $PMN_{0.65}$-$PT_{0.35}$ were reported to be 40°C and 145°C, respectively [Park et al., 1994]. It is obvious that the $PMN_{0.9}$-$PT_{0.1}$ shows a higher dielectric constant in our measurement because its transition temperature is near the room temperature. This phenomenon is the same as that occurred in PMN-PT ceramics with different PT content, where the dielectric constant has also a maximum value for $PMN_{0.9}$-$PT_{0.1}$ at room temperature [Park et al.,

1994]. It is important to note that the dielectric constants obtained here for our thin film samples are about an order of magnitude lower than PMN-PT ceramics. We believe that the small grain size and "dead layer" in the interface are the major cause. The grain size of the PMN-PT film is much smaller than ceramics. Consequently, the dielectric constant is much reduced. Besides, stress developed in the films can also contribute to the reduction of the dielectric constant.

From the above results, the overall electrical properties of $PMN_{0.9}$-$PT_{0.1}$ are better than $PMN_{0.65}$-$PT_{0.35}$ at room temperature. Therefore, $PMN_{0.9}$-$PT_{0.1}$ will be chosen for subsequent studies.

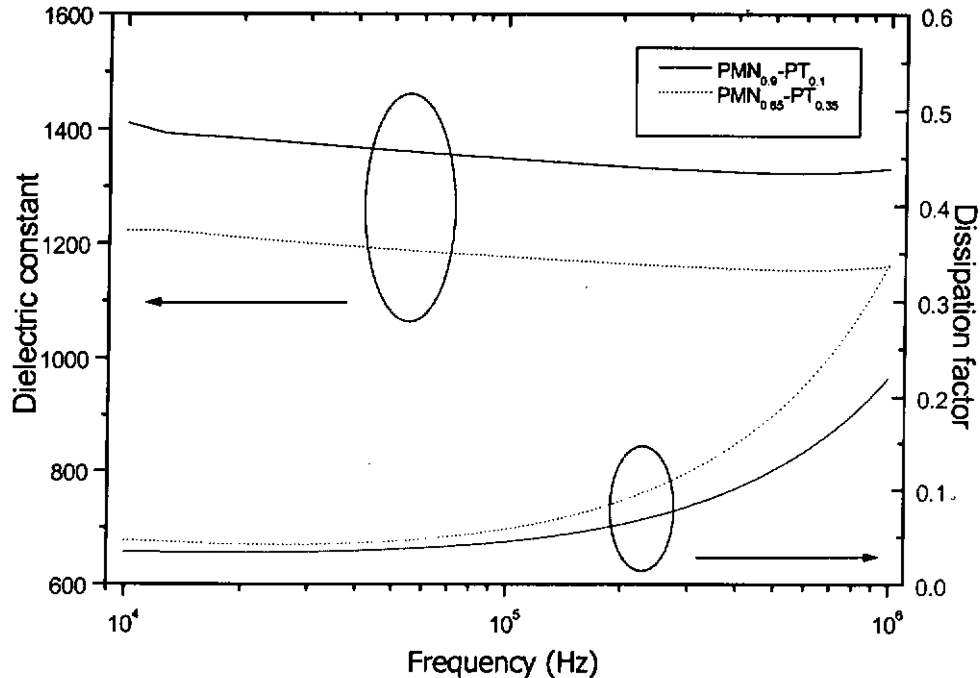

Fig. 4.6 The dielectric constant and dissipation factor of PMN-PT film for the heterostructure of $PMN_{0.9}$-$PT_{0.1}$/LSMO/LAO and $PMN_{0.65}$-$PT_{0.35}$/LSMO/LAO.

4.3 Thickness dependence of $PMN_{0.9}$-$PT_{0.1}$/LSMO/LAO

4.3.1 Fabrication and structural characterization of thin films

The fabrication condition of the LSMO and $PMN_{0.9}$-$PT_{0.1}$ layers were the same as that described in previous section. The deposition time for $PMN_{0.9}$-$PT_{0.1}$ films were 3, 5, 10, 15 and 20 minutes. In this way, different thickness $PMN_{0.9}$-$PT_{0.1}$ films were prepared according to the deposition time used and heterostructures of $PMN_{0.9}$-$PT_{0.1}$ /LSMO/LAO were fabricated with $PMN_{0.9}$-$PT_{0.1}$ film thickness ranging from 70 to 450nm.

The thickness of the $PMN_{0.9}$-$PT_{0.1}$ films were characterized by spectroellipsometry (SE) and yielded values of 70, 120, 250, 400 and 450nm. The thickness of LSMO film is 150 nm. The structure of the films was characterized by XRD. The XRD 2θ-θ profiles of the $PMN_{0.9}$-$PT_{0.1}$/LSMO/LAO films for the thickness of $PMN_{0.9}$-$PT_{0.1}$ spanning the range from 70 to 450 nm are illustrated in Fig. 4.7. From the figure, highly oriented single perovskite phase of $PMN_{0.9}$-$PT_{0.1}$ films are observed. In general, the intensity of the diffraction peak of $PMN_{0.9}$-$PT_{0.1}$(002) increases with film thickness.

The XRD ω–scan was performed to examine the out-of-plane orientation of the $PMN_{0.9}$-$PT_{0.1}$(002) diffraction peaks. The full width at half maximum (FWHM) of the rocking curves for different thickness of $PMN_{0.9}$-$PT_{0.1}$ films stand from 0.7° to 1.1°. It does not show any tendency of FWHM value with film thickness.

The XRD ϕ–scan of the $PMN_{0.9}$-$PT_{0.1}$(202), LSMO(202), and LAO(202) were performed to confirm epitaxial growth of the films and they are shown in Fig. 4.8. It indicates that the films are cube-on-cube grown on LAO(001) substrate and shows an in-plane epitaxial relationship of $(001)_{(0.9)PMN-(0.1)PT}||(001)_{LSMO}||(001)_{LAO}$ for the 450nm thick $PMN_{0.9}$-$PT_{0.1}$ film. Similar heteroepitaxial relationships are also obtained for all other thinner $PMN_{0.9}$-$PT_{0.1}$ films.

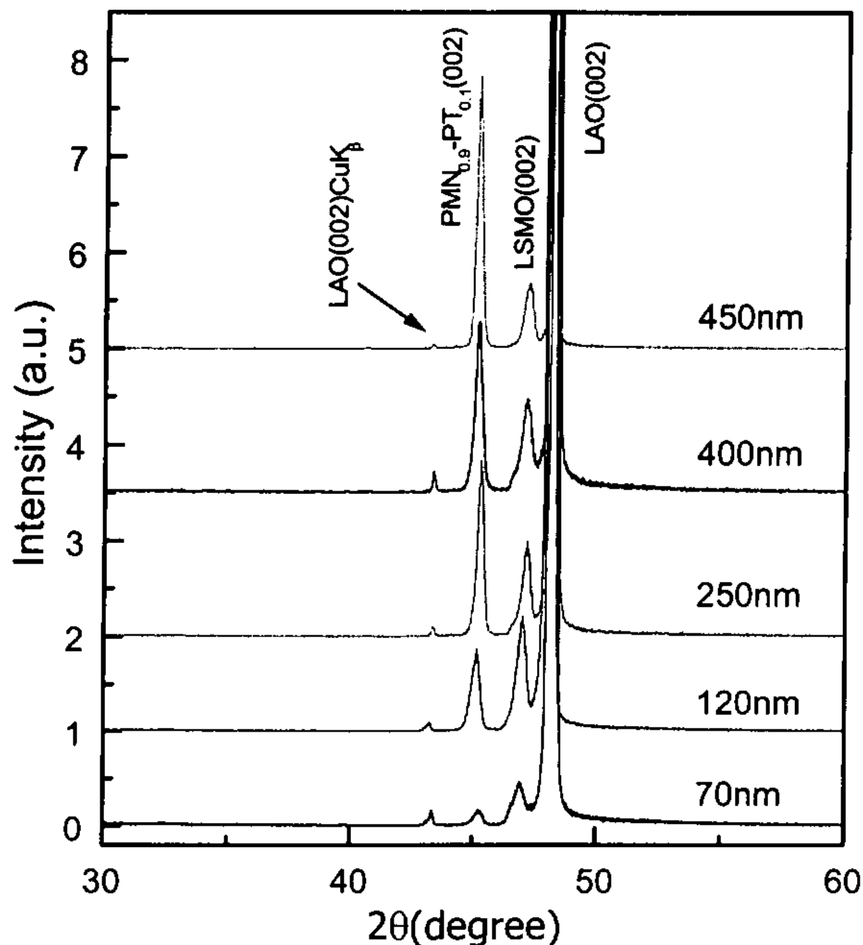

Fig. 4.7 The XRD 2θ-θ profiles of the $PMN_{0.9}$-$PT_{0.1}$/LSMO/LAO films for the thickness of $PMN_{0.9}$-$PT_{0.1}$ in the range of 70 to 450nm.

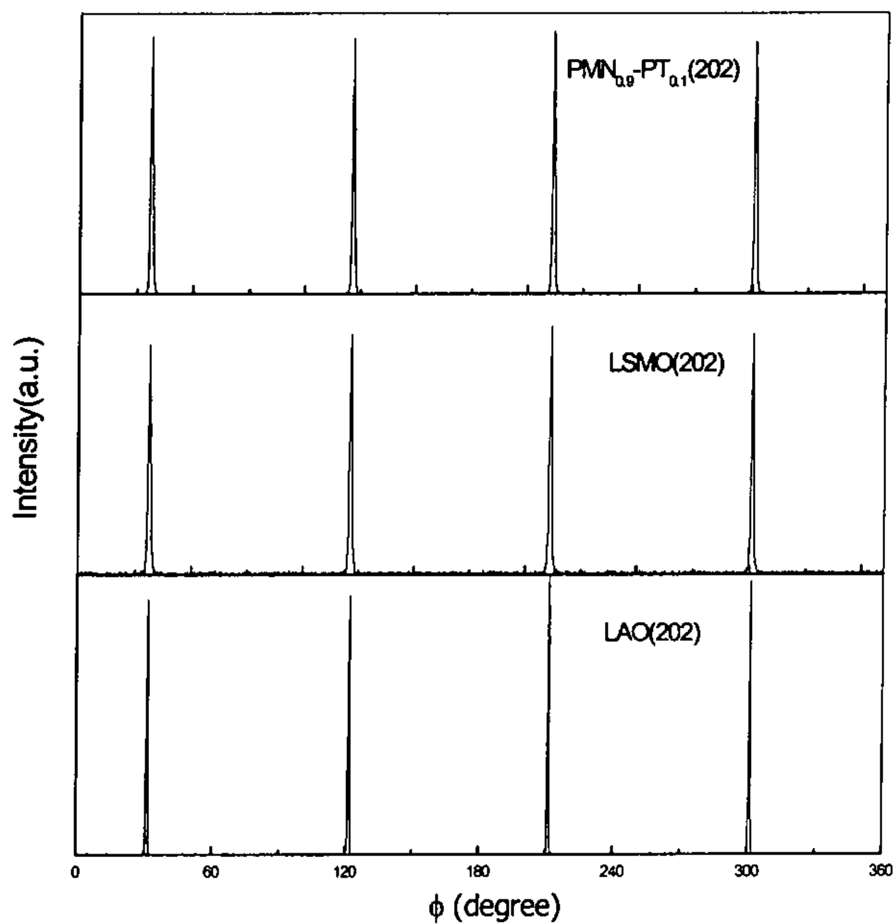

Fig. 4.8 The ϕ–scan of the $PMN_{0.9}$-$PT_{0.1}$(202), LSMO(202), and LAO(202).

4.3.2 Surface morphology

Fig. 4.9 shows the SEM image of a $PMN_{0.9}$-$PT_{0.1}$ film fabricated on LSMO/LAO with thickness of 450nm. Fig. 4.9a and 4.9b are the surface and cross-section images of $PMN_{0.9}$-$PT_{0.1}$/LSMO/LAO heterostructure, respectively. We can see that the surface of $PMN_{0.9}$-$PT_{0.1}$ film is quite smooth and crack-free. From Fig. 4.9b, the $PMN_{0.9}$-$PT_{0.1}$ and LSMO layers can be easily distinguished. The thickness of $PMN_{0.9}$-$PT_{0.1}$ and LSMO films are about 450 nm and 150 nm, respectively. Fig. 4.10a and 4.10b are the SEM image for the 400 nm thick $PMN_{0.9}$-$PT_{0.1}$ film. These thickness values are close to those obtained by SE. The 400 nm $PMN_{0.9}$-$PT_{0.1}$ film has similar feature for 450 nm $PMN_{0.9}$-$PT_{0.1}$ film. The difference is that the 400 nm $PMN_{0.9}$-$PT_{0.1}$ film has larger grain size. From Fig. 4.10a, the grain size is about 100 nm. The detailed mechanism of controlling the grain size and surface morphology is not well known at the moment. For example, Jang et al. [Jang et al., 1997] found that the grain size of $BaTiO_3$ ferroelectric films is related to the thickness. The grain size increases with film thickness. They reported thickness dependence of film properties change with grain size. The dielectric constant increased with increasing grain size. However, not all reports show the grain size depends on film thickness. Lian et al. revealed that the grain size of Lead zirconate titanate (PZT) thin film did not show any significant dependence on film thickness [Lian et al., 2000].

From the SEM images of our $PMN_{0.9}$-$PT_{0.1}$ films (not all shown in here), there is no correlation between grain size and film thickness. The grain size of the 400nm thick film is the largest among the films. It simply did not show trend of grain size dependence on film thickness.

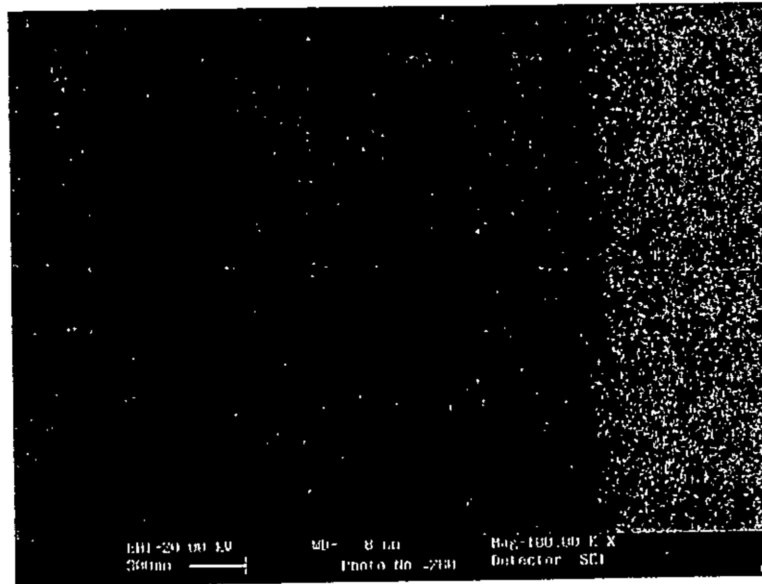

Fig. 4.9a The SEM surface image of 450nm $PMN_{0.9}$-$PT_{0.1}$ film.

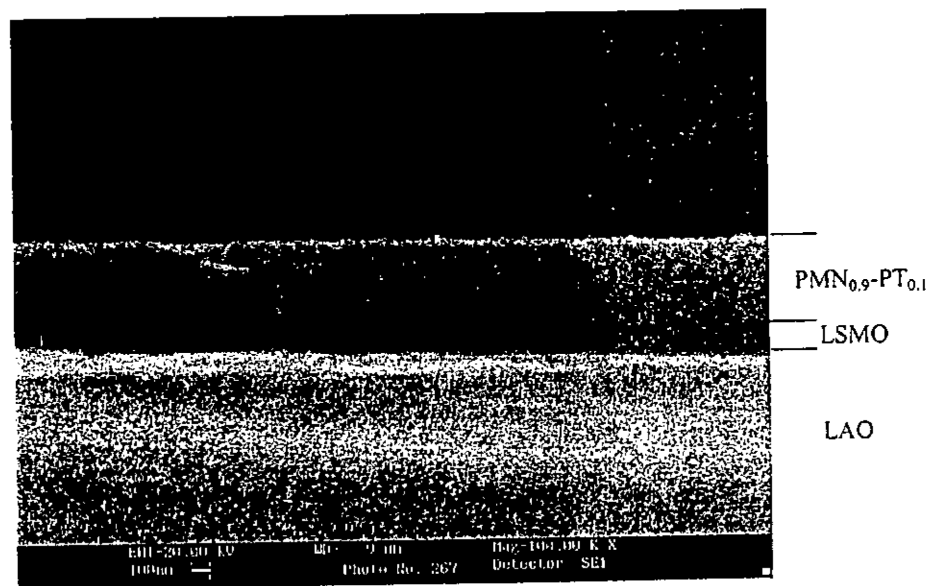

Fig. 4.9b The SEM cross-sectional image of 450nm $PMN_{0.9}$-$PT_{0.1}$ film.

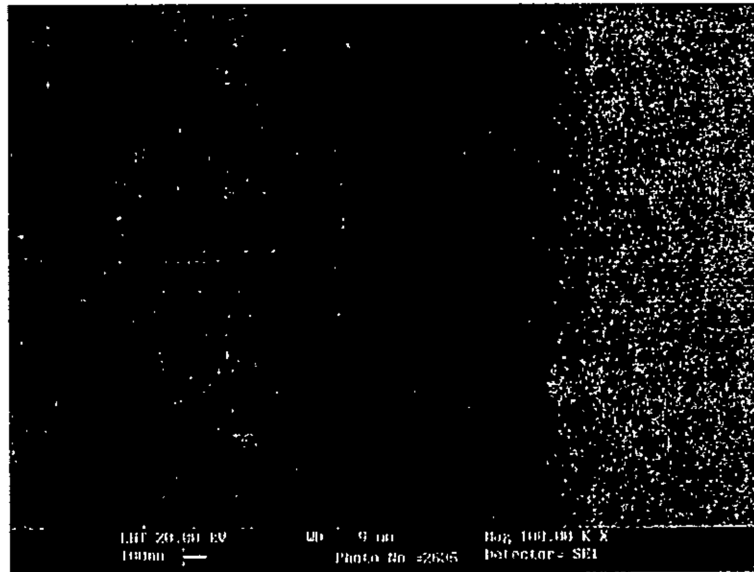

Fig. 4.10a The SEM surface image of 400nm $PMN_{0.9}$-$PT_{0.1}$ film.

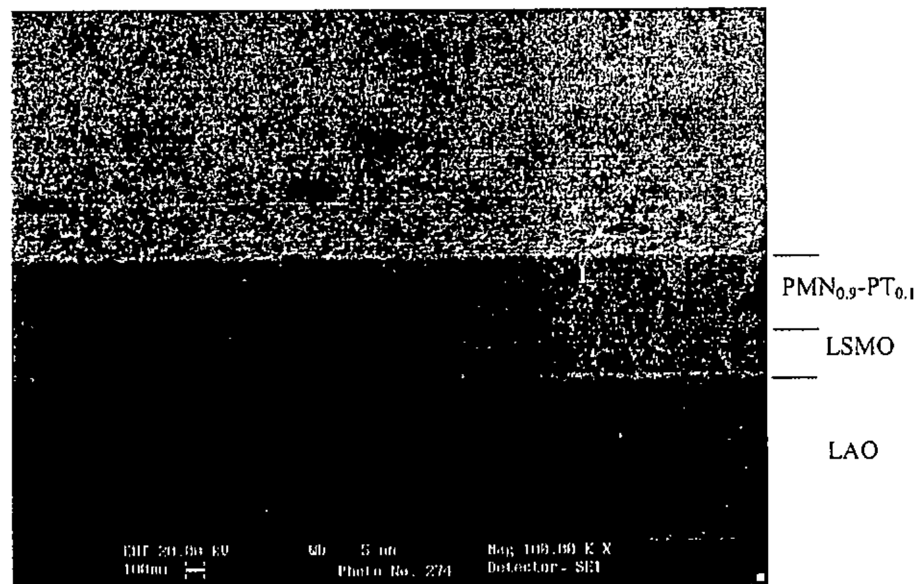

Fig. 4.10b The SEM cross-sectional image of 400nm $PMN_{0.9}$-$PT_{0.1}$ film.

Pao Yue-kong Library
PolyU • Hong Kong

4.3.3 Electrical properties

4.3.3.1 Leakage current measurement

Fig. 4.11 illustrates the leakage current density versus applied voltage for the heterostructure of $PMN_{0.9}$-$PT_{0.1}$/LSMO/LAO where the $PMN_{0.9}$-$PT_{0.1}$ layer were deposited at 650°C for different thickness. From the figure, there is large leakage current density for $PMN_{0.9}$-$PT_{0.1}$ from 70 to 250 nm, but small leakage current density for $PMN_{0.9}$-$PT_{0.1}$ films with 400 and 450nm thick. The leakage current densities at 1V are 8.54×10^{-3}, 1.52×10^{-3}, 2.70×10^{-4}, 3.87×10^{-8}, and 2.35×10^{-8} A/cm^2 for the thickness of $PMN_{0.9}$-$PT_{0.1}$ film ranging from 70 to 450nm.

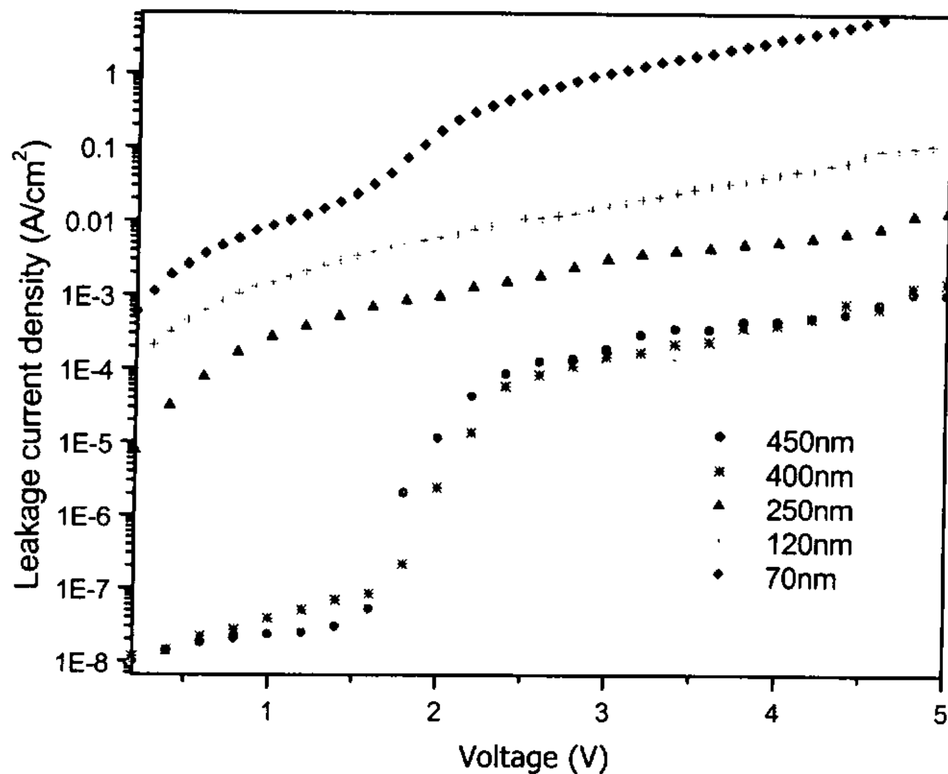

Fig. 4.11 The thickness dependence of leakage current density versus applied voltage for the heterostructure of $PMN_{0.9}$-$PT_{0.1}$/LSMO/LAO.

4.3.3.2 Dielectric measurement

For the dielectric constant of $PMN_{0.9}$-$PT_{0.1}$, Fig. 4.12 summaries the thickness dependence of dielectric constant of $PMN_{0.9}$-$PT_{0.1}$ films for the heterostructure of $PMN_{0.9}$-$PT_{0.1}$/LSMO/LAO. All measurements were performed under room temperature. These figures show that the dielectric constant increases with thickness of $PMN_{0.9}$-$PT_{0.1}$. The dissipation factor decreases for increasing $PMN_{0.9}$-$PT_{0.1}$ film thickness. The dielectric constant is just 500 at 10kHz for the 70 nm thick $PMN_{0.9}$-$PT_{0.1}$ film and increases to 1411 with thickness reaching 450 nm. The dissipation factor varies from 0.034 to 0.23 for $PMN_{0.9}$-$PT_{0.1}$ films of different thickness of the present studies.

As mentioned before, the grain size of $PMN_{0.9}$-$PT_{0.1}$ film did not show any dependence on film thickness. The decrease in dielectric constant of the $PMN_{0.9}$-$PT_{0.1}$ film with thickness is not due to grain size effect. It is probable due to the interfacial layer effect. The interaction of dielectric film with top/bottom electrode forms an interfacial layer. Normally, the dielectric constant of the interfacial layer is much smaller than the dielectric layer. The presence of these thin interfacial layers between dielectric and electrodes with a low dielectric constant can have a large effect on the net dielectric constant of the film. In addition, the interfacial layer effect is more significant for thinner films [Lee et al., 2000]. Therefore, the dielectric constant of thinner film is much lower than thicker films.

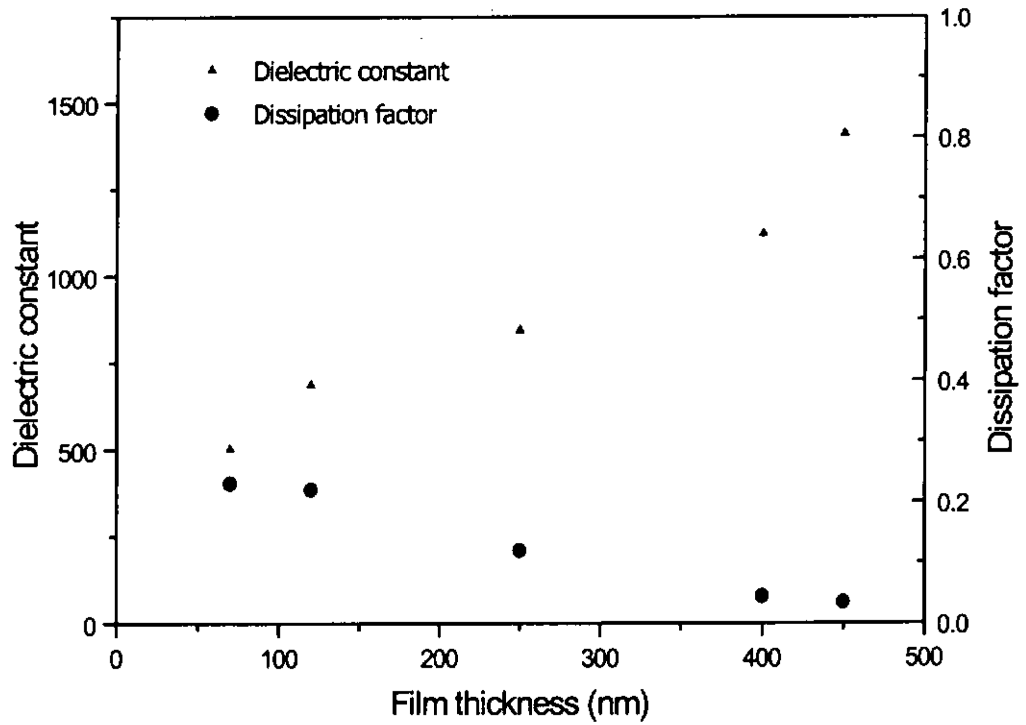

Fig. 4.12 The thickness dependence of dielectric constant and dissipation factor of $PMN_{0.9}$-$PT_{0.1}$ film for the heterostructure of $PMN_{0.9}$-$PT_{0.1}$/LSMO/LAO at 10kHz.

Chapter Five

Fabrication and Characterization of $PMN_{0.9}$-$PT_{0.1}$/LSMO/MgO/TiN/Si

5.1 Introduction

Heteroepitaxial growth of dielectric thin films on semiconductor substrates is crucial for developing practical integrated microelectronic devices. High-quality epitaxial $PMN_{0.9}$-$PT_{0.1}$ films fabricated on Si substrates are required. Since there is a large lattice mismatch and interdiffusion existing between the $PMN_{0.9}$-$PT_{0.1}$ and Si substrate, epitaxial $PMN_{0.9}$-$PT_{0.1}$ films directly grown on Si substrates cannot be obtained. To grow epitaxial $PMN_{0.9}$-$PT_{0.1}$ film on Si substrate, a buffer layer is required to act as an epitaxy template layer as well as a diffusion barrier. TiN is a commonly used buffer layer or diffusion barrier. It can also be epitaxially grow on Si substrate. It is, however, proved to oxidize at above 300°C under ambient oxygen. To prevent oxidation of TiN, we use a combination of MgO/TiN buffer layers. They have been epitaxially grown on Si(001) substrate and proved to be an excellent buffer for perovskites [Wu et al., 2000]. In the present work we have demonstrated the heteroepitaxial growth of $PMN_{0.9}$-$PT_{0.1}$/LSMO/MgO/TiN/Si. The electrical properties of the $PMN_{0.9}$-$PT_{0.1}$ films of this heterostructure have also been studied.

Before growing the $PMN_{0.9}$-$PT_{0.1}$ films on Si substrates, $PMN_{0.9}$-$PT_{0.1}$ films are first deposited on MgO single crystal substrates with LSMO bottom electrodes in order to confirm the epitaxial growth conditions of $PMN_{0.9}$-$PT_{0.1}$/LSMO/MgO. Then the heterostructure of LSMO/MgO/TiN/Si film have been fabricated and the structural properties are characterized by XRD and SEM. Up till now, there is only one report on epitaxial PMN thin film deposited on Si substrate with the heterostructure of PMN/$La_{0.5}Sr_{0.5}CoO_3$ (LSCO)/CeO_2/YSZ/Si [Wakiya et al., 2001]. But the deposition temperature of the buffer layer is quite high (800°C) and it is undesirable for fabricating integrated devices. In this chapter, we describe our research to grow epitaxial $PMN_{0.9}$-$PT_{0.1}$ film on Si substrates at a relatively lower temperature (≤ 650°C) for potential integrated device development.

5.2 Fabrication and characterization of $PMN_{0.9}$-$PT_{0.1}$ /LSMO/MgO

5.2.1 Fabrication and structural characterization of thin films

The heterostructure of $PMN_{0.9}$-$PT_{0.1}$/LSMO/MgO was fabricated by PLD method. For the fabrication of bottom LSMO electrode, the deposition temperature and the ambient oxygen pressure were kept at 650°C and 150 mTorr, respectively. For the fabrication of $PMN_{0.9}$-$PT_{0.1}$, the film was deposited under 200 mTorr ambient oxygen pressure and the deposition temperature was between 600°C and 650°C.

The structures of the films were characterized by XRD and SEM. The XRD 2θ-θ profiles of the $PMN_{0.9}$-$PT_{0.1}$/LSMO/MgO films for the deposition temperature of $PMN_{0.9}$-$PT_{0.1}$ in the range of 600°C to 650°C are showed in Fig. 5.1. From these figures, highly oriented and single perovskite phase of $PMN_{0.9}$-$PT_{0.1}$ films are observed. Tantigate et al. [Tantigate et al., 1995] also prepared a single phase $PMN_{0.9}$-$PT_{0.1}$ film on LSCO/MgO(001) substrate by PLD. However, they revealed that single phase perovkite $PMN_{0.9}$-$PT_{0.1}$ is only obtained at the deposition temperature of 575°C, and pyrochlore phase exist below 550°C and above 600°C. Wang et al. [Wang et al., 2001] reported that the formation of the perovskite phase in the films depends on the target composition. It was found that an Mg-rich target produce perovskite phase in a wide deposition temperature range. Since our $PMN_{0.9}$-$PT_{0.1}$ target is Mg-rich and Pb-rich, single perovskite phase $PMN_{0.9}$-$PT_{0.1}$ thin film can be thus obtained in a wide temperature range.

The out-of-plane orientation of the $PMN_{0.9}$-$PT_{0.1}$(002) peaks was examined by ω–scan. The FWHM of the rocking curve for 600°C, 625°C, and 650°C are 1.12°, 0.90°, and 0.83°, respectively. The orientation of $PMN_{0.9}$-$PT_{0.1}$ film is improved by increasing the deposition temperature. These figures reveal that the film deposited at 650°C has the best orientation because the smallest value of FWHM.

The XRD 360° ϕ–scan of the $PMN_{0.9}$-$PT_{0.1}$(202), LSMO(202), and MgO(202) were performed to confirm epitaxial growth of the films. Fig. 5.2 illustrates the ϕ–scan of $PMN_{0.9}$-$PT_{0.1}$/LSMO/MgO for $PMN_{0.9}$-$PT_{0.1}$ deposited at

650°C. The four-fold symmetric (separated by 90°) diffraction peaks of a typical cubic structure of different layers are found to locate at the same angular position. This indicates that the films are cube-on-cube grown on MgO(001) substrate. It suggests an in-plane epitaxial relationship of $(001)_{(0.9)PMN-(0.1)PT}||(001)_{LSMO}||(001)_{MgO}$. Similar heteroepitaxial relationships are also obtained for $PMN_{0.9}$-$PT_{0.1}$ deposited at 600°C to 625°C but with inferior crystallinity.

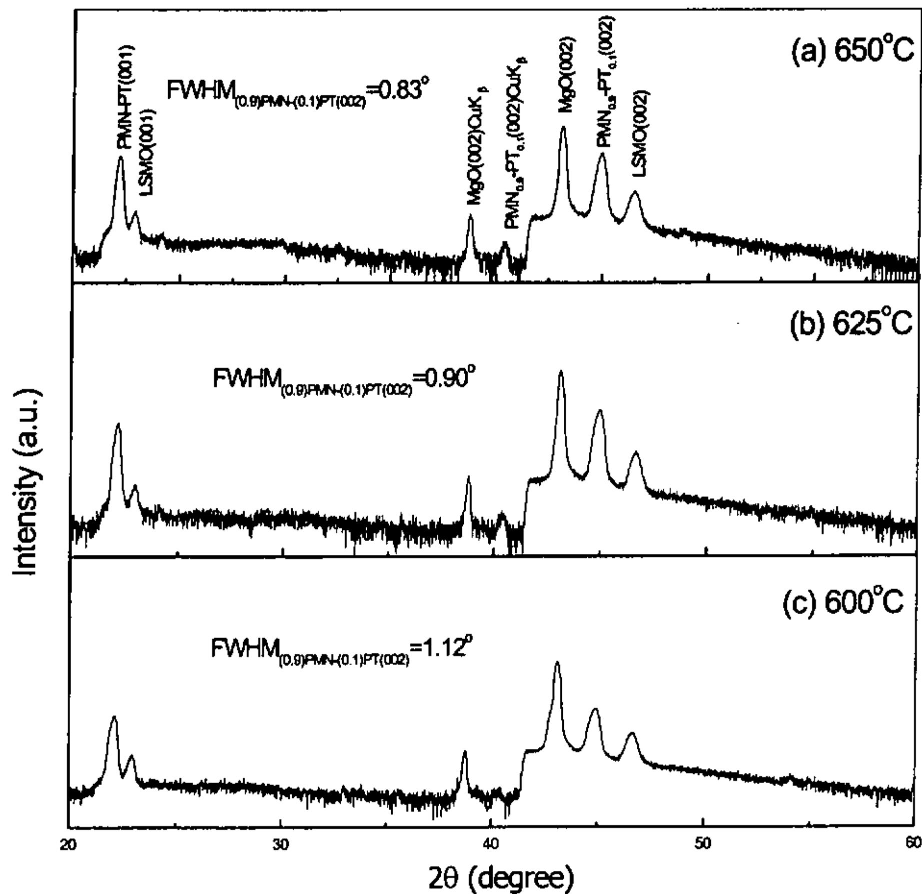

Fig. 5.1 The XRD 2θ-θ profiles of the $PMN_{0.9}$-$PT_{0.1}$/LSMO/MgO film for the deposition temperature of $PMN_{0.9}$-$PT_{0.1}$ in the range of 600°C to 650°C.

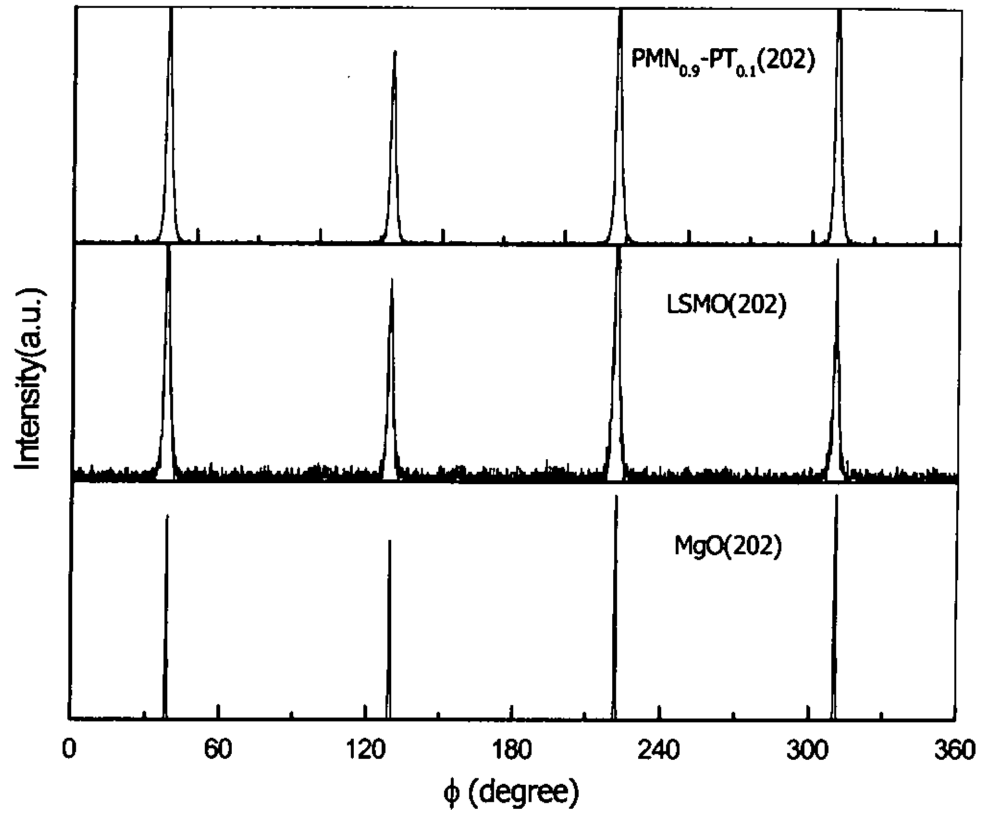

Fig. 5.2 The XRD ϕ–scan of the $PMN_{0.9}$-$PT_{0.1}$(202), LSMO(202), and MgO(202) for $PMN_{0.9}$-$PT_{0.1}$ deposited at 650°C.

5.2.2 Surface morphology

Fig. 5.3 shows the surface and cross-sectional SEM image of the $PMN_{0.9}$-$PT_{0.1}$ film fabricated on LSMO/MgO at 650°C. From the figure, the surface of the $PMN_{0.9}$-$PT_{0.1}$ film is quite smooth but with some dense outgrowth. The SEM cross-sectional image shows columnar structure and with clear boundary between dielectric and oxide electrode films. The thickness of $PMN_{0.9}$-$PT_{0.1}$ film is about 450 nm.

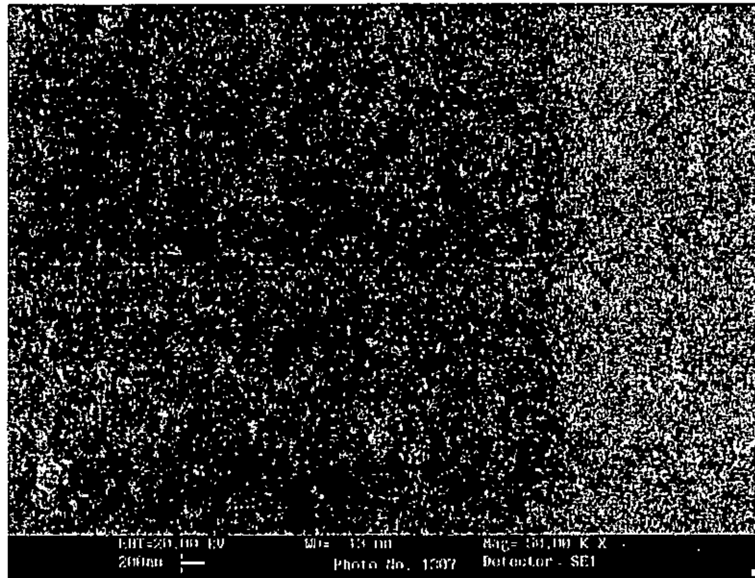

Fig. 5.3a The SEM surface image of $PMN_{0.9}$-$PT_{0.1}$/LSMO/MgO film.

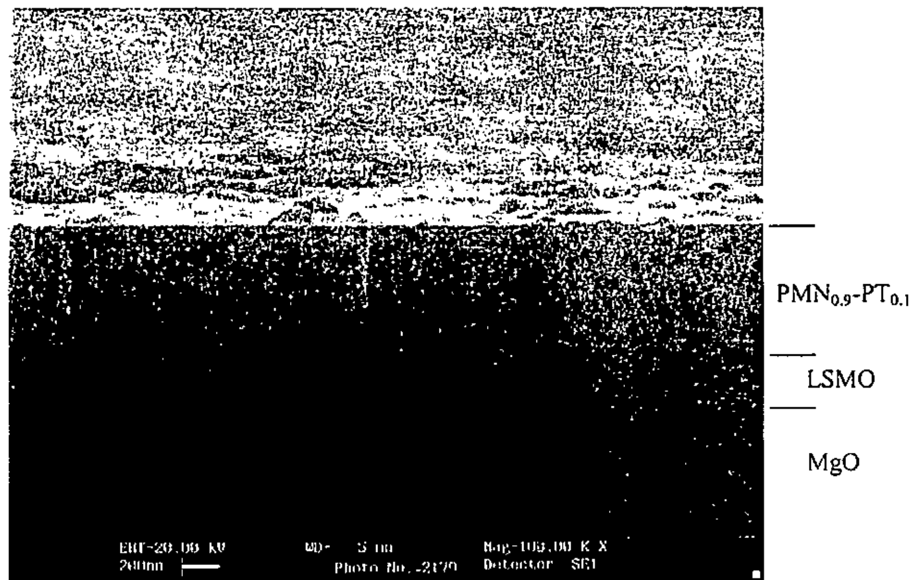

Fig. 5.3b The SEM cross-sectional image of $PMN_{0.9}$-$PT_{0.1}$/LSMO/MgO film.

5.2.3 Electrical properties

Table 5.1 summarizes the leakage current density at 1V and the dielectric constant at 10 kHz for the heterostructure of $PMN_{0.9}$-$PT_{0.1}$/LSMO/MgO where the $PMN_{0.9}$-$PT_{0.1}$ layers were deposited at 600°C, 625°C and 650°C. The leakage current density of $PMN_{0.9}$-$PT_{0.1}$ films are 1.01 x 10^{-7}, 8.69 x 10^{-9} and 8.57 x 10^{-9} A/cm^2 at 1V for $PMN_{0.9}$-$PT_{0.1}$ films deposited at 600°C, 625°C and 650°C, respectively. There is large leakage current density for $PMN_{0.9}$-$PT_{0.1}$ deposited at 600°C. Those for $PMN_{0.9}$-$PT_{0.1}$ deposited at 625°C and 650°C are reasonably small. The difference may due to better crystalline of the $PMN_{0.9}$-$PT_{0.1}$ grown at higher temperatures.

The dielectric constant for the heterostructure of $PMN_{0.9}$-$PT_{0.1}$/LSMO/MgO are 1186, 1300, and 1435 at 10 kHz for $PMN_{0.9}$-$PT_{0.1}$ films deposited at 600°C, 625°C and 650°C, respectively. These figures show that the dielectric constant of $PMN_{0.9}$-$PT_{0.1}$ increases with deposition temperature. Again, it is probably due to better crystallinity of the $PMN_{0.9}$-$PT_{0.1}$ deposited at higher temperatures. Besides, higher deposition temperature can also reduce interfacial layer effect. Lee et al. [Lee et al., 2000] have demonstrated that at higher deposition temperature, BST film resulted in a larger dielectric constant due to a smaller interfacial-dead layer effect in addition to better crystalline quality by which a larger net dielectric constant was obtained. The dissipation factor decreases with increasing deposition temperature of $PMN_{0.9}$-$PT_{0.1}$. This apparently is the result of bad crystallinity of the film, especially for those $PMN_{0.9}$-$PT_{0.1}$ films deposited at low temperature.

In general, the higher the deposition temperature of $PMN_{0.9}$-$PT_{0.1}$, the better is crystallinity of the $PMN_{0.9}$-$PT_{0.1}$ film. Consequently it results in better electrical properties of $PMN_{0.9}$-$PT_{0.1}$ film. However, one should bear in mind that too high deposition temperature may cause detrimental Pb and Mg loss, which may lead to degradation of the $PMN_{0.9}$-$PT_{0.1}$ properties.

Deposition temperature	Dielectric constant at 10 kHz	Dissipation factor at 10 kHz	Leakage Current Density (A/cm^2)
600°C	1186	0.20	1.01×10^{-7}
625°C	1300	0.071	8.69×10^{-9}
650°C	1435	0.056	8.57×10^{-9}

Table 5.1 Electrical properties of $PMN_{0.9}$-$PT_{0.1}$ grown on LSMO/MgO with deposition temperature of 600°C, 625°C, and 650°C.

5.3 LSMO/MgO/TiN/Si

5.3.1 Fabrication and structural characterization of thin films

For microelectronic applications, it is important to grow the $PMN_{0.9}$-$PT_{0.1}$ on Si. Before the fabrication of $PMN_{0.9}$-$PT_{0.1}$ film, the heterostructure structure of LSMO/MgO/TiN/Si film was prepared and characterized first. For the fabrication of TiN and MgO, the pressure of the chamber was pumped down to 5×10^{-6} Torr. The substrate temperature was fixed at 650°C. For the fabrication of LSMO, the film was deposited under 150 mTorr ambient oxygen pressure and the deposition temperature was 650°C.

The XRD 2θ–θ profile of LSMO/MgO/TiN/Si films is shown in Fig. 5.4. Since the lattice constants of TiN & MgO are too close, 4.22Å and 4.21Å, respectively, the two X-ray diffraction peaks cannot be resolved. Highly oriented single phase films are obtained. The FWHM of the rocking curve of LSMO(002) and MgO & TiN(002) films are 1.53° and 1.59°, respectively. The XRD ϕ-scan of the LSMO(202), MgO & TiN(202), and Si(202) were performed and they are shown in Fig. 5.5. All diffraction peaks are at the same position where the peaks are separated by 90°. This implies that the films are cube-on-cube growth on the Si(001) substrate with an in-plane epitaxial relationship of $(001)_{LSMO}||(001)_{MgO}||(001)_{TiN}||(001)_{Si}$.

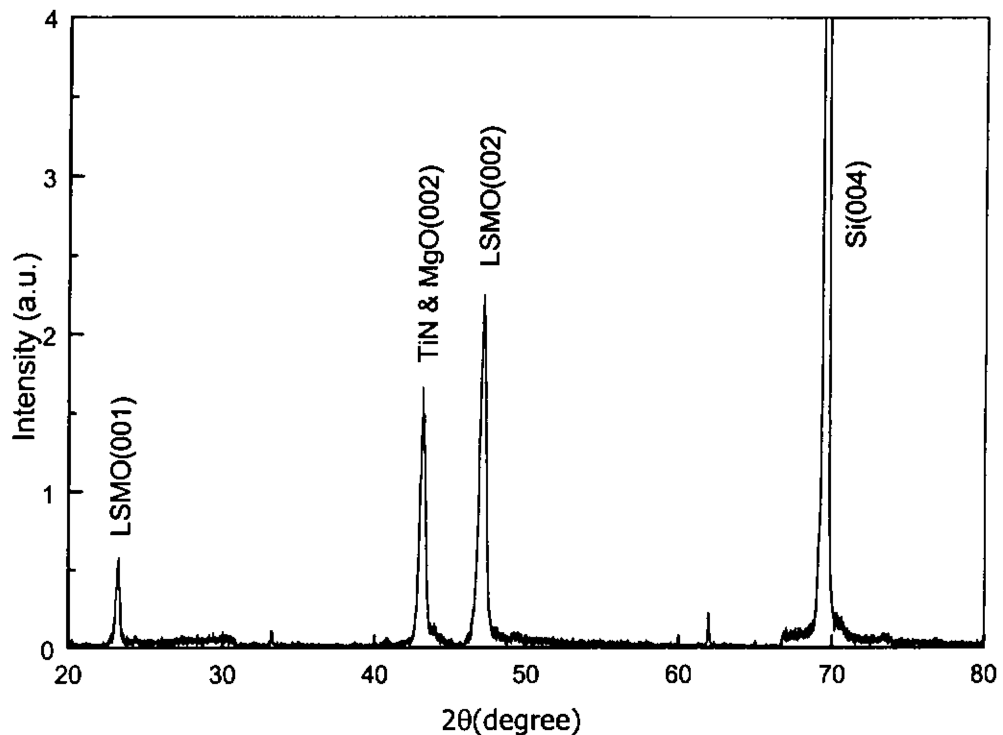

Fig. 5.5 The XRD 2θ-θ profile of the LSMO/MgO/TiN/Si films.

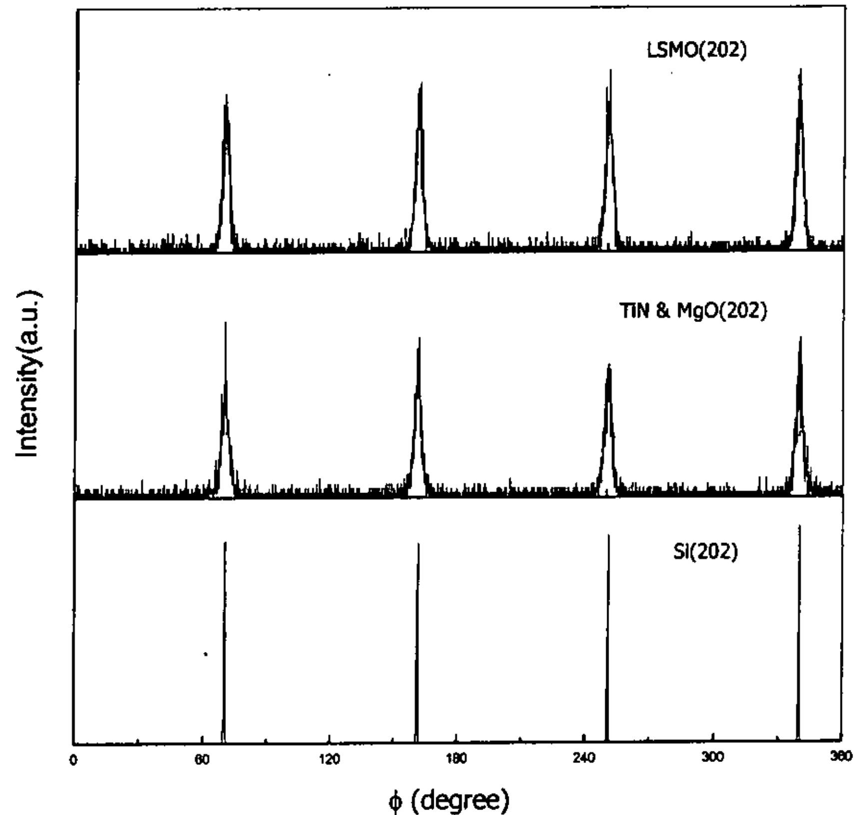

Fig. 5.6 The φ–scan of the LSMO(202), TiN & MgO(202), and Si(202).

5.3.2 Surface morphology

Fig. 5.7 shows the surface and cross-sectional SEM image of LSMO/MgO/TiN/Si film. The surface SEM image reveals that the grain size of LSMO film is quite small and uniform at about 20 to 30 nm. The cross-sectional SEM image in Fig. 5.7b shows clearly three distinct layers. The columnar structure of LSMO film can be clearly observed.

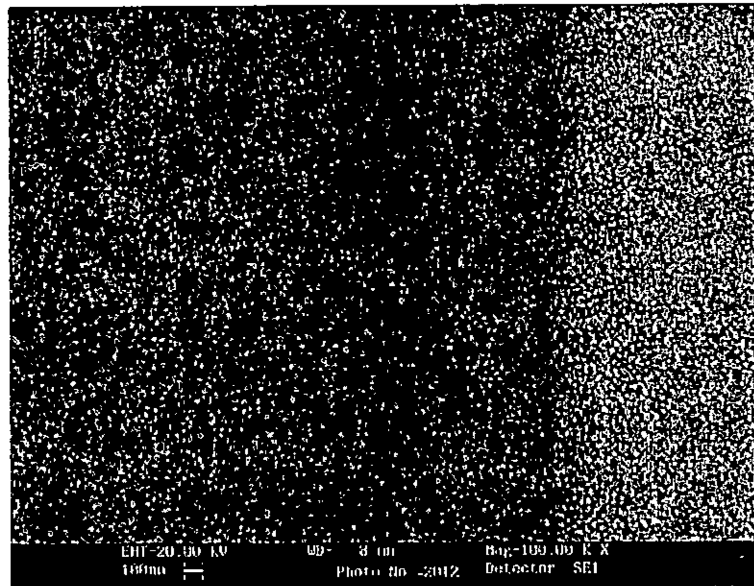

Fig. 5.7a The SEM surface image of LSMO/MgO/TiN/Si.

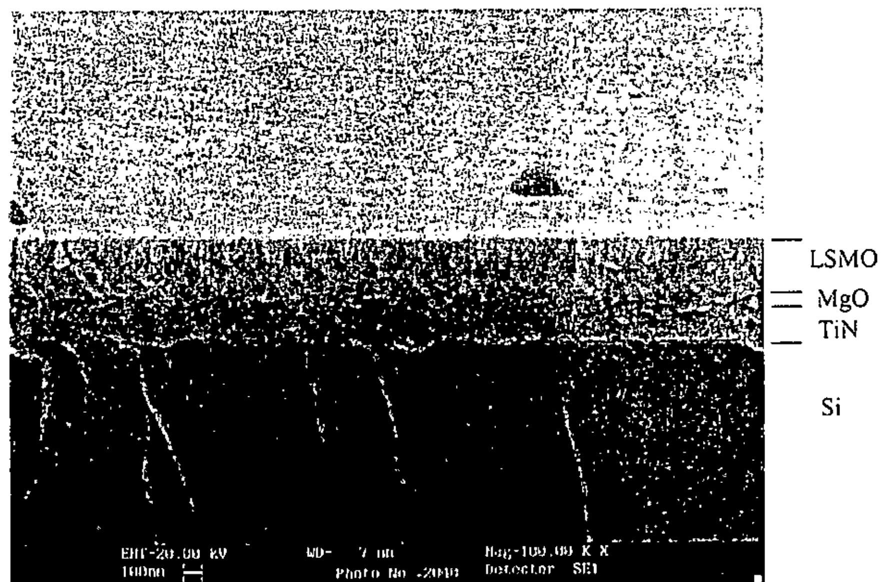

Fig. 5.7b The SEM cross-sectional image of LSMO/MgO/TiN/Si.

5.4 $PMN_{0.9}$-$PT_{0.1}$/LSMO/MgO/TiN/Si

5.4.1 Fabrication and structural characterization of thin films

The heterostructure of $PMN_{0.9}$-$PT_{0.1}$/LSMO/MgO/TiN/Si was fabricated in subsequent experiments. The deposition conditions of TiN, MgO and LSMO were the same as those described in section 5.3. For the fabrication of $PMN_{0.9}$-$PT_{0.1}$ film, it was deposited under 200 mTorr ambient oxygen pressure and at a deposition temperature of 650°C. After the deposition of the four layers, the film was cooled to room temperature naturally in the same atmosphere of deposition condition.

The XRD 2θ–θ profiles of the $PMN_{0.9}$-$PT_{0.1}$/LSMO/MgO/TiN/Si films are shown in Fig. 5.8. From the figure, no pyrochlore phase is observed and highly oriented single perovskite phase of $PMN_{0.9}$-$PT_{0.1}$ film is obtained. The out-of-plane orientation of the $PMN_{0.9}$-$PT_{0.1}$(002) peaks were examined by ω–scan. The FWHM of the rocking curve can be as small as 1.25°.

The XRD ϕ-scan of the $PMN_{0.9}$-$PT_{0.1}$(202), LSMO(202), MgO and TiN(202) , and Si(202) were performed to confirm epitaxial growth of the films. The results are shown in Fig. 5.9. From the figure, four-fold symmetry diffraction peaks of different layers are at the same angular position. This indicates that the films are cube-on-cube growth on Si(001) substrate with an in-plane epitaxial relationship of $(001)_{(0.9)PMN\text{-}(0.1)PT}||(001)_{LSMO}||(001)_{MgO}||(001)_{TiN}||(001)_{Si}$.

Wakiya et al. have demonstrated epitaxial PMN thin film deposited on Si substrate with the heterostructure of PMN/LSCO/CeO_2/YSZ/Si [Wakiya et al., 2001]. But the deposition temperature of the buffer layer is quite high (800°C) and it is undesirable for fabricating integrated devices. The high substrate temperature will cause thermal damage on Si wafer. In this study, epitaxial $PMN_{0.9}$-$PT_{0.1}$ films grown on Si substrate are demonstrated for the first time. Furthermore, the film growth temperature is shown to be as low as 650°C.

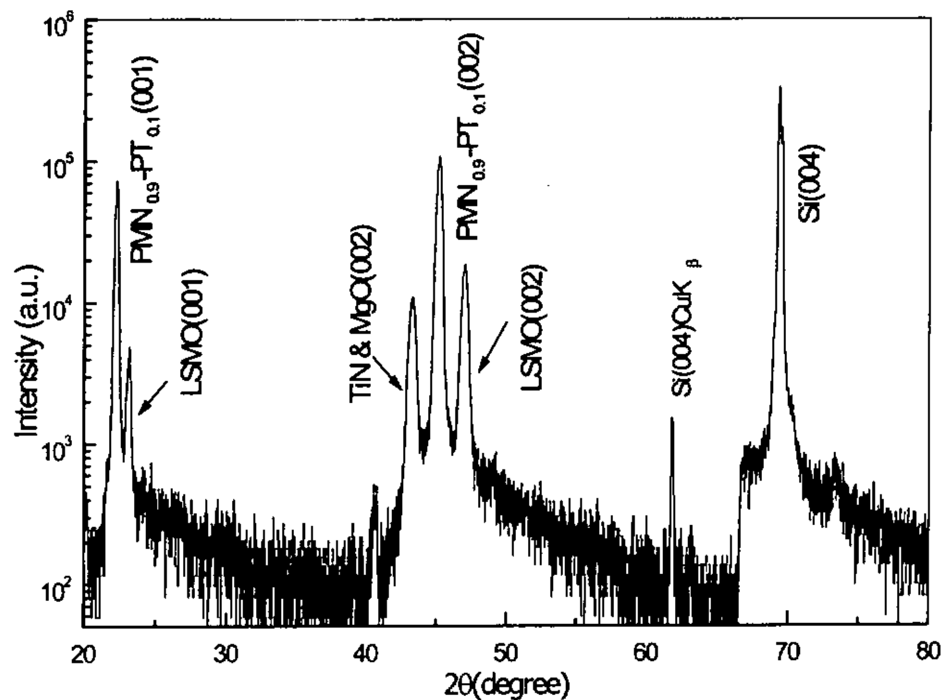

Fig. 5.8 The XRD 2θ–θ profile of the $PMN_{0.9}$-$PT_{0.1}$/LSMO/MgO/TiN/Si film.

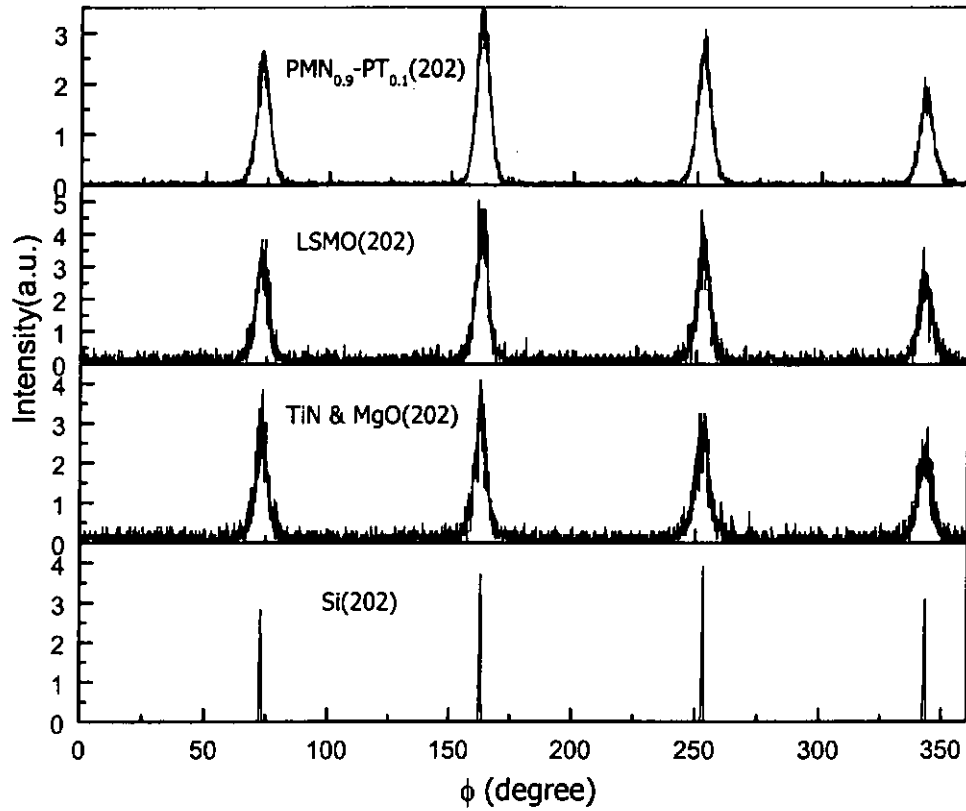

Fig. 5.9 The XRD ϕ-scan of the $PMN_{0.9}$-$PT_{0.1}$(202), LSMO(202), MgO & TiN(202), and Si(202).

5.4.2 Surface morphology

Fig. 5.10a is the image of the surface and Fig. 5.10b is the cross section of the heterostructure $PMN_{0.9}$-$PT_{0.1}$/LSMO/MgO/TiN/Si(001). From Fig. 5.10a, we can see that the surface of $PMN_{0.9}$-$PT_{0.1}$ film is quite smooth. The grain size is about 100 to 200 nm. From Fig. 5.10b, the four layers stack can be easily distinguished. The thickness $PMN_{0.9}$-$PT_{0.1}$ film is about 450 nm.

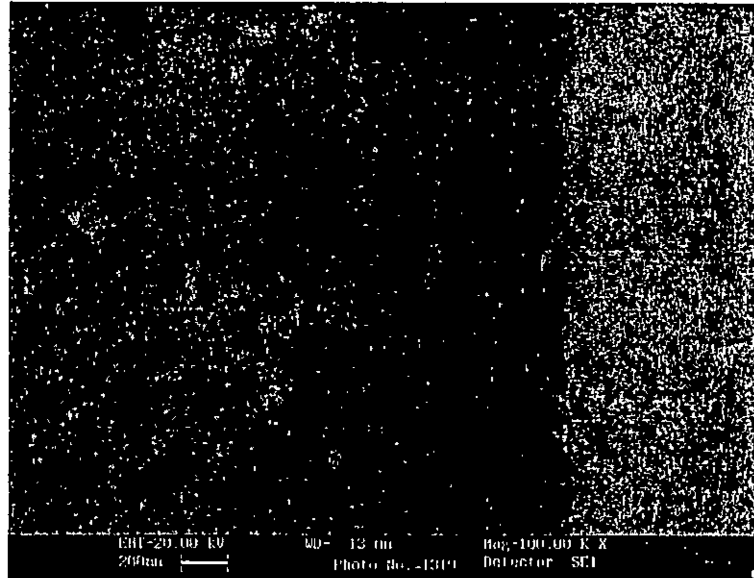

Fig. 5.10a The SEM surface image of the $PMN_{0.9}$-$PT_{0.1}$/LSMO/MgO/TiN/Si film.

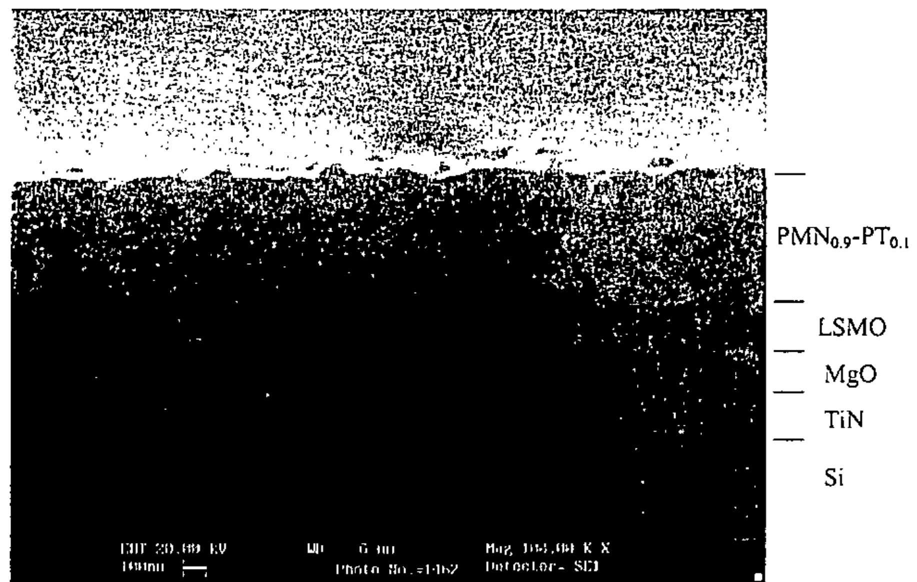

Fig. 5.10b The SEM cross-sectional image of $PMN_{0.9}$-$PT_{0.1}$/LSMO/MgO/TiN/Si film.

5.4.3 Electrical properties

5.4.3.1 Leakage current measurement

The leakage current density versus applied voltage for the heterostructure of $PMN_{0.9}$-$PT_{0.1}$/LSMO/MgO/TiN/Si film is illustrated in Fig. 5.11. The leakage current density of $PMN_{0.9}$-$PT_{0.1}$ film at 1V is 4.3×10^{-4} A/cm^2. This value is much larger than $PMN_{0.9}$-$PT_{0.1}$ films grown on LAO and MgO substrates. The large leakage current density is probably due to bad crystallinity of $PMN_{0.9}$-$PT_{0.1}$ film. Another possible cause of this large leakage may due to the large particulate (~1 μm) on the film by PLD process. These particulates are particularly prominent in the TiN film. As a result of their presence some local thinning and/or electrically short circuiting the $PMN_{0.9}$-$PT_{0.1}$ dielectric may occur.

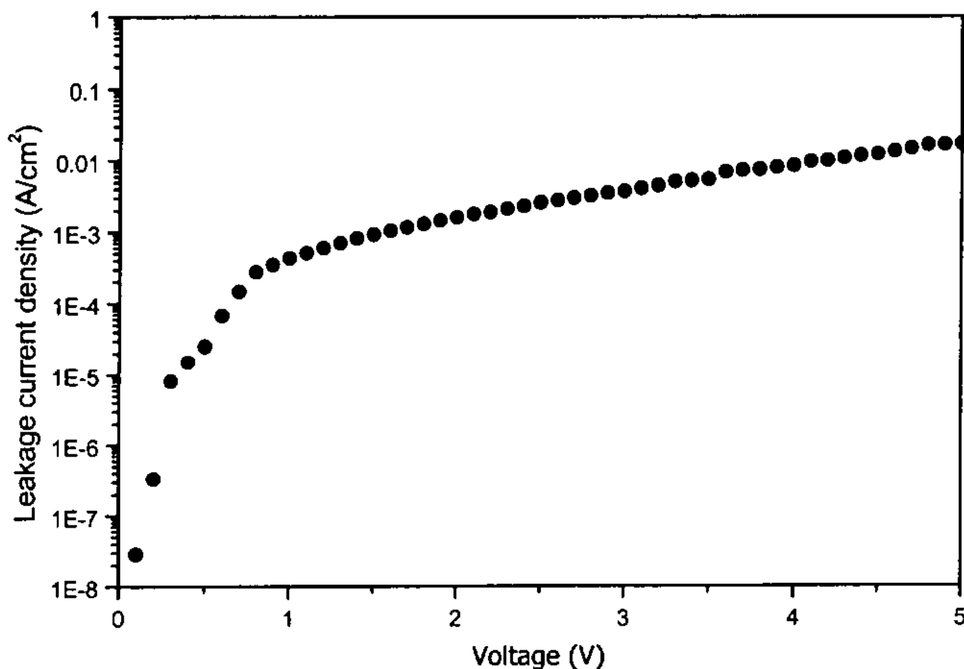

Fig. 5.11 The leakage current density versus applied voltage for the heterostructure of $PMN_{0.9}$-$PT_{0.1}$/LSMO/MgO/TiN/Si film.

5.4.3.2 Dielectric measurement

Fig. 5.12 shows the dielectric constant of $PMN_{0.9}$-$PT_{0.1}$/LSMO/MgO/TiN/Si film. The dielectric constant and the dissipation factor at 10 kHz are 1414 and 0.15, respectively. Although the dielectric constant is comparable to $PMN_{0.9}$-$PT_{0.1}$/LSMO/MgO film but it has large dissipation factor. The dielectric constant decreases dramatically with increasing frequency. The dissipation factor is quite large compared with that of $PMN_{0.9}$-$PT_{0.1}$ films grown on LAO and MgO substrates. The inferior electric properties of these $PMN_{0.9}$-$PT_{0.1}$ films may be due to the degraded crystallinity of the $PMN_{0.9}$-$PT_{0.1}$ films and large particulates on the film surface by PLD process.

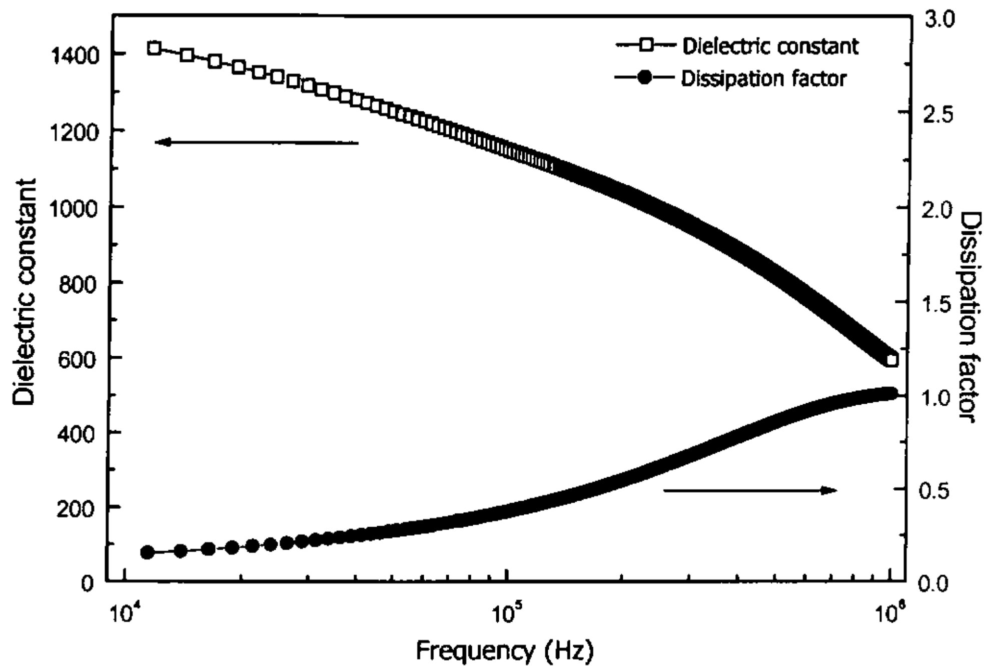

Fig. 5.12 The dielectric constant and dissipation factor for the heterostructure of $PMN_{0.9}$-$PT_{0.1}$/LSMO/MgO/TiN/Si film.

Chapter Six

Fabrication and Characterization of $PMN_{0.9}$-$PT_{0.1}$ Films with $BaPbO_3$ Electrode

6.1 Introduction

The electrical properties and reliability for a capacitor material are strongly affected by the electrode material. Electrode materials can be divided into three general groups. The first group consists of noble metals such as Pt, Au, Ir and Ru. The second group consists of rutile-type metal oxides such as IrO_2 and RuO_2. The third group is the perovskite conductive oxide such as $LaNiO_3$ (LNO), (La, Sr)CoO_3 (LSCO), and $SrRuO_3$ (SRO) that have the same structural chemistry as the dielectric perovskites [Nagaraj et. al., 2001].

$BaPbO_3$ (BPO) is a perovskite conductive oxide. The resistivity of bulk BPO ceramics has been reported to be 800 $\mu\Omega$cm at room temperature [Nitta et. al., 1965]. The structure of BPO is orthorhombic with a pseudo-cubic lattice constant of 4.267Å [Kodenkandath, 2000]. It has been demonstrated that the dielectric films deposited on the BPO/Pt electrode exhibit leakage current one order of magnitude lower than that of the films deposited on Pt electrodes [Luo et al, 2001]. Leakage current is one of the main concerns for DRAM applications. It is most desirable to grow capacitors having small leakage current and large capacitance.

As mentioned in Chapter 4, the interfacial layer effect is significant in thin film dielectric materials. Pb-based dielectrics and a Pb-based perovskite conductive oxide are expected to form a better interface. Inter-diffusion of Pb can be minimized. This can reduce the interfacial layer effect and hence increase the net dielectric constant of $PMN_{0.9}$-$PT_{0.1}$ films. Therefore, BPO should be an excellent oxide electrode for $PMN_{0.9}$-$PT_{0.1}$ film.

In this chapter, $PMN_{0.9}$-$PT_{0.1}$ films grow on LAO and MgO single crystal substrates with BPO as bottom electrode are presented. Furthermore, $PMN_{0.9}$-$PT_{0.1}$ films fabricated on Pt coated Si substrates are examined. According to Tantigate et al., an oxide layer on Pt coated Si substrate can promote the formation of $PMN_{0.9}$-$PT_{0.1}$ perovskite phase [Tantigate et al., 1996]. In this respect we have also grown perovskite $PMN_{0.9}$-$PT_{0.1}$ films on BPO and LSMO oxide electrodes, which have been deposited on top of Pt coated Si substrates. The properties of all $PMN_{0.9}$-$PT_{0.1}$ films fabricated on three different electrodes are studied and compared.

6.2 $PMN_{0.9}$-$PT_{0.1}$ on LAO with BPO bottom electrodes

6.2.1 Fabrication and structural characterization of thin films

Ceramic BPO target was prepared by solid-state reaction of $BaCO_3$ and PbO powder. Its X-ray diffraction profile is shown in Fig. 6.1 that confirms the presence of single perovskite structure of BPO.

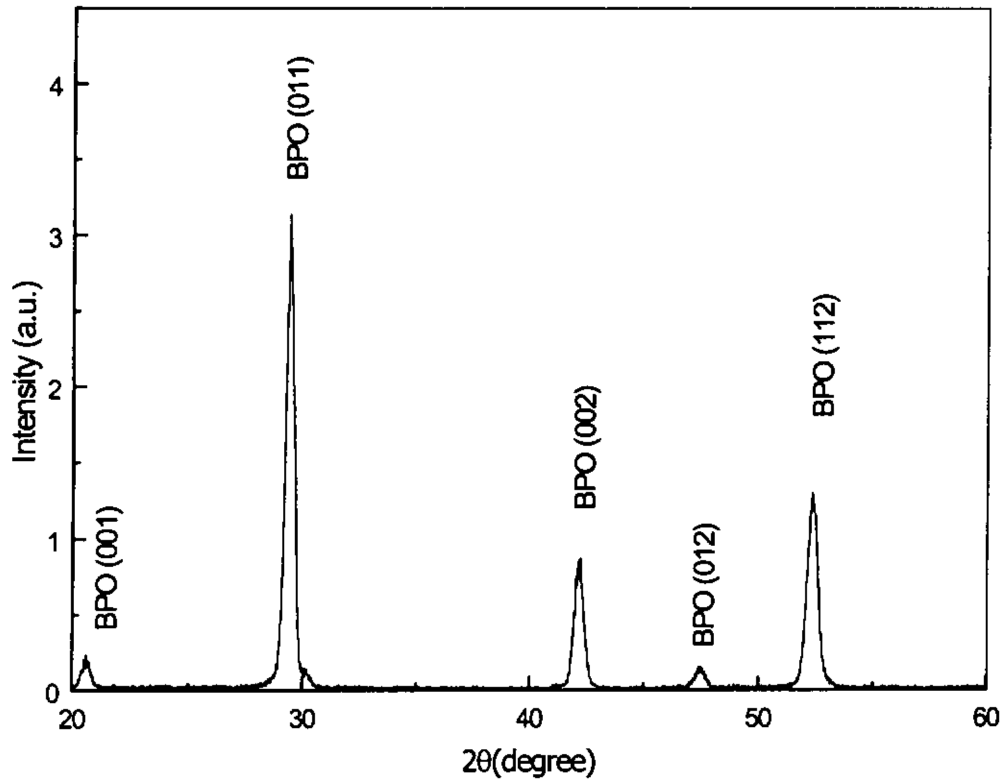

Fig. 6.1 The XRD 2θ-θ profile of the BPO ceramic target.

The heterostructure of $PMN_{0.9}$-$PT_{0.1}$/BPO/LAO was fabricated by PLD. The deposition temperature for $PMN_{0.9}$-$PT_{0.1}$ and BPO films were set at 650°C. The ambient oxygen pressure for growing $PMN_{0.9}$-$PT_{0.1}$ and BPO were 200, and 100 mTorr, respectively.

The XRD 2θ-θ profile of $PMN_{0.9}$-$PT_{0.1}$/BPO/LAO is illustrated in Fig. 6.2. From the figures, highly oriented single perovskite phase of $PMN_{0.9}$-$PT_{0.1}$ and BPO films are observed. The out-of-plane orientation of the $PMN_{0.9}$-$PT_{0.1}$(002) and BPO (002) peaks were examined by ω–scan. The FWHM of the rocking curve of $PMN_{0.9}$-

$PT_{0.1}$(002) and BPO(002) are 0.93° and 0.82°, respectively. These values reveal very good out-of-plane orientations of the $PMN_{0.9}$-$PT_{0.1}$ and BPO films.

The XRD ϕ–scan was performed to confirm the hereroepitaxial growth of the films. The XRD ϕ–scans of $PMN_{0.9}$-$PT_{0.1}$(202), BPO(202), and LAO(202) are shown in Fig. 6.3. The figure suggests that the films are cube-on-cube growth on LAO(001) substrate with an in-plane epitaxial relationship of $(001)_{(0.9)PMN-(0.1)PT}||(001)_{BPO}||(001)_{LAO}$.

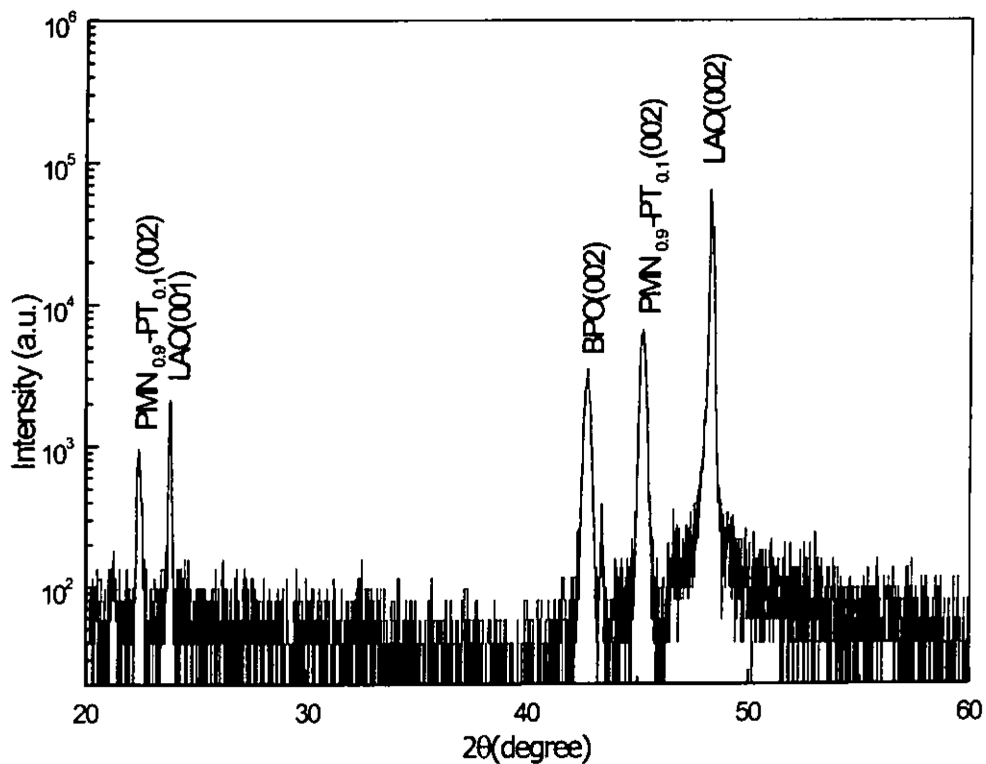

Fig. 6.2 The XRD 2θ-θ profile of the $PMN_{0.9}$-$PT_{0.1}$/BPO/LAO film.

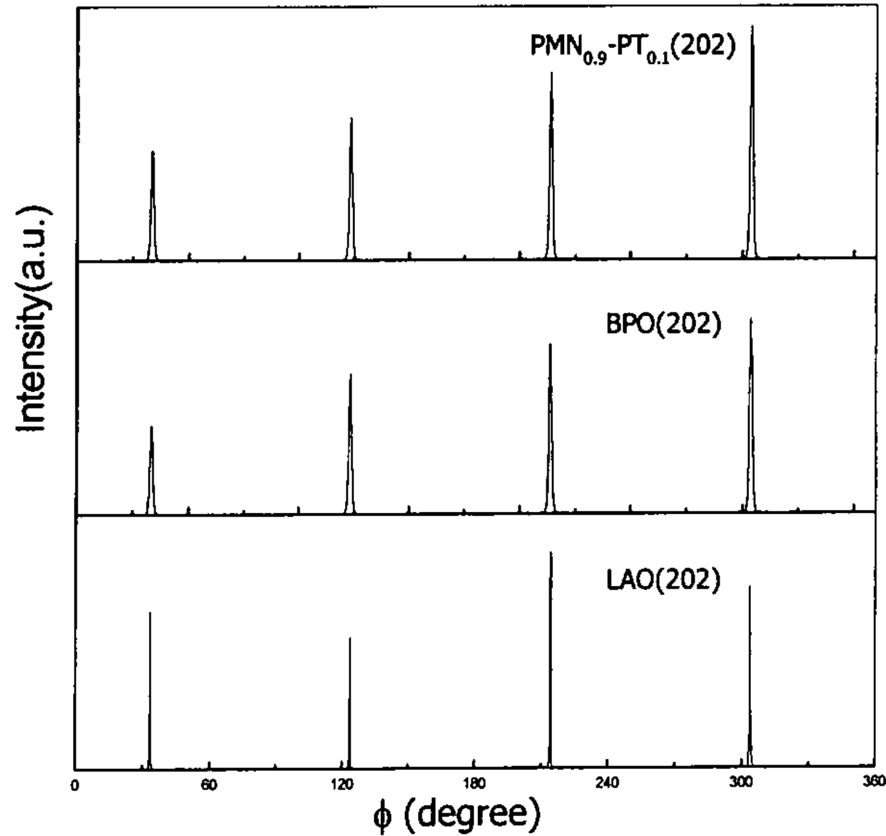

Fig. 6.3 The φ–scan of the $PMN_{0.9}$-$PT_{0.1}$(202), BPO(202), and LAO(202).

6.2.2 Surface morphology

Fig. 6.4 shows the SEM image of a $PMN_{0.9}$-$PT_{0.1}$ film. It is seen that the grain size of $PMN_{0.9}$-$PT_{0.1}$ film is quite small. Some outgrowths emerge from the smooth matrix. The size of outgrowths is in the range from 100nm to 200nm. From the cross-sectional SEM image, shape boundary between the $PMN_{0.9}$-$PT_{0.1}$ and BPO layers can be clearly identified. The thickness of $PMN_{0.9}$-$PT_{0.1}$ film is about 450 nm whereas those of the BPO is about 300 nm.

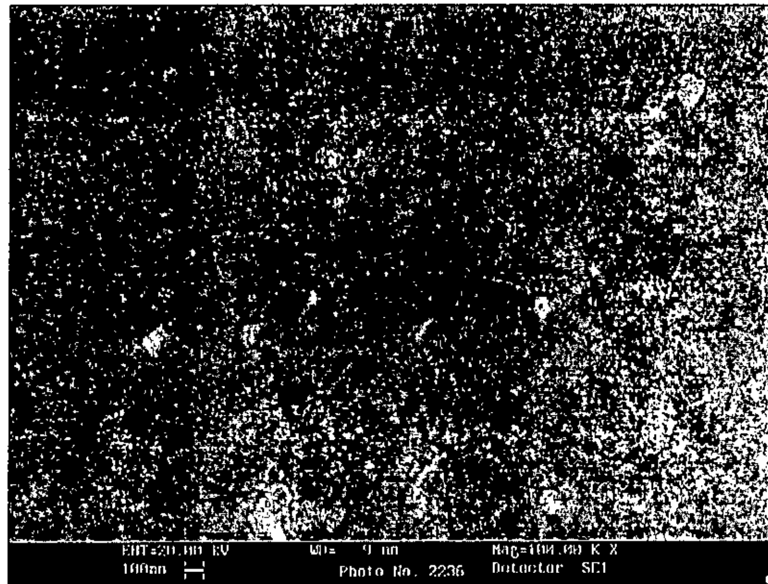

Fig. 6.4a The SEM surface image of $PMN_{0.9}$-$PT_{0.1}$/BPO/LAO film.

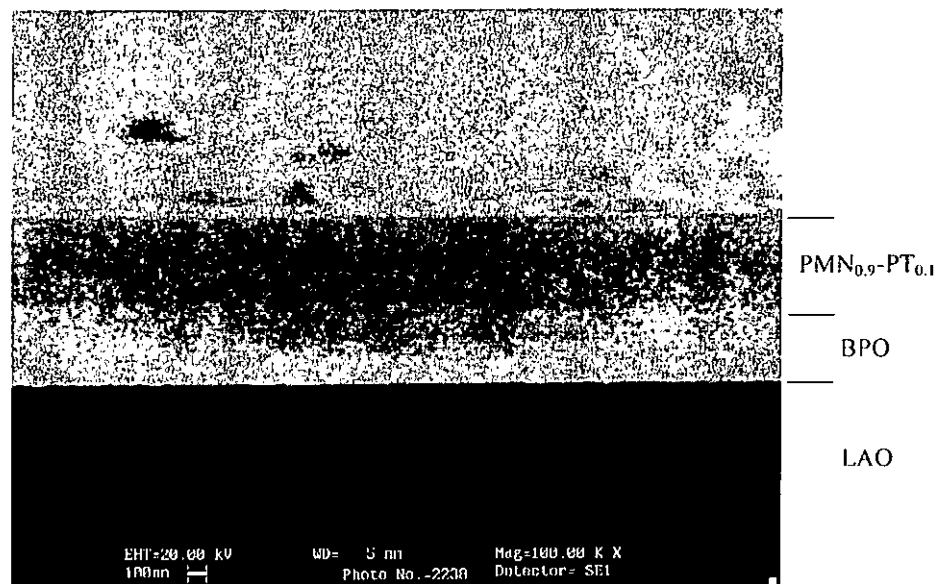

Fig. 6.4b The SEM cross-sectional image of $PMN_{0.9}$-$PT_{0.1}$/BPO/LAO film.

6.2.3 Leakage current and dielectric constant measurement

The leakage current density versus applied voltage for the heterostructure of $PMN_{0.9}$-$PT_{0.1}$/BPO/LAO film is not as small as those in $PMN_{0.9}$-$PT_{0.1}$/LSMO/LAO film. The leakage current density at 1V and 5V are 1.35×10^{-7} A/cm^2 and 0.029 A/cm^2, respectively. It is one order of magnitude larger than the heterostructure of $PMN_{0.9}$-$PT_{0.1}$/LSMO/LAO film with 450 nm $PMN_{0.9}$-$PT_{0.1}$, as shown in Fig. 4.11. For the dielectric measurement, the dielectric constant and dissipation factor at 10 kHz are 781 and 0.14, respectively. The dielectric constant is small compared with 1411 for the heterostructure of $PMN_{0.9}$-$PT_{0.1}$/LSMO/LAO film. The dissipation factor, on the other hand, is large compared with 0.034 for the heterostructure of $PMN_{0.9}$-$PT_{0.1}$/LSMO/LAO film.

From the above results, the electrical properties for the heterostructure of $PMN_{0.9}$-$PT_{0.1}$/BPO/LAO are worse than $PMN_{0.9}$-$PT_{0.1}$/LSMO/LAO. This may be attributed to large lattice mismatch between BPO (4.267 Å) and LAO (3.79 Å). This affects the film quality of $PMN_{0.9}$-$PT_{0.1}$ on BPO/LAO. In order to provide better film quality of BPO to grow $PMN_{0.9}$-$PT_{0.1}$ film, BPO was then grown on MgO (4.21 Å) single crystal substrate.

6.3 $PMN_{0.9}$-$PT_{0.1}$ on MgO with BPO bottom electrode

6.3.1 Fabrication and structural characterization of thin film

The heterostructure of $PMN_{0.9}$-$PT_{0.1}$/BPO/MgO was fabricated by the standard PLD method. The deposition condition for $PMN_{0.9}$-$PT_{0.1}$ and BPO films on

MgO substrate was same as previous section. The XRD 2θ-θ profile $PMN_{0.9}$-$PT_{0.1}$/BPO/MgO film is illustrated in Fig. 6.5. Apparently, highly oriented single perovskite phase of $PMN_{0.9}$-$PT_{0.1}$ films has been obtained.

The out-of-plane orientations of the (002) peaks were examined. The XRD ω–scans show that the FWHM of the rocking curve of $PMN_{0.9}$-$PT_{0.1}$(002) and BPO(002) are 0.51° and 0.55°, respectively. These values are much better than those obtained for $PMN_{0.9}$-$PT_{0.1}$/BPO/LAO heterostructure and it indicates an excellent $PMN_{0.9}$-$PT_{0.1}$ out-of-plane orientation.

The XRD φ–scan of $PMN_{0.9}$-$PT_{0.1}$/BPO/MgO was performed. The $PMN_{0.9}$-$PT_{0.1}$(202), BPO(202), and MgO(202) are shown in Fig. 6.6. We can see that the films are cube-on-cube growth on MgO(001) substrate. It shows an in-plane epitaxial relationship of $(001)_{(0.9)PMN-(0.1)PT}||(001)_{BPO}||(001)_{MgO}$.

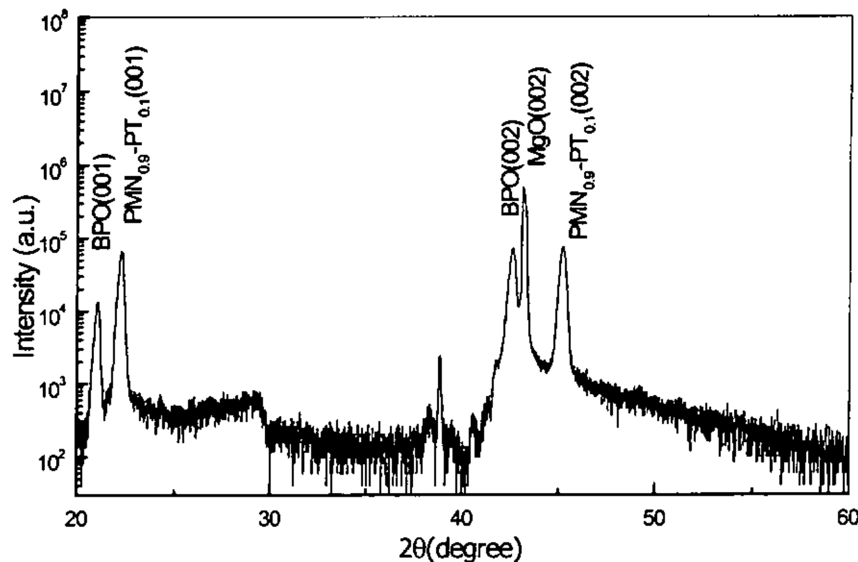

Fig. 6.5 The XRD 2θ-θ profiles of the $PMN_{0.9}$-$PT_{0.1}$/LSMO/MgO film.

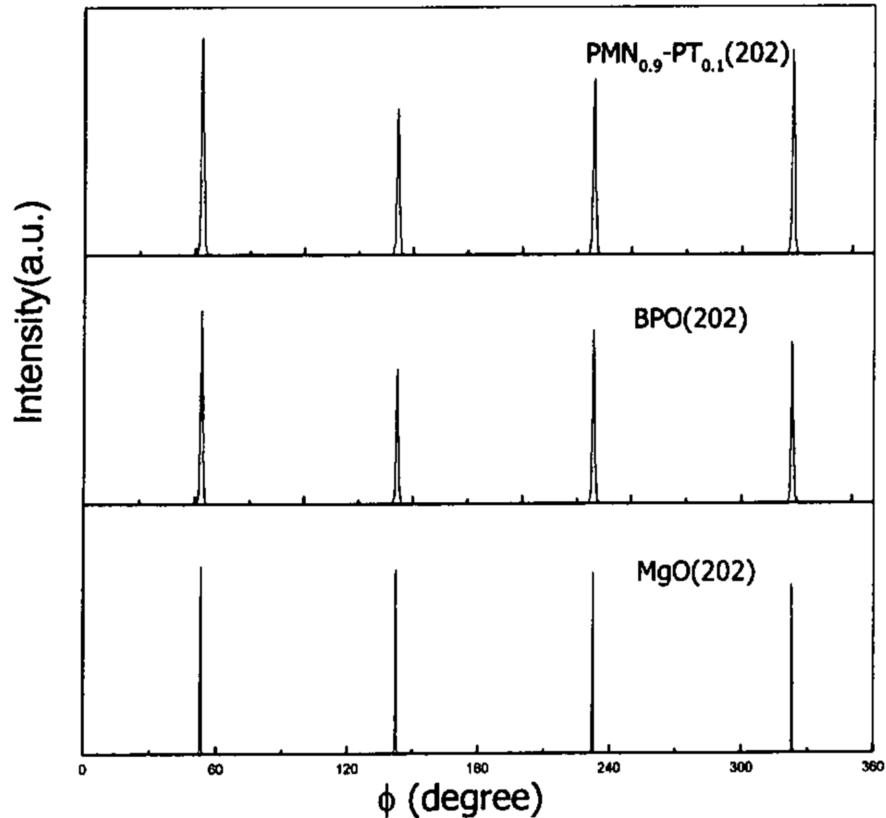

Fig. 6.6 The ϕ–scan of the $PMN_{0.9}$-$PT_{0.1}$(202), BPO(202), and MgO(202).

6.3.2 Surface morphology

Fig. 6.7 illustrates the surface and cross-sectional SEM image of a $PMN_{0.9}$-$PT_{0.1}$/BPO/MgO film. The surface SEM image shows that the grain size of $PMN_{0.9}$-$PT_{0.1}$ film is quite small. There appear some outgrowths too. The cross-sectional SEM image shows distinct boundary between the $PMN_{0.9}$-$PT_{0.1}$ and BPO films. From Fig. 6.7b, the $PMN_{0.9}$-$PT_{0.1}$ and LSMO layers can be easily distinguished. The thicknesses of the $PMN_{0.9}$-$PT_{0.1}$ and BPO films are about 450 nm and 300 nm, respectively.

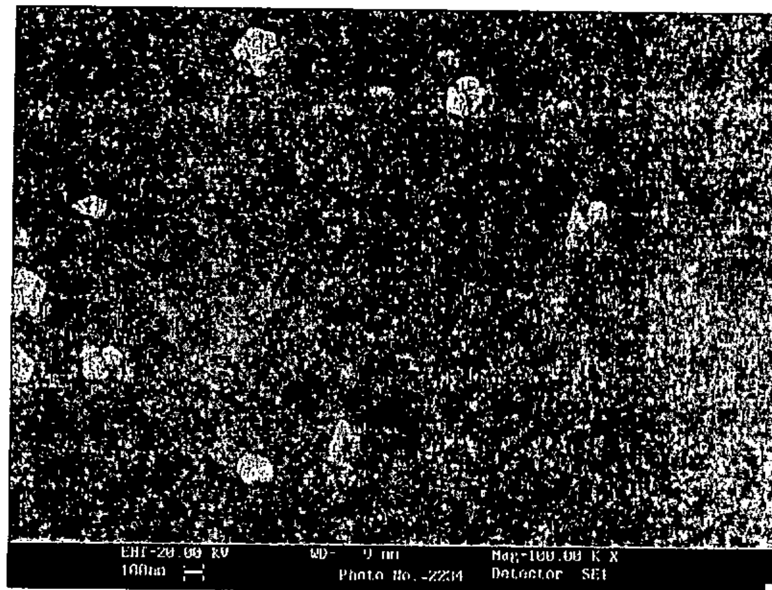

Fig. 6.7a The SEM surface image of $PMN_{0.9}$-$PT_{0.1}$/BPO/MgO.

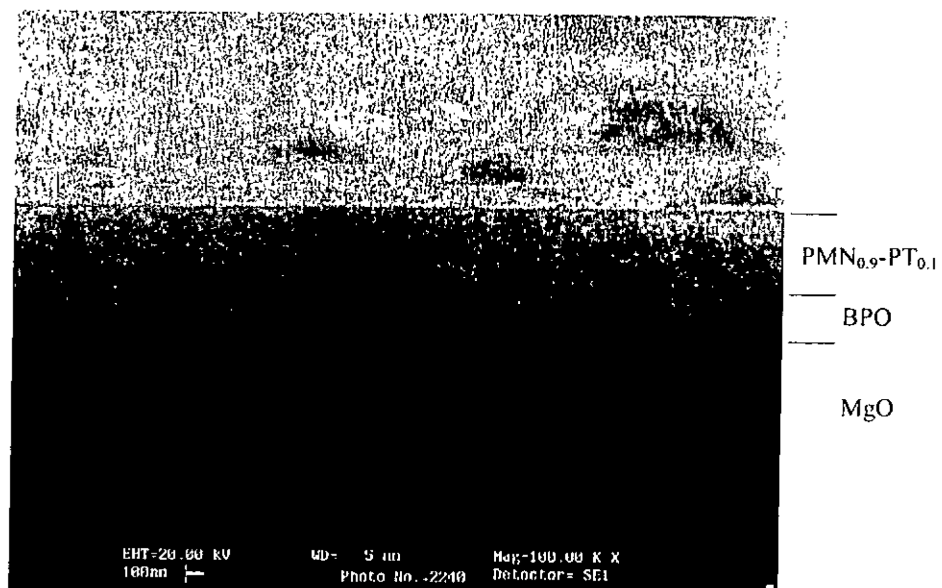

Fig. 6.7b The SEM cross-sectional image of $PMN_{0.9}$-$PT_{0.1}$/BPO/MgO.

6.3.3 Electrical properties

6.3.3.1 Leakage current measurement

The electrical properties of $PMN_{0.9}$-$PT_{0.1}$/BPO/MgO heterostructure were measured with top spot Au electrodes of 200 μm diameter. The leakage current density versus applied voltage for the $PMN_{0.9}$-$PT_{0.1}$/BPO/MgO film is shown in Fig. 6.8. By comparing with $PMN_{0.9}$-$PT_{0.1}$/BPO/LAO film, the leakage current density of $PMN_{0.9}$-$PT_{0.1}$/BPO/MgO film is much smaller. The leakage current density at 1V is 6.97×10^{-8} A/cm^2. This low leakage current density is probable due to the result of good crystalline of the heterostructure of $PMN_{0.9}$-$PT_{0.1}$/BPO/MgO film.

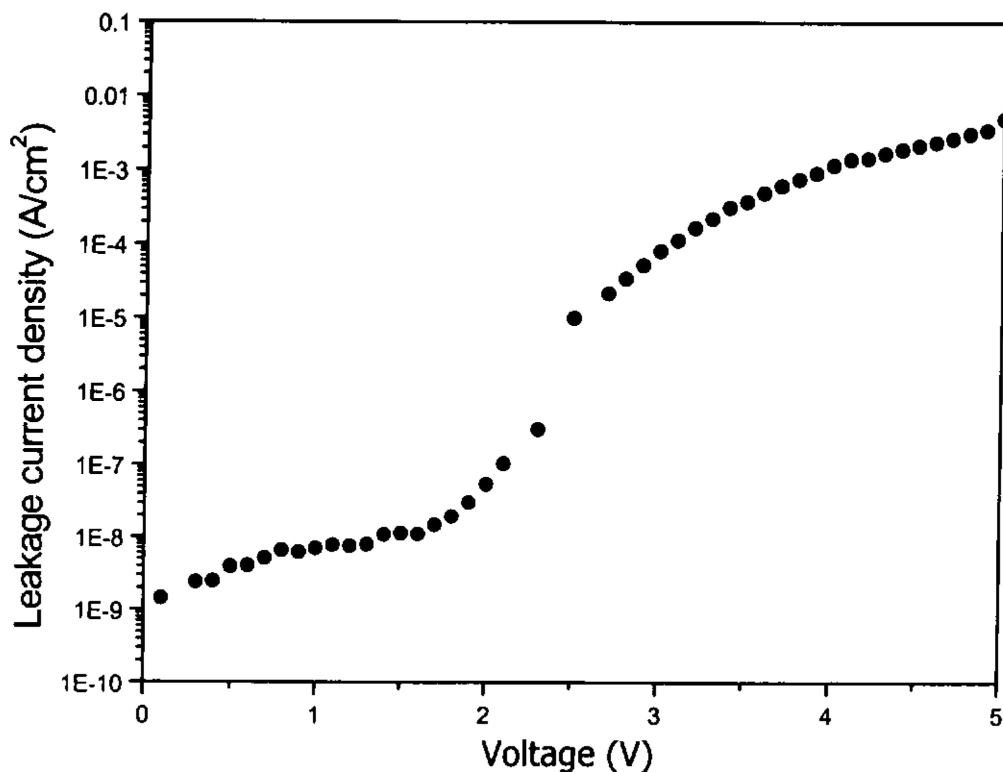

Fig. 6.8 The leakage current density versus applied voltage for the heterostructure of $PMN_{0.9}$-$PT_{0.1}$/BPO/MgO film.

6.3.3.2 Dielectric measurement

Fig. 6.9 shows the dielectric constant of $PMN_{0.9}$-$PT_{0.1}$/BPO/MgO film. The dielectric constant and the dissipation factor at 10 kHz are 1596 and 0.06, respectively. The dielectric constant is larger than the $PMN_{0.9}$-$PT_{0.1}$/LSMO/LAO film (1411) and $PMN_{0.9}$-$PT_{0.1}$/BPO/LAO film (781).

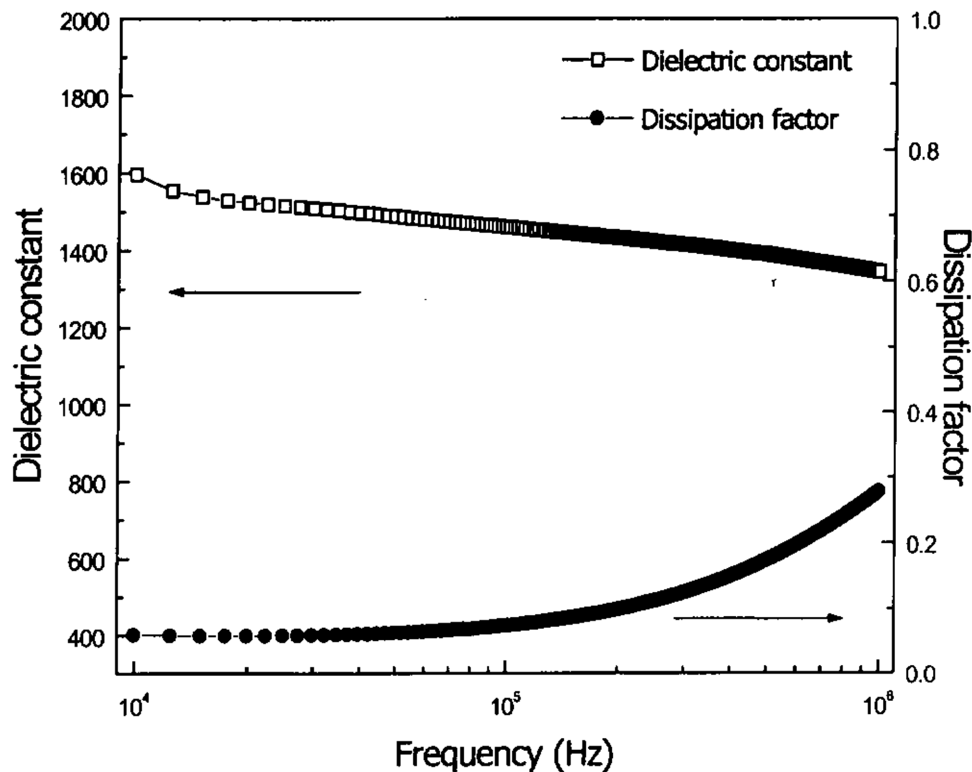

Fig. 6.9 The dielectric constant and dissipation factor of $PMN_{0.9}$-$PT_{0.1}$ film for the heterostructure of $PMN_{0.9}$-$PT_{0.1}$/LSMO/LAO.

6.4 $PMN_{0.9}$-$PT_{0.1}$ on Pt/Si with LSMO and BPO oxide electrodes

6.4.1 Fabrication and structural characterization of thin films

$PMN_{0.9}$-$PT_{0.1}$ films were fabricated on Pt/Si substrate with LSMO and BPO oxide electrode. The deposition temperature for growing $PMN_{0.9}$-$PT_{0.1}$, LSMO, and BPO films were all set at 650°C. The ambient oxygen pressure during deposition of $PMN_{0.9}$-$PT_{0.1}$, LSMO, and BPO were 200, 150, and 100 mTorr, respectively.

The XRD 2θ-θ profiles of $PMN_{0.9}$-$PT_{0.1}$/Pt/Si, $PMN_{0.9}$-$PT_{0.1}$/LSMO/Pt/Si, and $PMN_{0.9}$-$PT_{0.1}$/BPO/Pt/Si films are shown in Fig. 6.10. For the $PMN_{0.9}$-$PT_{0.1}$/Pt/Si film, pyrochlore phase dominates and only very weak $PMN_{0.9}$-$PT_{0.1}$ perovskite phase is seen. The pyrochlore diffraction peaks show much higher intensities than the perovskite ones. It is common for obtaining pyrochlore phase films. Tantigate's experimental result showed that the pyrochlore phase appeared for all deposition temperature on Pt/Si substrate [Tantigate et al., 1996]. Nakamura et al. also obtained similar experimental results [Nakamura et al., 1996]. By considering the lattice constant, Pt, the perovskite and pyrochlore phase are 3.92Å, 4.03Å, and 10.59Å, respectively. The lattice mismatch between Pt and perovskite phase is much smaller than that between Pt and pyrochlore phase. The mechanism for obtaining this result is still not very well known [Lee et al., 2001].

From Fig. 6.10b and 6.10c, no pyrochlore diffraction peak can be observed and these films have single pervoskite phase. It is revealed that pervoskite oxide

electrodes have a function to promote the formation of pervoskite phase. For the $PMN_{0.9}$-$PT_{0.1}$/LSMO/Pt/Si, the strongest XRD diffraction peak from pervoskite phase is the (011) peak. It is much higher than all other diffraction peaks. This indicates that the $PMN_{0.9}$-$PT_{0.1}$ is (011) preferentially oriented. Similarly, for the $PMN_{0.9}$-$PT_{0.1}$ /BPO/Pt/Si, the highest XRD diffraction peak from pervoskite phase is the (111) peak. This means that the $PMN_{0.9}$-$PT_{0.1}$ film is (111) preferentially oriented. The different orientation of $PMN_{0.9}$-$PT_{0.1}$ films for the two oxide electrodes may be attributed to different lattice constant of the oxide electrodes and the crystal plane surface energy. The exact mechanism controlling the orientation growth is however not known.

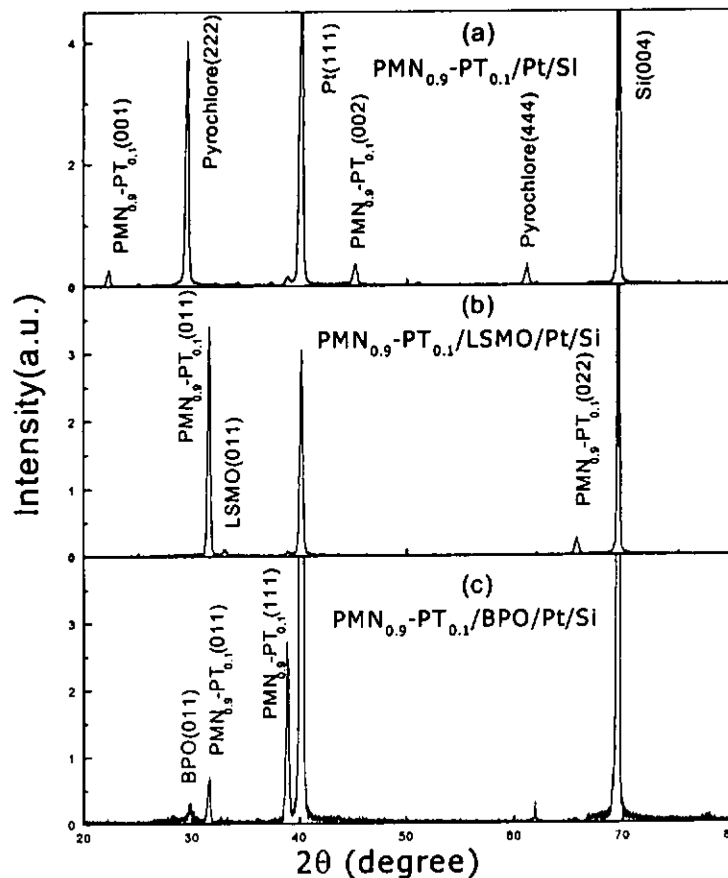

Fig. 6.10 The XRD 2θ-θ profiles of the $PMN_{0.9}$-$PT_{0.1}$ films for three different bottom electrodes.

6.4.2 Surface morphology

Fig. 6.11 to Fig. 6.13 show the SEM images of $PMN_{0.9}$-$PT_{0.1}$/Pt/Si, $PMN_{0.9}$-$PT_{0.1}$/LSMO/Pt/Si, and $PMN_{0.9}$-$PT_{0.1}$/BPO/Pt/Si films. Fig. 6.11 depicts the surface and cross-sectional SEM images of $PMN_{0.9}$-$PT_{0.1}$ film grown on Pt without oxide electrode. It can be seen that the surface of the $PMN_{0.9}$-$PT_{0.1}$ film is composed of grains of 10 – 100 nm diameter. The cross-sectional SEM image shows columnar structure aligned along the out-of-plane direction.

Fig. 6.12 and Fig 6.13 show the surface and cross-sectional SEM images of $PMN_{0.9}$-$PT_{0.1}$ thin film with LSMO and BPO electrodes. The two surfaces are quite different, $PMN_{0.9}$-$PT_{0.1}$ thin film with LSMO electrode exhibits a more well defined grain structure. The grain size is larger and some grains are in triangular shape. On the other hand, the grain of the $PMN_{0.9}$-$PT_{0.1}$ thin film with BPO electrode is in circular shape and the grain size is smaller. The difference in microstructures between these $PMN_{0.9}$-$PT_{0.1}$ films may be attributed to orientation. Regarding to the cross-sectional SEM image, $PMN_{0.9}$-$PT_{0.1}$ thin film with LSMO electrode shows clear and prominent columnar structure running from bottom to top of the film. The $PMN_{0.9}$-$PT_{0.1}$ film thickness is about 530 nm. The $PMN_{0.9}$-$PT_{0.1}$ film with BPO electrode is about 450 nm thick. No apparent columnar structure is seen. The XRD pattern reveals a mixture of (011) and (111) oriented grains.

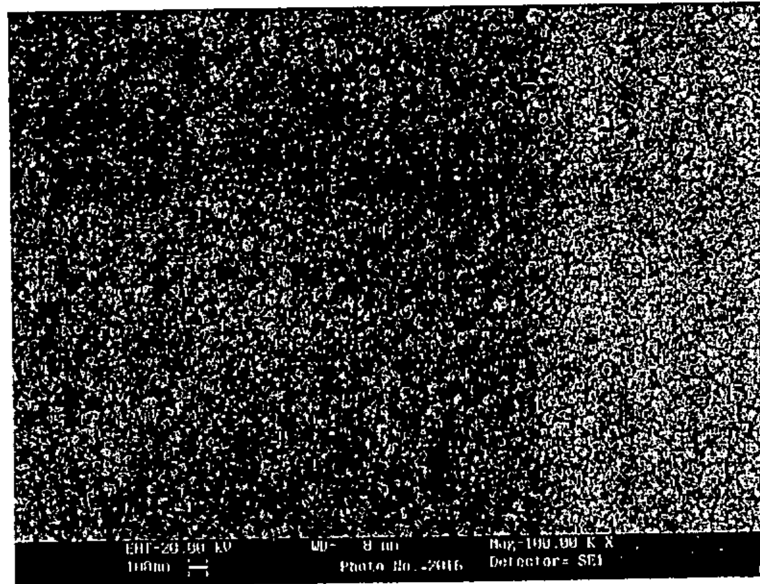

Fig. 6.11a The SEM surface image of $PMN_{0.9}$-$PT_{0.1}$/Pt/Si.

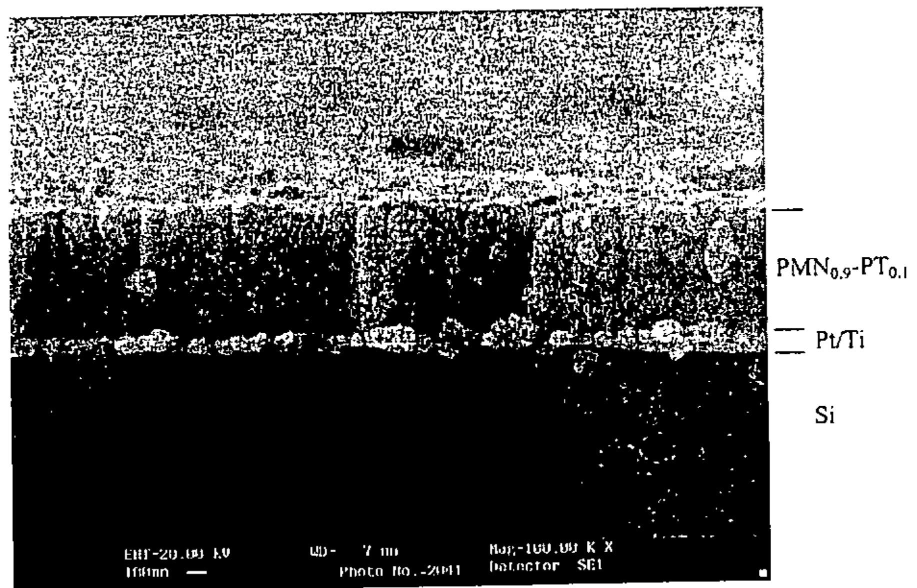

Fig. 6.11b The SEM cross-sectional image of $PMN_{0.9}$-$PT_{0.1}$ /Pt/Si.

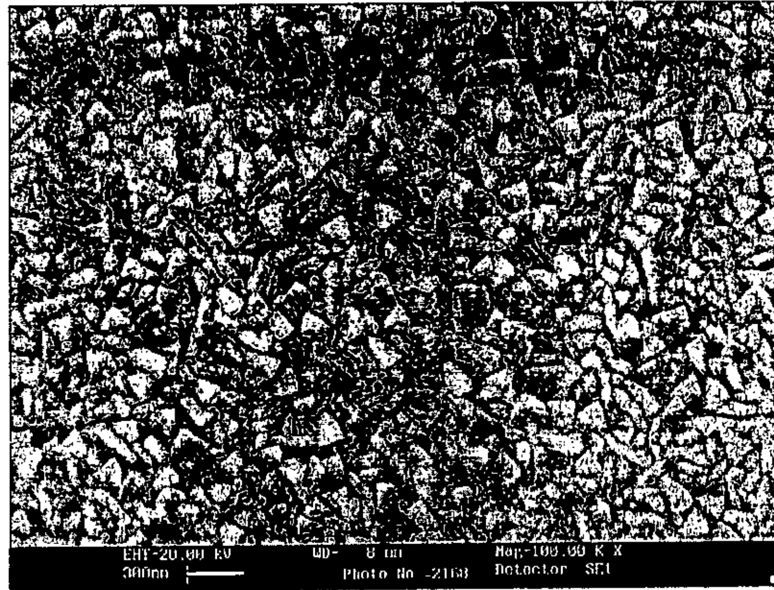

Fig. 6.12a The SEM surface image of $PMN_{0.9}$-$PT_{0.1}$/LSMO/Pt/Si.

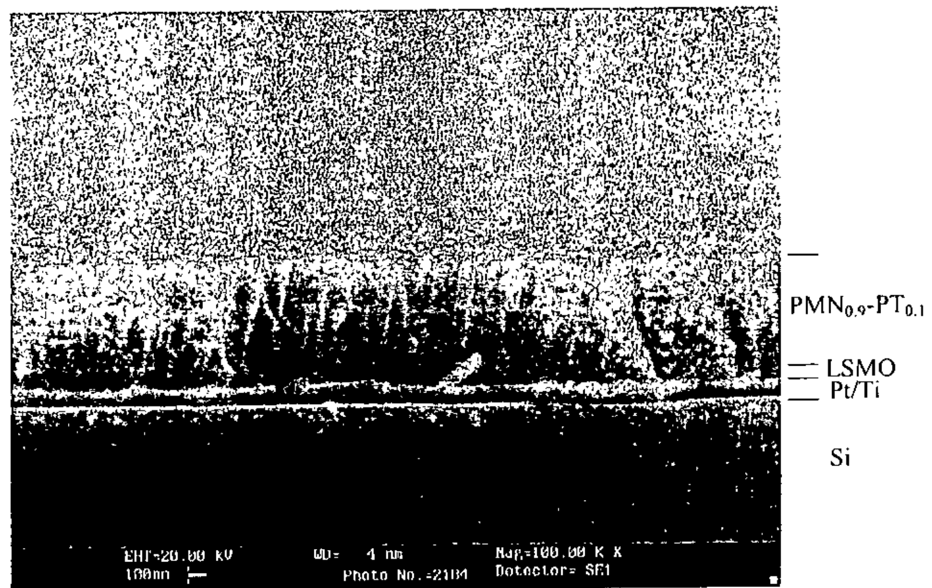

Fig. 6.12b The SEM cross-sectional image of $PMN_{0.9}$-$PT_{0.1}$/LSMO/Pt/Si.

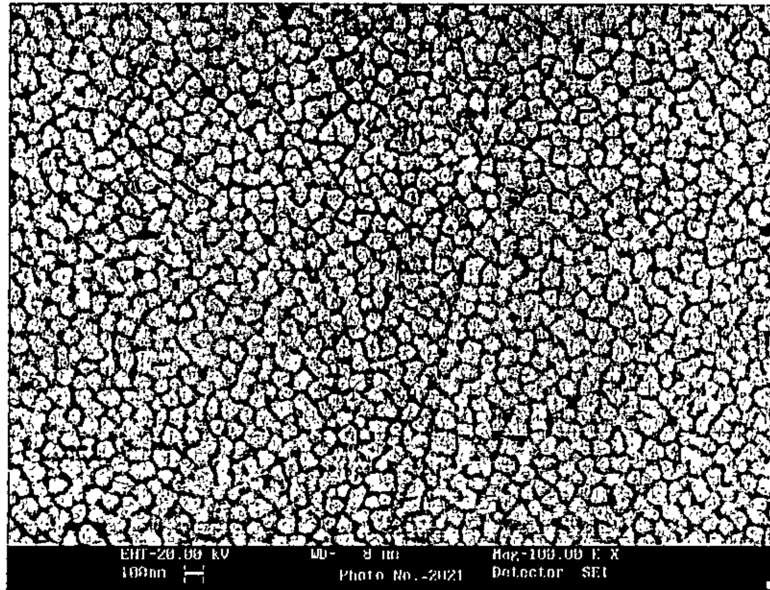

Fig. 6.13a The SEM surface image of $PMN_{0.9}$-$PT_{0.1}$/BPO/Pt/Si.

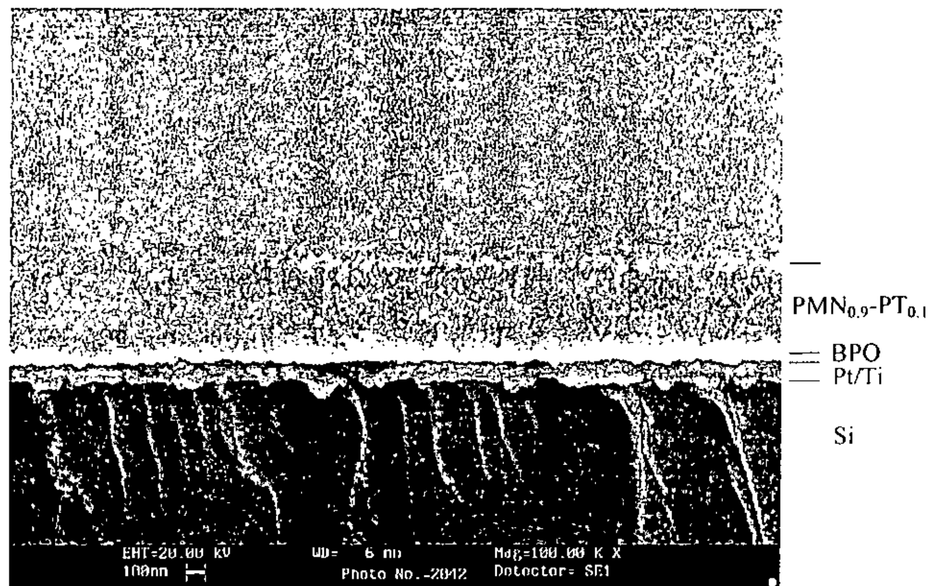

Fig. 6.13b The SEM cross-sectional image of $PMN_{0.9}$-$PT_{0.1}$/BPO/Pt/Si.

6.4.3 Electrical properties

6.4.3.1 Leakage current measurement

The leakage current density versus applied voltage profiles for the three heterostructures are shown in Fig. 6.14. Throughout the voltage range studied, $PMN_{0.9}$-$PT_{0.1}$/Pt/Si has the largest leakage current density and $PMN_{0.9}$-$PT_{0.1}$/BPO/Pt/Si has the lowest leakage current density. The leakage current densities at 1V are $1.07x10^{-7}$ A/cm^2, $2.00x10^{-8}$ A/cm^2, and $6.78x10^{-9}$ A/cm^2 for the heterostructure of $PMN_{0.9}$-$PT_{0.1}$/Pt/Si, $PMN_{0.9}$-$PT_{0.1}$/LSMO/Pt/Si, and $PMN_{0.9}$-PT-$_{0.1}$/BPO/Pt/Si, respectively. This result agrees with the result of Luo et al. [Luo et al., 2001]. They demonstrated that PZT films deposited on the BPO/Pt electrode exhibit leakage current one order of magnitude lower than that of the film deposited on the Pt electrode. It has also been demonstrated that the leakage current density is small by using hybrid electrodes with Pt and oxides [Al-Shareef et al., 1995].

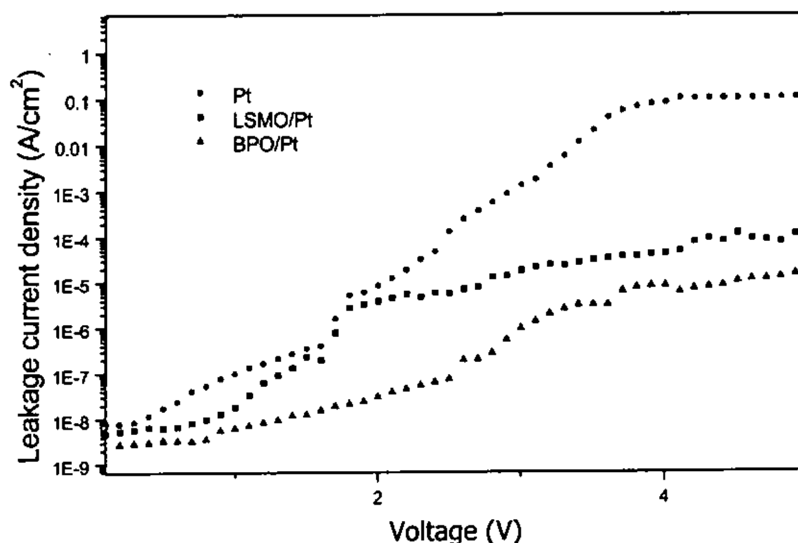

Fig. 6.14 The leakage current density versus applied voltage for the heterostructure of $PMN_{0.9}$-$PT_{0.1}$ for different electrodes.

6.4.3.2 Dielectric measurement

The dielectric constant of the heterostructure of $PMN_{0.9}$-$PT_{0.1}$/Pt/Si, $PMN_{0.9}$-$PT_{0.1}$/LSMO/Pt/Si, and $PMN_{0.9}$-$PT_{0.1}$/BPO/Pt/Si are illustrated in Fig. 6.15. This figure reveals that $PMN_{0.9}$-$PT_{0.1}$ film coated on Pt/Si film has the smallest dielectric constant. It is because the $PMN_{0.9}$-$PT_{0.1}$ film contains almost all pyrochlore phase. The dielectric constant of pyrochlore phase is much lower than the pervoskite phase. The dissipation factor of $PMN_{0.9}$-$PT_{0.1}$ coated on Pt/Si is the lowest among all. This is probably because the resistance of Pt is the least. The dielectric constants of $PMN_{0.9}$-$PT_{0.1}$/Pt/Si, $PMN_{0.9}$-$PT_{0.1}$/LSMO/Pt/Si, and $PMN_{0.9}$-$PT_{0.1}$/BPO/Pt/Si films are 406, 1409, and 1750, respectively, at 10kHz. Their corresponding dissipation factors are 0.053, 0.076 and 0.056, respectively, at 10kHz.

The dielectric constant of $PMN_{0.9}$-$PT_{0.1}$/BPO/Pt/Si film is the largest. It shows that the BPO electrode improves the quality of interfacial layer and increases the dielectric constant of the $PMN_{0.9}$-$PT_{0.1}$ layer. Consequently, an increase of the net dielectric constant of $PMN_{0.9}$-$PT_{0.1}$ film results.

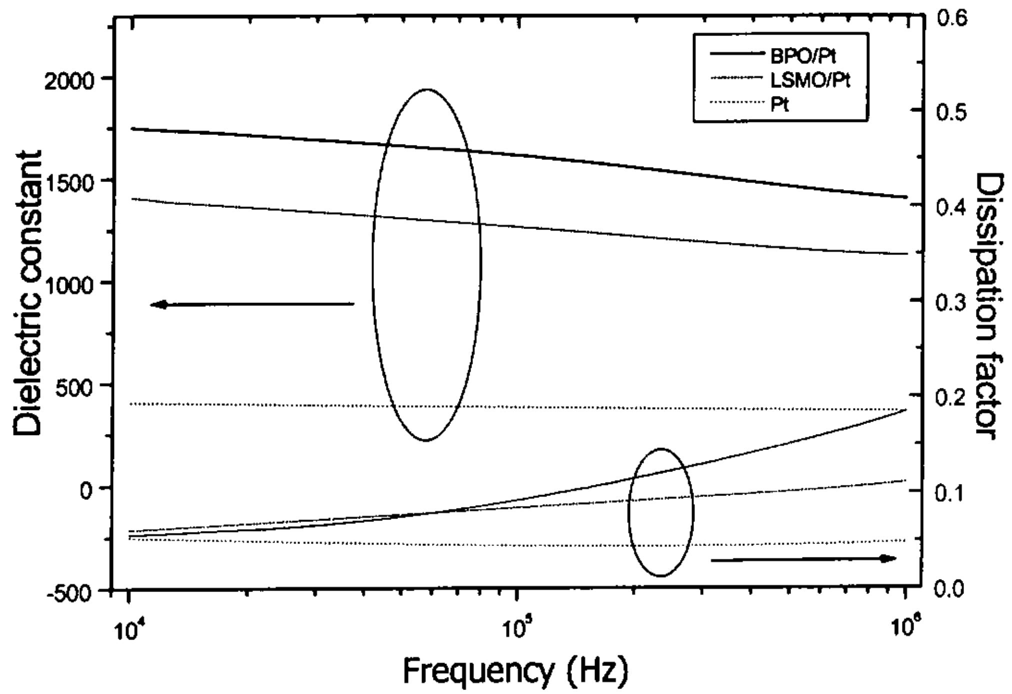

Fig. 6.15 The dielectric constant and dissipation factor of $PMN_{0.9}$-$PT_{0.1}$ film for different electrodes.

Chapter Seven

Conclusions

$PMN_{0.9}$-$PT_{0.1}$ and $PMN_{0.65}$-$PT_{0.35}$ films were fabricated on LAO single crystal substrate with LSMO bottom electrode. Heteroepitaxial relationships of $(001)_{(0.9)PMN-(0.1)PT}||(001)_{LSMO}||(001)_{LAO}$ and $(001)_{(0.65)PMN-(0.35)PT}||(001)_{LSMO}||(001)_{LAO}$ were obtained when the film were deposited at 650°C and under an ambient of 200 mTorr oxygen. The out-of-plane lattice constants of PMN0.9-PT0.1 and PMN0.65-PT0.35 films were 0.401 and 0.398 nm, respectively. The leakage current density of the $PMN_{0.65}$-$PT_{0.35}$ film was slightly larger than that of the $PMN_{0.9}$-$PT_{0.1}$ film. Furthermore, the dielectric constant measurements carried out at room temperature reveal a bigger value for $PMN_{0.9}$-$PT_{0.1}$ than for $PMN_{0.65}$-$PT_{0.35}$. It can be concluded that the dielectric properties of $PMN_{0.9}$-$PT_{0.1}$ is better than $PMN_{0.65}$-$PT_{0.35}$ film at room temperature for use in DRAM capacitor.

Thickness dependence of the $PMN_{0.9}$-$PT_{0.1}$ films grown on LSMO/LAO was studied. $PMN_{0.9}$-$PT_{0.1}$ films of 70, 120, 250, 400, and 450 nm thick were fabricated. The SEM surface image showed that there was no apparent correlation between grain size and film thickness. The leakage current densities at 1V for the 400 and 450 nm $PMN_{0.9}$-$PT_{0.1}$ films were 3.87×10^{-8}, and 2.35×10^{-8} A/cm^2, respectively. The leakage current was much larger for the 70, 120, and 250 nm $PMN_{0.9}$-$PT_{0.1}$ films. The dielectric constant of $PMN_{0.9}$-$PT_{0.1}$ films was seen to

increase with thickness. The dielectric constant of the 450 nm $PMN_{0.9}$-$PT_{0.1}$ film was 1411. The dissipation factor, on the other hand, decreases with increasing film thickness. From data of our investigation, we believe that the decrease of dielectric constant with film thickness is not related to the grain size but probable due to the existence of interfacial layer between the dielectric and oxide electrode films.

The effect of growth temperature on the properties of $PMN_{0.9}$-$PT_{0.1}$ films were studied also. $PMN_{0.9}$-$PT_{0.1}$ films were fabricated on MgO single crystal substrate with LSMO bottom electrode at temperatures of 600°C, 625°C, and 650°C. In-plane epitaxial relationship of $(001)_{(0.9)PMN-(0.1)PT}||(001)_{LSMO}||(001)_{MgO}$ was obtained for all these deposition temperatures. The leakage current density was reasonably small for $PMN_{0.9}$-$PT_{0.1}$ films deposited at 625°C and 650°C but large for those grown at 600°C. The dielectric constant was 1435 at 10kHz for $PMN_{0.9}$-$PT_{0.1}$ deposited at 650°C and it decreased with deposition temperature. This may simply due to the fact that better crystalline $PMN_{0.9}$-$PT_{0.1}$ films are obtained at higher temperatures.

$PMN_{0.9}$-$PT_{0.1}$ were also fabricated on MgO/TiN buffered Si(100) substrates with LSMO bottom electrode. No pyrochlore phase but a highly oriented single perovskite phase of $PMN_{0.9}$-$PT_{0.1}$ film was observed and heteroepitaxial relationship of $(001)_{(0.9)PMN-(0.1)PT}||(001)_{LSMO}||(001)_{MgO}||(001)_{TiN}||(001)_{Si}$ was demonstrated. However, its leakage current was much larger than those of $PMN_{0.9}$-$PT_{0.1}$ films grown on LAO and MgO substrates. The dielectric constant at 10 kHz was 1414 but it decreased dramatically with increasing frequency. The dissipation factor was quite

large compared with that of $PMN_{0.9}$-$PT_{0.1}$ films grown on LAO and MgO substrates. The inferior electric properties of these $PMN_{0.9}$-$PT_{0.1}$ films may be due to the degraded crystallinity of the $PMN_{0.9}$-$PT_{0.1}$ films and large particulates on the film surface by PLD process. The latter is a particular acute problem due to the accumulation effect for multi-layer fabrication. The particulate problem can be eliminated by inserting a shadow mask between target and substrate during film deposition. It is believed that the reduction of particulate can improve the electrical properties.

Pb-based perovskite conductive oxide electrode (BPO) was introduced to minimize the inter-diffusion of Pb between dielectric film and oxide electrode. Epitaxial $PMN_{0.9}$-$PT_{0.1}$ films were fabricated on LAO single crystal substrate with BPO bottom electrode. Nevertheless, the electrical properties were no better than the heterostructrue of $PMN_{0.9}$-$PT_{0.1}$/LSMO/LAO. This may be due to large lattice mismatch between BPO and LAO. Then epitaxial $PMN_{0.9}$-$PT_{0.1}$ film was grown on BPO/MgO. The electrical properties were improved. The leakage current density at 1V was 6.97×10^{-8} A/cm^2. It is probable due to better crystalline of the heterostructure of $PMN_{0.9}$-$PT_{0.1}$/BPO/MgO. The dielectric constant and the dissipation factor at 10 kHz were 1596 and 0.06, respectively.

$PMN_{0.9}$-$PT_{0.1}$ were then fabricated on Pt/Si substrate with and without LSMO or BPO oxide electrode. The properties of heterostructures of $PMN_{0.9}$-$PT_{0.1}$/Pt/Si, $PMN_{0.9}$-$PT_{0.1}$/LSMO/Pt/Si, and $PMN_{0.9}$-$PT_{0.1}$/BPO/Pt/Si were measured

and compared. From the XRD profile, prominent pyrochlore phase of $PMN_{0.9}$-$PT_{0.1}$ appeared in the $PMN_{0.9}$-$PT_{0.1}$/Pt/Si film. Pyrochlore-free and single perovskite phase $PMN_{0.9}$-$PT_{0.1}$ films were obtained for the heterostructures of $PMN_{0.9}$-$PT_{0.1}$/LSMO/Pt/Si and $PMN_{0.9}$-$PT_{0.1}$/BPO/Pt/Si. $PMN_{0.9}$-$PT_{0.1}$ was (011) preferentially oriented for $PMN_{0.9}$-$PT_{0.1}$/LSMO/Pt/Si film. On the other hand, $PMN_{0.9}$-$PT_{0.1}$ (111) preferentially oriented film was obtained for $PMN_{0.9}$-$PT_{0.1}$/LSMO/Pt/Si film. The SEM images of the two surfaces were quite different. This may be attributed to the difference in crystalline orientation. Among these three films, $PMN_{0.9}$-$PT_{0.1}$/BPO/Pt/Si showed the smallest leakage current density (6.78×10^{-9} A/cm^2 at 1V) and the largest dielectric constant (1750 at 10kHz). It is believed that the BPO electrode improves the quality of interfacial layer as well as the electrical properties of $PMN_{0.9}$-$PT_{0.1}$ film.

In short, Au/$PMN_{0.9}$-$PT_{0.1}$/BPO/Pt/Si of good electrical properties has been demonstrated. Our work has illustrated that PMN-PT integration with Si is possible (both heterostructures and heteroepitaxial structures). However, in view of the ultra-large dielectric constant of bulk PMN-PT (>30,000), it appears that there is plenty of room for improved electrical performance of the PMN-PT films. As we have mentioned earlier, inserting a shadow mask between target and substrate to eliminate the particulate during film deposition may help. A more thorough understanding of the interface physics involved and a more controlled film growth process are needed. Lastly, in order to introduce $PMN_{0.9}$-$PT_{0.1}$ film for DRAM capacitor application, further studies on reproducibility, thermal stability and operation reliability are required.

References

Abe, K., and Komatsu, S., *Jpn. J. Appl. Phys., Part 1* **31**, 2985 (1992)

Al-shareef, H. N., Auciello, O., and Kingon, A. I., *J. Appl. Phys.* 77, 2146 (1995)

Auciello, O., and Waser, R., *Science and Technology of Electroceramic Thin Films*, Kluwer Academic Publishers, London, 1995

Buchanan, R. C., *Ceramic Materials for Electronics*, Marcel Dekker, Inc., New York, (1991)

Cheung, J. T., Gergis, I., James, M., and DeWames, R. E., *Appl. Phys. Lett.* **60**, 3180 (1992)

Chopre, K. L., and Kaur, I., *Thin Film Device Applications*, Plenum Press, New York, (1983)

Chrisey, D. B., and Hubler, G. K., *Pulsed Laser Deposition of Thin Film*, John Wiley & Sons, Inc., New York, 1994

Cross, L. E., *Ferroelectrics* **76**, 241 (1987)

Davis, M. F., Wosik, J., Forster, K., Deshmukh, S. C., Rampersad, H. R., Shah, S., Siemsen, P., Wolfe, J. C., and Economou, D. J., *J. Appl. Phys.* **69**, 7182 (1991)

Dijkkamp, D., Venkatesan, T., Wu, X.D., Shaheen, S.A., Jisrawi, N., Min-Lee, Y.H., McLean, W.L., and Croft, M., *Applied Physics Letter* **51**, 619 (1987)

Elshabini-Riad, A., and Barlow, F. D., III, *Thin Film Technology Handbook*, McGraw-Hill, New York, 1997

Floquet, N., Hector, J., an Gaucher, P., *J. Appl. Phys.* **84**, 3815 (1998)

Fork, D. K., Nashmoto, K., and Geballe, T. H., *Appl. Phys. Lett.* **60**, 1621 (1992)

Gaponov, S.V., Klyuenkov, E.B., Nesterov, B.A., Salashchenko, N.N., and Kheifets, M.I., *Soviet Technical Physics Letters* 193 (1979).

Greer, J. A., and Van Hook, H. J., *Mater. Res. Soc. Symp. Proc.* **191**, 171 (1990)

Greene, J. E. (1993) in Multicomponent and Multilayered Thin Films for Advanced Microtechnologies (O. Auciello and J. Engemann, eds.), NATO/ASI Series E **234**, 39, Kluwer Academic Publishers, The Netherlands (1993)

Hwang, Y. S., Paek, S. H., and Mah, J. P., *J. Mater. Sci. Lett.* **15**, 1030 (1996).

Jang, J. W., Chung, S. J., Cho, W. J., Hahn, R. S., and Choi, S. S., *J. Appl. Phys.* **81**, 6322 (1997)

Joshi, P. C., and Krupanidhi, S. B., *J. Appl. Phys.* **73**, 7627 (1993)

Kawano, H., Morii, K., and Nakayama, Y., *J. Appl. Phys.* **73**, 5141 (1993)

Kim, S. H., Choi, Y. S., Kim, C. E., and Yang, D. Y., *Thin Solid Films* **325**, 72 (1998)

Kotecki, D. E., *Integ. Ferroelec.* **16**, 1 (1997)

Lavric, D., Rao, R. A., Gan, G., Krajrwski, J. J., and Eom, C. B., *Intergrated Ferroelectrics* **21**, 499 (1998)

Lee, S.Y., Custodio, M.C.C., Lim, H.J., Feigelson, R.S., Maria, J.-p., and Trolier-Mckinstry, S., *Journal of Crystal Growth* **226**, 247-253 (2001)

Lee, B. T., and Hwang, C. S., *Appl. Phys. Lett.* **77**, 124 (2000)

Lian, L., and Sottos, N. R., *J. Appl. Phys.* **87**, 3941 (2000)

Lu, Y. L., Gaynor, B., Hsu, C., Jin, G. H., Cronin-Golomb, M., Wang, F. L., Zhao, J., Wang, S.-Q., Yip, P., and Drehman, A. J., *Appl. Phys. Lett.* **74**, 3038 (1999)

Luo, Y. R., and Wu, J. M., *Appl. Phys. Lett.* **79**, 3669 (2001)

Matsumuro, Y., Oishi, Y., and Okuyama, M., *Journal of the Korean Physical society* **32**, S1625 (1998)

Misman, O., Bhattacharya, S. K., Erbil, A., and Tummala, R. R., *Journal of Material Science: Materials in Electrons*, **11** (2000) 657-660

Nagaraj, B., Aggarwal, S., and Ramesh, R., *J. Appl Phys.* **90**, 375 (2001)

Nagarajan, V., Ganpule, C. S., Nagaraj, B., Aggarwl, S., Alpay, S. P., Roytburd, A. L., Williams, E. D., and Ramesh, R., *Appl. Phys. Lett.* **75**, (1999) 4183

Nakamura, T., Masuda, A., Morimoto, A., and Shimizu, T., *Jpn. J. Appl. Phys.* **35**, 4750 (1996)

Namiki, A., Kawai, T., and Ichige, K., *Surface Science*, **166**, 129 (1986)

Narayan, J., Tiwari, P., Chen, X., Singh, J., Chowdhury, R., and Zheleva, T., *Appl. Phys. Lett.* **61**, 1290 (1992)

Nitta, T., Nagase, K., Hayakawa, S., and Iida, Y., *J. Am. Ceram. Soc.* **48**, 642 (1965)

Noblanc, O., Guacher, P., and Calvarin, G., *J. Appl. Phys.* **79**, 4291 (1996)

Nomura, S., and Uchino, K., *Ferroelectrics* **41**, 117 (1982)

Park, J. H., Kim, B. K., Song, K. H., and Park, S. J., *Materials Research Bulletin* **30**, 435 (1994)

Park, S. E., and Shrout, T. R., *IEEE Trans. Ultrason. Ferroelectr. Freq. Control* **44**, 1140 (1997)

Prince, B., *High Performance Memories*, John Wiley & Sons, LTD, New York, (1996)

Ramesh, R., Luther, K., Wilkens, B., Hart, D. L., Wang, E., Tarascon, J. M., Inam, A., Wu, X. D., and Venkatesan, T., *Appl. Phys. Lett.* **57**, 1505 (1990)

Ramesh, R., *Thin Film Ferroelectric Materials and Devices,* Kluwer Academic Publishers, Boston, (1997)

Scott, J. F., *Ferroelectric Memories*, Springer, Berlin, (2000)

Shrout, T. R., Chang, Z. P., Kim, N., and Markgraf, S., *Ferroelectr. Lett.* **Sect. 12**, 63 (1990a)

Shrout, T. R., and Fielding, J., *Proceedings of the 1990 IEEE Ultrasonic Symposium* 711 (1990b)

Singh, R. K., Holland, O.W., and Narayan, J., *Journal of Applied Physics* **68**, 233 (1990).

Smith, H. M., and Turner, A. F., *Appl. Opt.* **4**, 147 (1965)

Smolensky, G. A., *J. Phys. Soc. Jpn. Suppl.* **28**, 26 (1970)

Swartz, S. L., Shrout, T. R., Schulze, W. A., and Cross, L. E., *J. of the American Ceramic Society* **67**, 311 (1984)

Syamaprasad, U., Sheeja Nair, A. R., Sarma, M. S., Guruswamy, P., Mukherjee, P. S., Damodaran, A. D., Krishnamurthy, L., and Achuthan, M., *J. Mater. Sci: Mater. in Elect.* **8**, 199 (1997)

Takeshima, Y., Shiratsuyu, K., Takagi, H., and Tomono, K., *Jpn. J. Appl. Phys., Part 1* **34**, 5083 (1995)

Tantigate, C., Lee, J., and Safari, A., *Appl. Phys. Lett.* **66**, 1611 (1995)

Tantigate, C., and Safari, A., *ISAF 96. Proceeding of th Tenth IEEE International Symposium on Application of Ferroelectric* 479 (1996)

Udayakumar, K. R., Schuele, P. J., Chen, J., Krupanidhi, S. B., and Cross, L. E., *J. Appl. Phys.* **77**, 3981 (1995)

Wakiya, N., Shinozaki, K., and Mizutani, N., *Thin Solid Films* **384**, 189 (2001)

Wang, J., Wong, K. H., Chan, H. L. W., and Choy, C. L., *Ferroelectrics* **252**, 257 (2001)

Wu, W. B., Wong, K. H., and Choy, C. L., *J. Phys. D: Appl. Phys.* **32**, L57 (1999)

Wu, W. B., Wong, K. H., and Choy, C. L., *Thin Solid Films* **360**, 103 (2000)

Zaky, A. A., and Hawley, R., *Dielectric Solids*, Routledge & Kegan Paul Ltd., London, (1970)